

AD-A163 390

HYDRAULIC POWER MODULATION LAMINAR PROPORTIONAL  
AMPLIFIER DEVELOPMENT(U) MASSACHUSETTS INST OF TECH  
CAMBRIDGE DEPT OF MECHANICAL ENGIN. K M LEE ET AL.

1/1

UNCLASSIFIED

NOV 85 HDL-CR-85-122-1 DAK21-81-C-0122

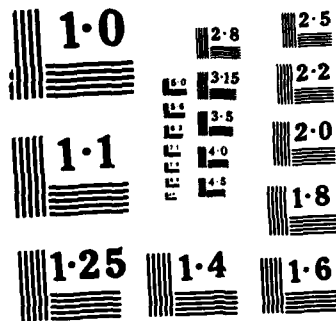
F/G 20/4

NL

END

FILMED

ENC



NATIONAL BUREAU OF STANDARDS  
MICROCOPY RESOLUTION TEST CHART

HDL-CR-85-122-1

November 1985

## AD-A163 390

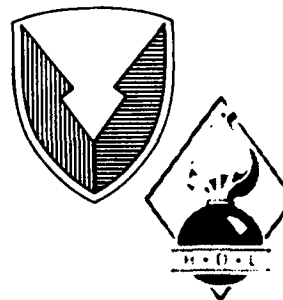
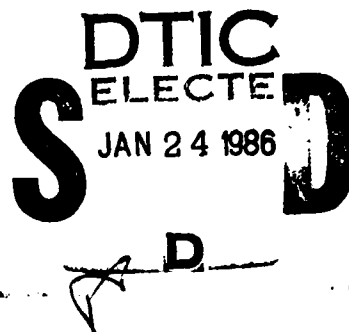
Hydraulic Power Modulation Laminar  
Proportional Amplifier Development

by K.-M. Lee  
D. N. Wormley

Prepared by

Massachusetts Institute of Technology  
Department of Mechanical Engineering  
Cambridge, Massachusetts 02139

Under contract  
DAAK 21-81-C-0122



U.S. Army Laboratory Command  
Harry Diamond Laboratories  
Adelphi, MD 20783-1197

Approved for public release; distribution unlimited.

86 1 24 032

DTIC FILE COPY

The findings in this report are not to be construed as an official Department of the Army position unless so designated by other authorized documents.

Citation of manufacturers' or trade names does not constitute an official indorsement or approval of the use thereof.

Destroy this report when it is no longer needed. Do not return it to the originator.

UNCLASSIFIED

SECURITY CLASSIFICATION OF THIS PAGE (When Data Entered)

REPORT DOCUMENTATION PAGE		READ INSTRUCTIONS BEFORE COMPLETING FORM
1. REPORT NUMBER HDL-CR-85-122-1	2. GOVT ACCESSION NO. <b>AD A163390</b>	3. RECIPIENT'S CATALOG NUMBER
4. TITLE (and Subtitle) Hydraulic Power Modulation Laminar Proportional Amplifier Development	5. TYPE OF REPORT & PERIOD COVERED Contractor Report	6. PERFORMING ORG. REPORT NUMBER
7. AUTHOR(s) K.-M. Lee and D.N. Wormley (HDL contact: James Joyce)	8. CONTRACT OR GRANT NUMBER(s) DAAK 21-81-C-0122 ✓	
9. PERFORMING ORGANIZATION NAME AND ADDRESS Massachusetts Institute of Technology ✓ Department of Mechanical Engineering Cambridge, MA 02139	10. PROGRAM ELEMENT, PROJECT, TASK AREA & WORK UNIT NUMBERS Program Ele: 6.11.02.A	
11. CONTROLLING OFFICE NAME AND ADDRESS Harry Diamond Laboratories Adelphi, MD 20783-1197	12. REPORT DATE November 1985	13. NUMBER OF PAGES 86
14. MONITORING AGENCY NAME & ADDRESS (if different from Controlling Office)	15. SECURITY CLASS. (of this report) UNCLASSIFIED	15a. DECLASSIFICATION/DOWNGRADING SCHEDULE
16. DISTRIBUTION STATEMENT (of this Report) Approved for public release; distribution unlimited.		
17. DISTRIBUTION STATEMENT (of the abstract entered in Block 20, if different from Report)		
18. SUPPLEMENTARY NOTES DA Project: 1L161102AH44 HDL Project: A41134, A4523A, A4533A		
19. KEY WORDS (Continue on reverse side if necessary and identify by block number) Laminar proportional amplifier, Hydraulic systems ✓		
20. ABSTRACT (Continue on reverse side if necessary and identify by block number) A basic analytical and experimental study of the influence of geometry on laminar proportional fluidic amplifier characteristics has been conducted. Performance characteristics for current HDL C-Format amplifier designs as well as new configurations have been determined to identify the design tradeoffs among characteristics including blocked load gain, pressure recovery, flow recovery, efficiency, laminar operating range and dynamic response.		

DD FORM 1 JAN 73 1473

EDITION OF 1 NOV 65 IS OBSOLETE  
S/N 0102-LF-014-6601

UNCLASSIFIED

SECURITY CLASSIFICATION OF THIS PAGE (When Data Entered)

UNCLASSIFIED

SECURITY CLASSIFICATION OF THIS PAGE (When Data Entered)

The results of the study have led to the development and testing of a laminar proportional amplifier (LPA) specifically designed for power modulation applications. The power modulation amplifier has a nozzle to splitter distance which is 37.5 percent of that of the standard LPA design and as a result has a blocked load pressure gain which is approximately 35 percent of that of the standard LPA, but has a pressure recovery, 1.35 times and efficiency double the respective values of the standard LPA. In addition, the power modulation LPA has an increased operating range with respect to temperature variations and increased dynamic response with an increase in the frequency at which 90 degrees phase shift occurs in the frequency response by a factor of 2.6. The increased pressure recovery and efficiency can lead to reductions in fluidic system size and weight for applications in which power modulation is of prime importance.

*page 1 of 1*

UNCLASSIFIED

SECURITY CLASSIFICATION OF THIS PAGE (When Data Entered)

## Contents

	Page
1 INTRODUCTION.....	6
2 NOZZLE/JET/RECEIVER SYSTEM.....	9
2.1 Experimental Apparatus.....	9
2.2 Nozzle.....	14
2.3 Bounded Jet.....	20
2.4 Analytical Model and Receiver Configuration.....	26
3 LAMINAR PROPORTIONAL AMPLIFIER.....	31
3.1 Jet Deflection.....	35
3.2 Input Characteristics.....	37
3.3 Blocked Load Characteristics and Pressure Gain Analysis.....	38
3.4 Output Characteristics.....	39
3.5 Design Considerations.....	40
3.5.1 Effect of $X_{sp}$ and $B_c$ .....	40
3.5.2 Effect of supply duct and receiver geometries.....	41
3.5.3 Effect of control edge spacing and control port geometry.....	44
3.6 Design Summary.....	46
4 LPA CONFIGURATIONS AND PERFORMANCE EVALUATION.....	46
4.1 LPA Configurations and Construction.....	47
4.2 Performance Evaluation.....	47
4.2.1 Influence of modified Reynold's number.....	53
4.2.2 Temperature sensitivity.....	60
4.2.3 Frequency response.....	60
4.2.4 Leakage flow.....	66
4.3 Discussion of Results.....	66
5 SUMMARY AND CONCLUSION.....	67

## Appendices

A.--Bounded Jet Analysis.....	68
B.--Normalized Channel Resistance.....	74

Accession For	
NTIS CRA&I	<input checked="" type="checkbox"/>
DTIC TAB	<input type="checkbox"/>
Unannounced	<input type="checkbox"/>
Justification .....	
By .....	
Distribution /	
Availability Codes	
Dist	Avail and/or Special
A-1	

## Figures

	Page
1 Laminar proportional amplifier (LPA) schematic.....	7
2 LPA output characteristics.....	8
3 LPA power characteristics.....	8
4 LPA blocked-load characteristics.....	8
5 Nozzle/jet/receiver system schematic.....	10
6 LPA characteristic dimensions.....	10
7 Kinematic viscosity of fluid.....	11
8 Experimental apparatus.....	12
9 Test configuration No. 1.....	13
10 Test configuration No. 2.....	13
11 Test configuration No. 3.....	13
12 Discharge coefficient vs. modified Reynold's numbers.....	18
13 Influence of fluid properties on blocked-load pressure recovery.....	19
14 Bounded jet schematic.....	21
15 Influence of aspect ratio on blocked-load pressure recovery.....	23
16 Effect of $X_{sp}$ on blocked load pressure; $\sigma=0.2$ .....	24
17 Effect of aspect ratio on blocked load pressure; $X_{sp}=3$ .....	25
18 Flow regions of nozzle/jet/receiver system.....	27
19 Comparison of output characteristics between analytical and experimental data; $\sigma=0.2$ , $X_{sp}=8$ .....	32
20 Efficiency of nozzle/jet/receiver system; $\sigma=0.2$ , $X_{sp}=8$ .....	32
21 Comparison of output characteristics between analytical and experimental data; $\sigma=0.6$ , $X_{sp}=3$ .....	33
22 Efficiency of nozzle/jet/receiver system; $\sigma=0.6$ , $X_{sp}=3$ .....	33
23 Comparison of output characteristics between analytical and experimental data; gradual expansion receiver.....	34
24 Efficiency of nozzle/jet/receiver system; gradual expansion receiver.....	34
25 Power jet deflection schematic.....	36
26 Flow component representation schematic.....	36
27 The effect of $B_c$ on maximum jet edge pressure differential, $P_{jdm}$ .....	42
28 The effect of constraints on the selection of $B_c$ and $X_{sp}$ .....	42
29 The conventional C-format amplifier design.....	43
30 The offset C-format amplifier design.....	43
31 Effect of supply duct length.....	45
32 C-format power modulation LPA schematic.....	49
33 C-format standard HDL design LPA schematic.....	50
34 Experiment schematic.....	51
35 Amplifier test section schematic.....	52
36 Comparison of output characteristics at $N'_R=100$ .....	54
37 Efficiency of power modulation LPA at $N'_R=100$ .....	54
38 Output characteristics of traditional HDL design LPA.....	55
39 Efficiency of traditional HDL design LPA.....	55
40 Blocked load characteristics of power modulation LPA.....	56
41 Blocked load characteristics of traditional HDL design LPA.....	57
42 Comparison of blocked-load pressure gain.....	58
43 Comparison of blocked-load pressure recovery.....	58
44 Comparison of output characteristics at $N'_R=175$ .....	61
45 Efficiency of power modulation LPA at $N'_R=175$ .....	61

	Page
46 Effect of temperature.....	62
47 Steady state gain of prototype LPA.....	64
48 Comparison of frequency response.....	65
A-1 Flow development of bounded jet.....	69

## Tables

1 Velocity profile of bounded jet.....	29
2 Characteristic dimensions of model LPA.....	48
3 Output rating and efficiency.....	59
A-1 Flow development of bounded jet.....	70

## 1. INTRODUCTION

Hydraulic control systems are widely used in applications where high force levels, fast response, and high-power-to-weight ratio are required. Aerodynamic control surface actuators, machine tool actuators, and mobile equipment control systems frequently employ closed-loop hydraulic control systems. Important performance criteria for these systems include maximum force and velocity capabilities, accuracy, repeatability, maintainability, and cost.

The use of fluidic elements in the sensing, signal processing, and power modulation components of hydraulic control systems offers the potential advantages of high reliability due to the elimination of moving parts, insensitivity to severe vibration and radiation environments, and capability to utilize the hydraulic medium directly for both signal and power level functions. Previous development effort<sup>1</sup> has demonstrated the performance capability of C-Format Harry Diamond Laboratories (HDL) fluidic elements in hydraulic signal processing applications and has demonstrated the viability of developing power level fluid modulation devices, including servovalves using fluidic elements. Effort directed primarily to signal processing and sensing applications has led to development of the laminar proportional amplifier (LPA). This amplifier is shown in figure 1. The C-format has provided a format for minimization of packaging volume and weight and a basis for system design standardization.<sup>2,3</sup> Typical LPA characteristics are illustrated in figures 2 and 3 where output flow-pressure and power-pressure characteristics are plotted and in figure 4 where blocked-load output pressure is plotted versus input pressure.

Fluidic devices are open-center flow devices with continuous flow consumption. In power level applications, devices with high output flow recovery, pressure recovery, and efficiency are required. The standard C-Format HDL LPA which has been developed for signal processing applications has a relatively high pressure gain desirable for signal processing and has lower power gain, pressure recovery, and flow recovery than are optimum in power modulation applications.

In this study effort has been directed to the development of a fluidic amplifier for power modulation

---

<sup>1</sup>D. N. Wormley and K-M Lee, Integrated Component Fluidic Servovalves and Position Control Systems. HDL-CR-82-158-1, Harry Diamond Laboratories (April 1983).

<sup>2</sup>F. M. Manion and T. M. Drzewiecki, Analytical Design of Laminar Proportional Amplifiers, HDL Fluidic State-of-the-Art (October 1974).

<sup>3</sup>T. M. Drzewiecki and F. M. Manion, Flueries 40 : LJARS, The Laminar Jet Angular Rate Sensor, HDL-TM-79-7, Harry Diamond Laboratories (December 1979).

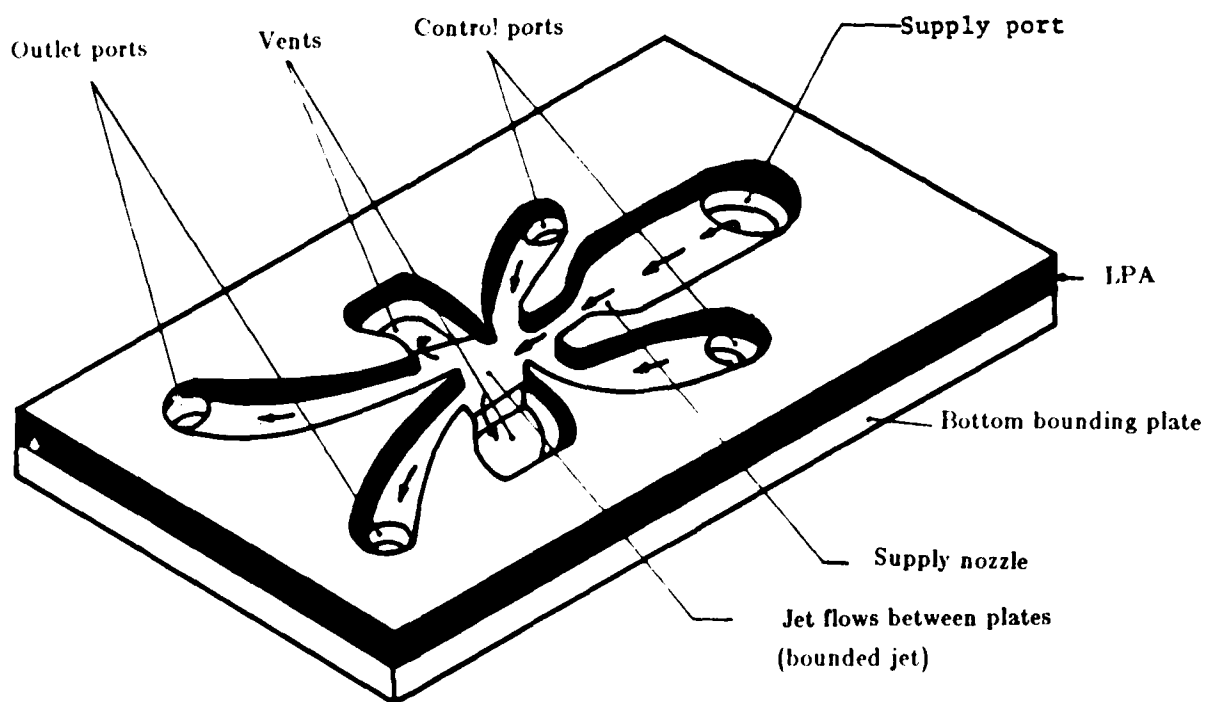


**Figure 1.** Laminar proportional amplifier schematic.

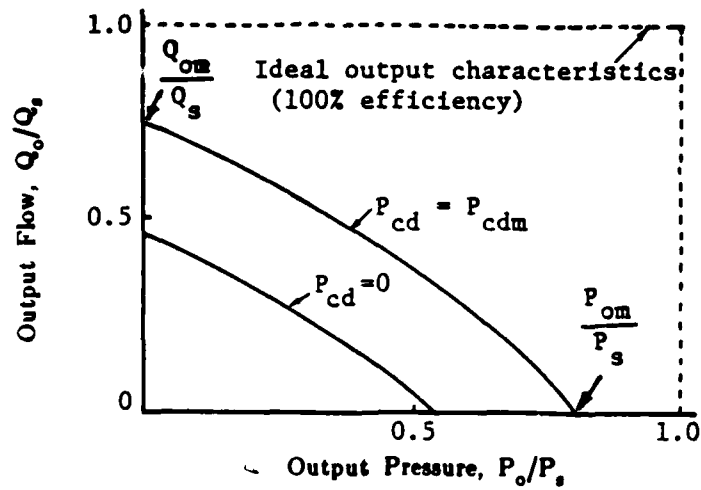


Figure 2. LPA output characteristics.

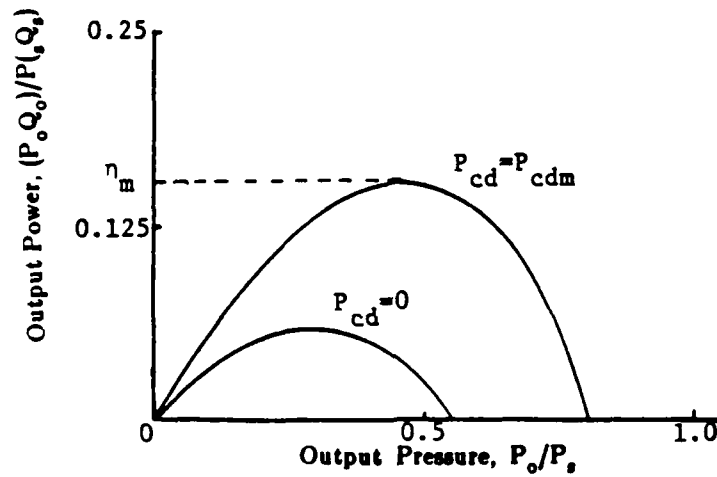


Figure 3. LPA power characteristics.

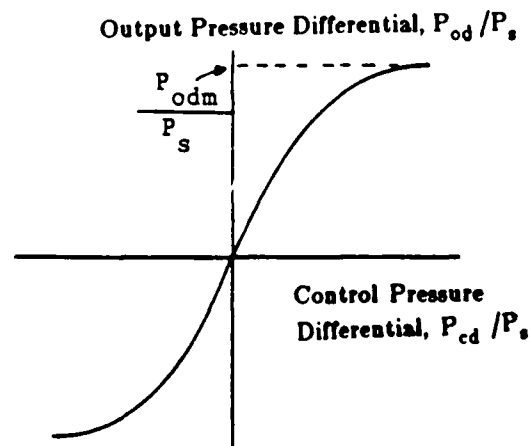


Figure 4. LPA blocked-load characteristics.

applications. The effort has included basic geometric studies to determine the parameters controlling the pressure and flow recovery in an LPA and then effort to develop a new element which can be implemented in the C-Format and provide improved power modulation characteristics. The basic studies are described in section 2 and are based upon the nozzle-jet-receiver geometry shown in figure 5. The amplifier development is based upon the LPA shown in figure 6 where LPA characteristic dimensions are defined.

The experimental data has been obtained for operation on either MIL-H-5606 or DC 200 fluid 20CS which have densities of  $869 \text{ kg/m}^3$  and  $955 \text{ kg/m}^3$  respectively. The kinematic viscosities of DC-200-20CS and MIL-H-5606 are shown in figure 7 as a function of temperature.

## 2. NOZZLE/JET/RECEIVER SYSTEM

In many fluidic devices, the nozzle/jet/receiver system is the primary source of the driving power. The planar nozzle serves to convert the supply pressure into the kinetic energy of a jet and to direct this jet toward the receiver. The function of the receiver is to transform efficiently the kinetic energy of a high-velocity jet into a controllable pressure. The power recovery at the receiver outlet influences the maximum power available for the laminar proportional amplifier when the jet is fully deflected. The design parameters which significantly influence the blocked load pressure recovery are discussed in sections 2.2 and 2.3. An analytical model to predict the output characteristics and the influence of design parameters on the flow and power recovery is described in section 2.4. The parameters considered in the studies are the fluid properties, aspect ratio, nozzle-to-splitter distance, and the receiver geometries.

### 2.1 Experimental Apparatus

An experimental program was conducted to determine the influence of design parameters on power recovery and to obtain sufficiently detailed information so that a rational analytical performance prediction could be developed. The experiments were conducted using a planar nozzle and a channel receiver ten times larger than the prototype standard HDL design LPA, using the experimental apparatus shown in figure 8. The objectives of the experiments were to determine the influence of fluid properties, aspect ratio, and nozzle-to-splitter distance on the blocked-load pressure recovery and the influence of receiver geometries on the output flow-pressure characteristics which influence the power recovery. To aid in developing a rational analytical model, the pressure distribution of the recovered pressure around the receiver inlet was measured.

The typical configuration used to determine the blocked-load pressure recovery is shown in figure 9.

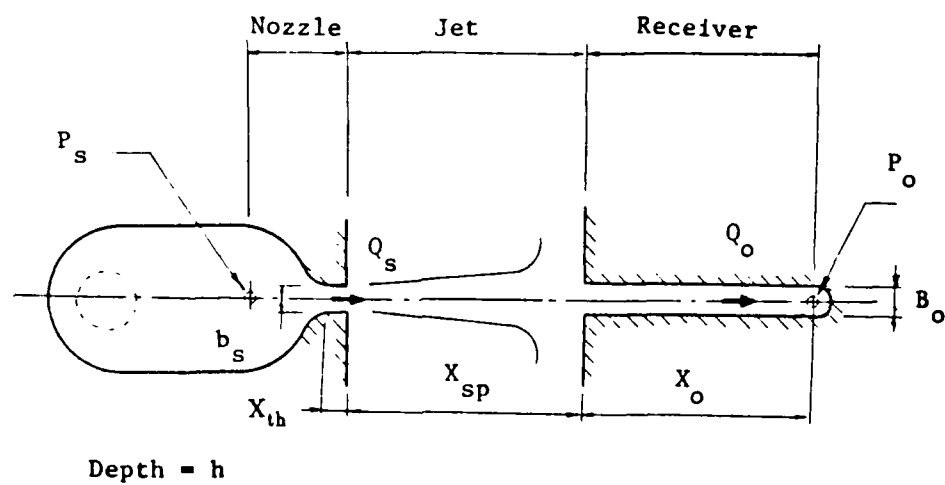


Figure 5. Nozzle/jet/receiver system schematic.

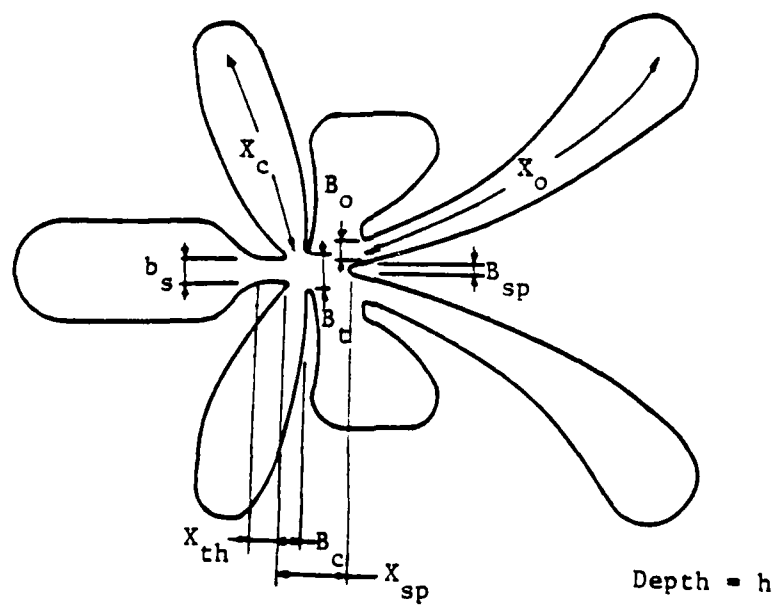
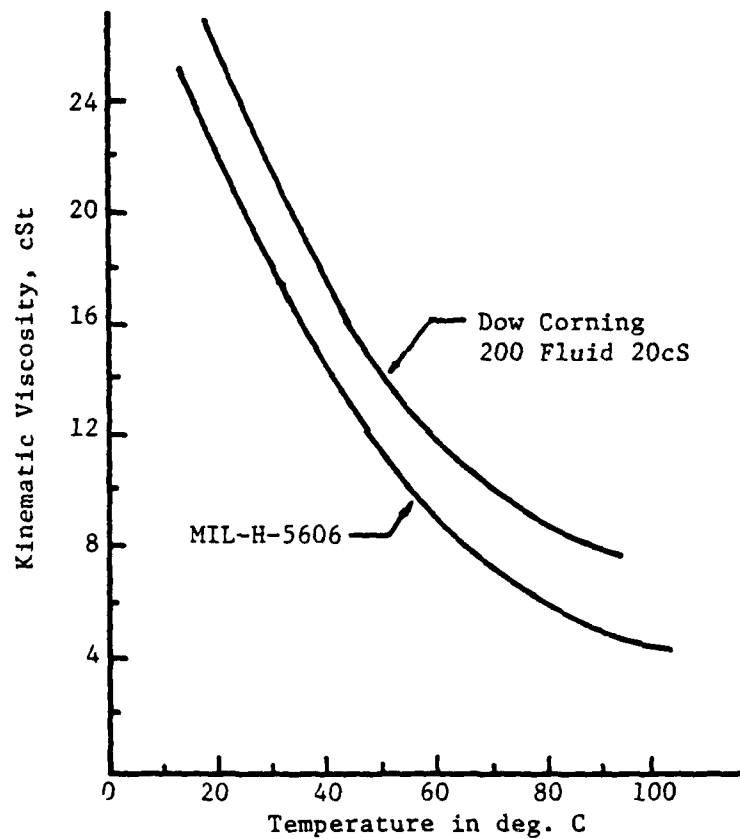


Figure 6. LPA characteristic dimensions.



**Figure 7.** Kinematic viscosity of fluid.

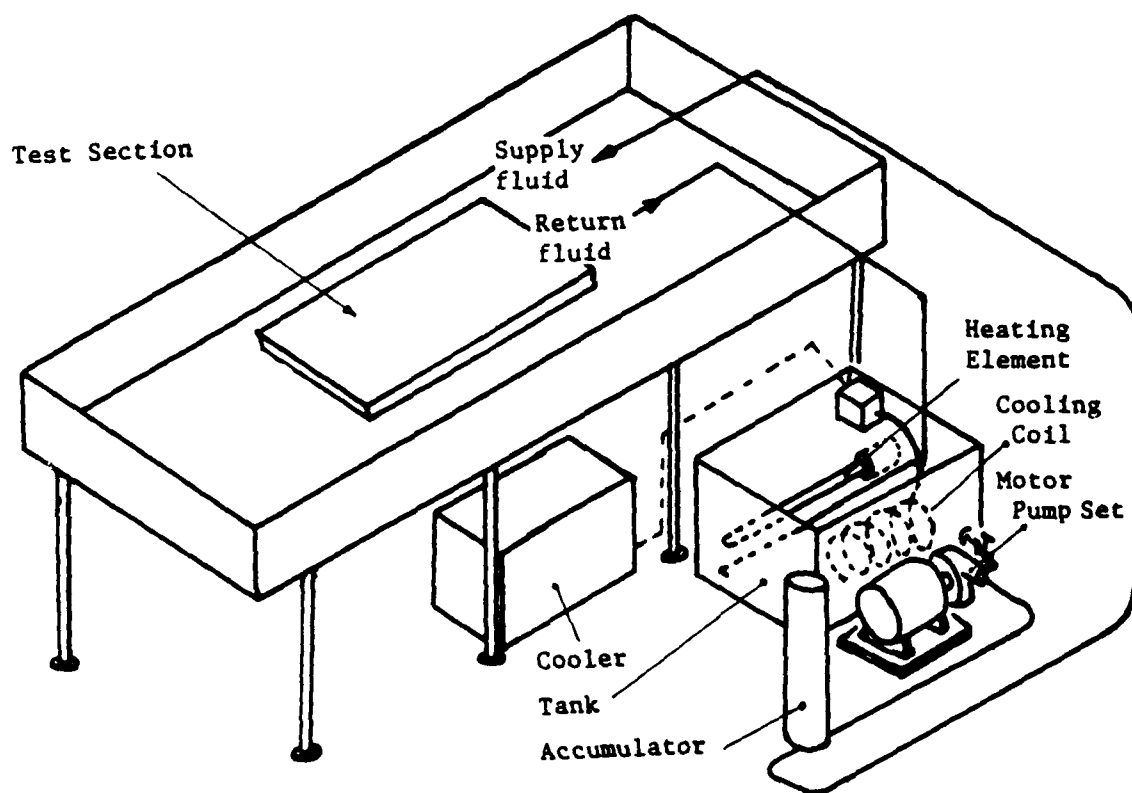
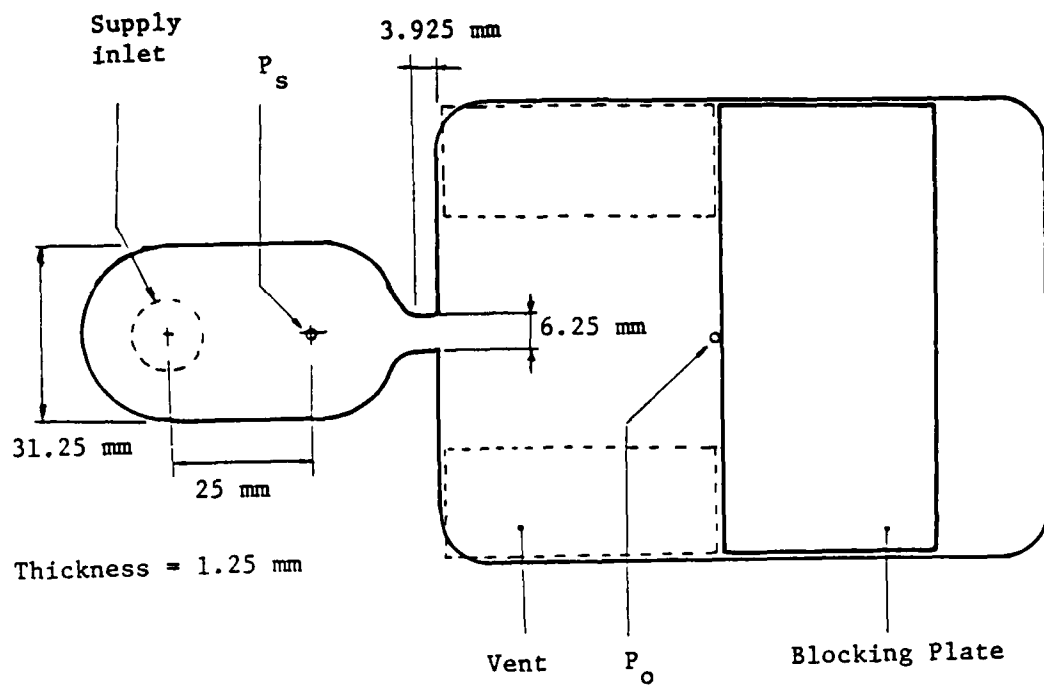
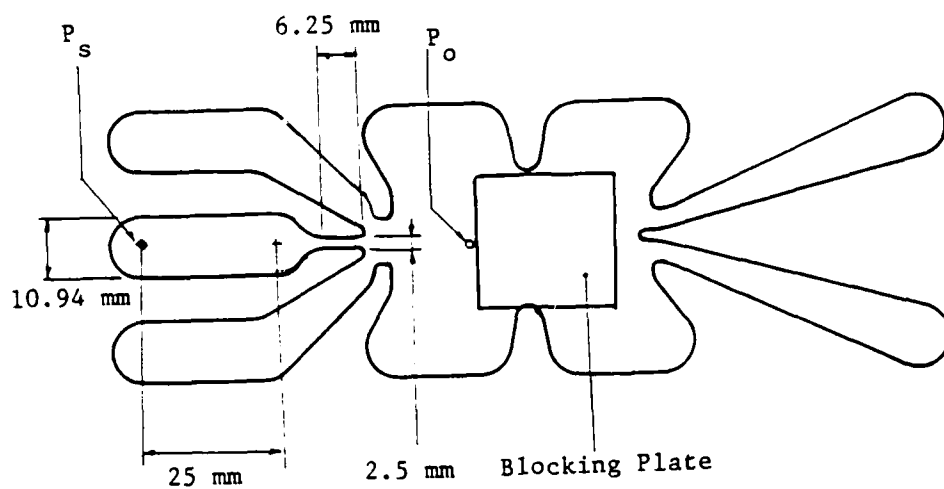


Figure 8. Experimental apparatus.



**Figure 9.** Test configuration no. 1.



**Figure 10.** Test configuration no. 2.

The nozzle throat width is 6.25 mm (0.25 in.) with each model laminate 1.25 mm (0.05 in.) thick, approximately 10 times that of a typical prototype standard HDL design LPA. With four such laminates, experiments with aspect ratios of 0.2, 0.4, 0.6 or 0.8 could be performed. For an aspect ratio greater than unity, the nozzle of the HDL LJARS design with nozzle throat width of 2.5 mm (0.01 in.) and aspect ratio of 1.25 shown in figure 10 was used. The normalized distance between the nozzle exit and the receiver inlet,  $X_{sp}$ , can be varied between 0 and 10 so that the influence of  $X_{sp}$  on the maximum pressure recovery can be observed. Of particular interest is the comparison of the maximum pressure recovery of small  $X_{sp}$  with the conventional design for  $X_{sp} = 8$ . Test configurations no. 1 and no. 2 were designed for blocked load experiments. To obtain the output characteristics, the test configuration no. 3 shown in figure 11 was used. Two particular shapes were chosen for the receiver, a constant width channel and a gradual diverging channel with included angle of 4.5 degrees. The objective was to investigate the increase in flow recovery contributed by the diffuser-like receiver which converts kinetic energy to a controllable pressure.

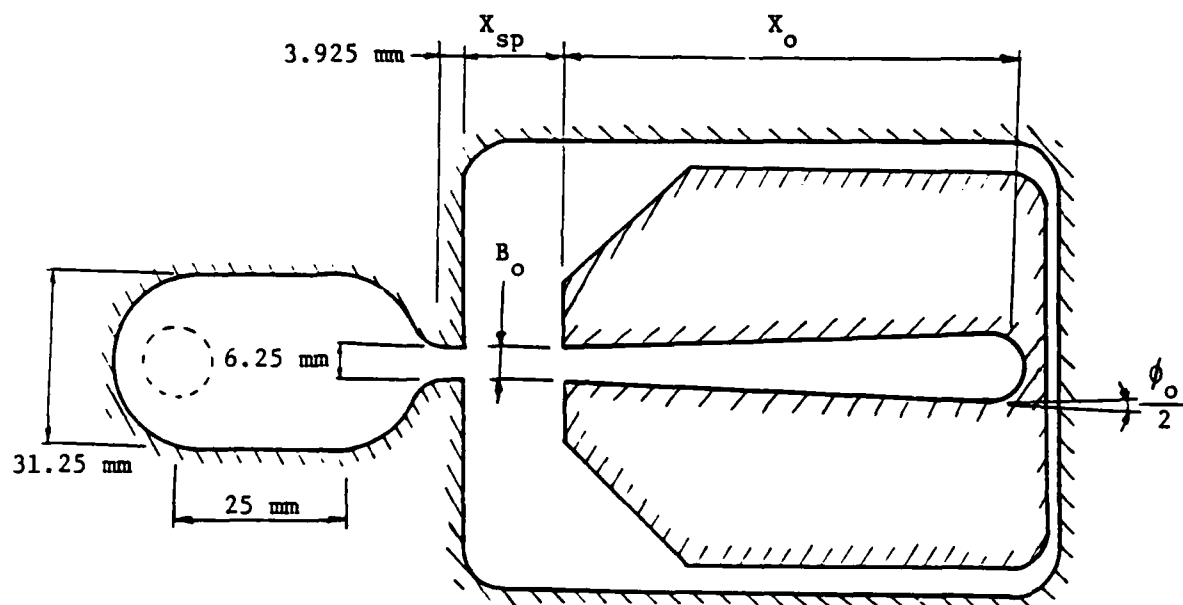
The general experimental apparatus is shown in figure 8. The oil is supplied from a tank with dimensions of 45 cm x 60 cm x 30 cm (height) and pumped through a 1/2 hp motor-pump set, an accumulator, and a pressure regulator. The system is equipped with a 1250 watt portable cooling unit and a 2000 watt heater capable of varying the oil temperature from 4 C (40 F) to 60 C (140 F), designed to cover an entire laminar operating range by regulating the fluid viscosity which is a function of temperature. In each test, the fluid temperature, supply pressure, and recovered pressure were measured. The volumetric flow rate was determined from the pressure drop measured by a calibrated laminar flow restriction.

To obtain the distribution of the recovered pressure, a row of static pressure taps were drilled through the cover plate, perpendicular to the direction of flow and along the edge which includes the receiver inlet. Fourteen holes, seven on each side of the receiver centerline and spaced 1.875 mm (0.075 in.) apart and each inserted with a short steel tube with internal diameter of 0.825 mm (0.033 in.), were drilled. A pair of datametric electronic monometers were used to measure the static pressure. Each pressure reading was plotted against the supply pressure by an electronic X-Y plotter at a pre-determined fluid temperature.

## 2.2 Nozzle

The flow condition at the nozzle exit is characterized by the volumetric discharge coefficient defined as

$$C_d = \frac{\text{actual flow}}{\text{ideal flow}} = \frac{Q_s}{\sigma b_s^2 u_s} \quad (1)$$



TEST DEVICE NO.	$X_{sp}$	$X_o$	$B_o$	$\phi_o$ (deg.)
3a	8	7	1	0
3b	3	12	1	0
3c	3	12	1.1	4.5

Figure 11. Test configuration no. 3.

where

$b_s$  = nozzle throat width,

$\sigma$  = aspect ratio,  $h/b_s$ ,

$P_s$  = supply pressure,

$P_v$  = vent pressure, and

$\rho$  = density of fluid.

and  $u_s$  is the Bernoulli's velocity defined as

$$u_s = \sqrt{\frac{2(P_s - P_v)}{\rho}} \quad (2)$$

It is of interest to compare the analytical and experimental discharge coefficient.

Drzewiecki<sup>4</sup> showed that the discharge coefficient of the planar nozzle is primarily a function of modified Reynold's number for various nozzle configurations and for a wide range of modified Reynold's number, where the modified Reynold's number is

$$N_R' = \frac{N_R}{(1 + X_{th})(1 + 1/\sigma)^2} \quad (3)$$

$$N_R = \frac{b_s u_s}{\nu} \quad (4)$$

where

$X_{th}$  = nozzle throat length-to-width ratio, and

$\nu$  = kinematic viscosity.

The modified Reynold's number may be shown analytically to be equivalent to the normalized entrance length of a constant width rectangular channel with an effective length,  $1 + X_{th}$ , and uniform inlet velocity profile as

$$\phi \equiv \frac{X_{eq}}{D_e Re} = \frac{0.25}{C_d N_R'} \quad (5)$$

where

---

<sup>4</sup>T. M. Drzewiecki, *Flueries* 37 : A General Planar Nozzle Discharge Coefficient Representation, HDL-TM-74-5, Harry Diamond Laboratories (August 1974).

$$D_e = \frac{2}{1+1/\sigma}, \quad (6)$$

$$Re = D_e \frac{b_s \bar{u}}{\nu}, \quad (7)$$

$$X_{eq} = 1 + X_{th}, \quad (8)$$

$\bar{u}$  = average velocity.

The pressure drop in the neighborhood of the duct entrance for the above defined entrance length can be derived as

$$\frac{P_s - P_v}{0.5 \rho \bar{u}^2} = 1 + 15.2 \phi^{1/2}, \quad 10 \leq C_d N_R' \leq 200. \quad (9)$$

From the definition of discharge coefficient and equation (9),  $C_d$  can be related to the modified Reynold's number as

$$C_d^2 + 7.6(N_R')^{1/2} C_d^{1.5} - 1 = 0. \quad (10)$$

The analytical discharge coefficients based on the rectangular channel model are compared with the experimental curve-fit solutions which were suggested by Drzewiecki, et al<sup>3,5</sup> to reduce the numerical solution to a more tractable closed form in figure 12. The comparison shows excellent agreement for modified Reynold's numbers between 20 and 240. Below the modified Reynold's number of 20, the influence of aspect ratio on  $C_d$  may not be neglected.

To determine the effect of the fluid properties, the test configuration no. 1 with an aspect ratio of 0.2 and  $X_{sp}$  equal to 8, was tested with MIL-II-5606 at a temperature of 26.7 C and with DC-200-20CS in a temperature range from 15 to 60 C. The use of two different fluids at various temperatures serves as a means to vary the fluid density and viscosity. The characteristic velocity was varied by regulating the supply pressure. The experimental data plotted in figure 13 result in a single curve which indicates that the fluid properties can be expressed in terms of  $N_R'$ .

The data in figures 12 and 13 lend confidence in the definition of the flow condition at the nozzle exit by the modified Reynold's number and in the approximation of the nozzle exit velocity profile by the velocity profile corresponding to an inlet flow to the rectangular channel of equivalent length  $1 + X_{th}$ .

<sup>3</sup>T. M. Drzewiecki and F. M. Manion, *Flueries 40* : LJARS, The Laminar Jet Angular Rate Sensor, HDL-TM-70-7, Harry Diamond Laboratories (December 1970).

<sup>5</sup>T. M. Drzewiecki, *Flueries 38* : A Computer-Aided Design Analysis for the Static and Dynamics Port Characteristics of Laminar Proportional Amplifiers, HDL-TR-1758, Harry Diamond Laboratories (June 1970).

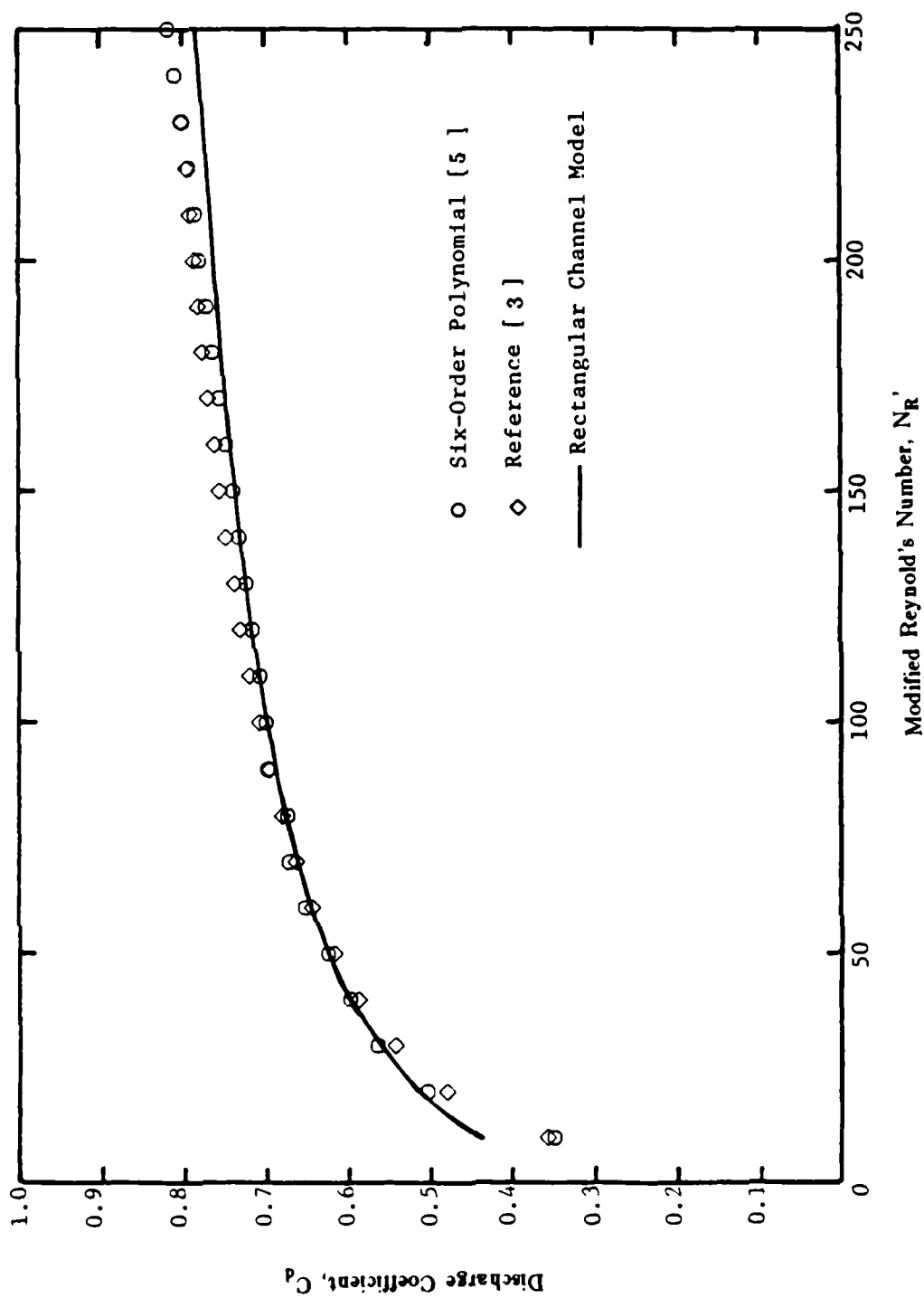


Figure 12. Discharge coefficient vs. modified Reynold's numbers.

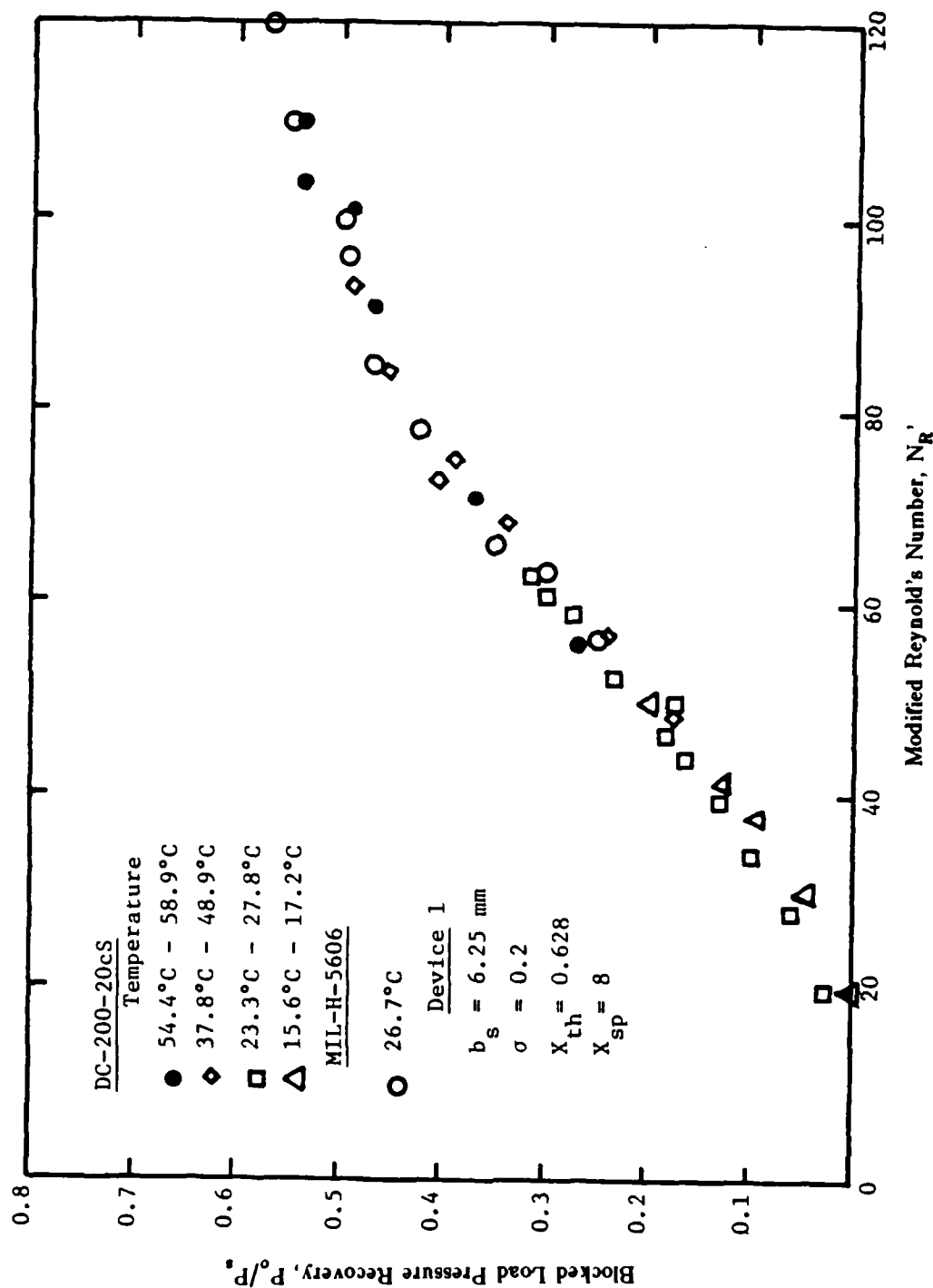


Figure 13. Influence of fluid properties on blocked-load pressure recovery.

### 2.3 Bounded Jet

Two regions of the jet flow between the nozzle exit and the receiver inlet may be considered; namely, a region with negligible pressure gradient and a region where the adverse axial pressure gradient due to the presence of the receiver may not be neglected. The bounded jet in the absence of the receiver is shown in figure 14 and is discussed in this section. It is assumed that the jet issues into a region of essentially stagnant fluid having a low velocity compared to the jet. It has been determined<sup>1</sup> that the standard HDL design LPA must be operated with  $N_R' < 120$  to avoid transition to turbulence. In many power modulation applications where a high supply pressure is used, a low aspect ratio (less than unity) is normally required for the standard HDL design LPA to limit the operation to the laminar regime. The study of the laminar bounded jet with an aspect ratio less than unity is required to develop design information for power modulation configurations.

From the order-of-magnitude study, the momentum equation can be written as

$$\frac{\sigma}{2} U \frac{\partial U}{\partial X} + \sigma V \frac{\partial U}{\partial Y} + W \frac{\partial U}{\partial Z} = \frac{2}{\sigma C_d N_R} \left( \sigma^2 \frac{\partial^2 U}{\partial Y^2} + \frac{\partial^2 U}{\partial Z^2} \right), \quad (11)$$

where

$$\begin{aligned} X &= \frac{x}{b_s} & Y &= \frac{y}{b_s/2} & Z &= \frac{z}{h/2} \\ U &= \frac{u}{\bar{u}} & V &= \frac{v}{\bar{u}} & W &= \frac{w}{\bar{u}} \end{aligned}$$

$\bar{u}$  = average velocity defined at the nozzle exit.

Depending on the order of magnitude comparison between the effect of the shear stresses acting on the top and bottom plates and that on the surrounding fluid, the jet flow can be boardly divided into the following cases in terms of the aspect ratio

1.  $\sigma^2 \gg 1$ , the effect of the shear stresses on the bounding plates is insignificant in comparison to that on the surrounding fluid, and the jet flow can be considered as two dimensional.
2.  $\sigma^2 \sim 1$ , the effect of the shear stresses on the bounding plates and that on the surrounding fluid are of equal order-of-magnitude.
3.  $\sigma^2 \ll 1$ , the effect of the shear stresses on the bounding plates dominates.

To determine the influence of aspect ratio on blocked load pressure recovery, configuration no. 2 with aspect ratios of 1.25 and 2.5 was tested with DC-200-20CS at 25.6 and 16.1 C. The experimental data are

---

<sup>1</sup>D. N. Wormley and K-M Lee, Integrated Component Fluidic Servovalves and Position Control Systems, HDL-CR 82-158-1, Harry Diamond Laboratories (April 1983).

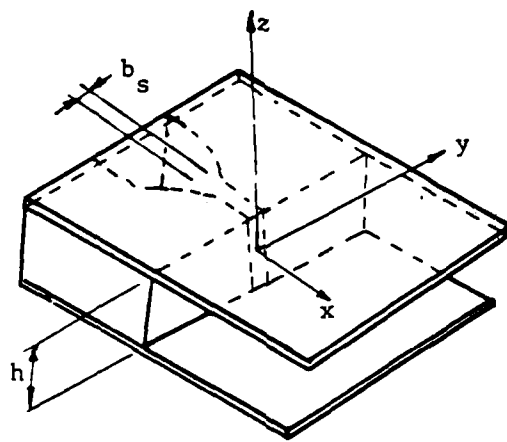


**Figure 14.** Bounded jet schematic.

compared with data from configuration no. 1 with an aspect ratio equal to 0.2 in figure 15. The data show that the blocked-load pressure recovery increases as the aspect ratio increases within the laminar operating range of  $40 \leq N_R' \leq 120$ . The pressure recovery is more sensitive to the change in modified Reynold's number for the aspect ratio of 0.2 than for the aspect ratio of unity or greater if  $N_R'$  is greater than 40. As aspect ratios of unity or less are commonly encountered, an alternate means to increase the pressure recovery is desirable.

Integrating equation (11),

$$\frac{d}{dX} \int_{Z=0}^1 \int_{Y=0}^{\infty} U^2 dYdZ = - \frac{4}{\sigma^2 C_d N_R'} \int_{Y=0}^{\infty} \text{Abs} \left[ \frac{\partial U}{\partial Z} \right]_{Z=1} dY. \quad (12)$$

Equation (12) shows that the decay of the jet momentum is due to the bounding plate frictional losses which increase with the increase of  $X_{sp}$ . The rate of decay can be reduced by operating at a high laminar Reynold's number and/or with a larger aspect ratio.

It is of interest to determine the influence of  $X_{sp}$  on the blocked load pressure recovery. Figure 16 shows the experimental data using configuration no. 1 with an aspect ratio equal to 0.2 and four different  $X_{sp}$  of 4, 6, 8, and 10. For  $\sigma=0.2$ , the blocked-load pressure recovery increases from 0 to 0.4 for  $X_{sp}=10$  and from 0.6 to 0.8 for  $X_{sp}=4$  corresponding to the modified Reynold's number from 40 to 100. As the nozzle discharge coefficient changes by a factor of 1.167 in the same range of modified Reynold's numbers, the influence of Reynold's number on the blocked-load pressure recovery is primarily due to the top and bottom bounding plates which increase the jet spread and reduce the jet momentum through the frictional effects. The data indicate that the blocked-load pressure recovery increases proportionally as  $X_{sp}$  decreases for an aspect ratio much lower than unity. Another attractive feature for using a smaller  $X_{sp}$  than 8 stands on the evidence,<sup>3</sup> that a larger laminar operating range can be obtained with smaller  $X_{sp}$ .

Configuration no. 3b with  $X_{sp}$  equal to 3 and with four different aspect ratios of 0.2, 0.4, 0.6 and 0.8 was tested to determine the influence of aspect ratio and modified Reynold's number on the system with small  $X_{sp}$ . The data plotted in figure 17 show that a maximum pressure recovery as high as 90 percent is obtainable and that the blocked-load pressure recovery is less sensitive to modified Reynold's number if the modified Reynold's number is greater than 100. The high pressure recovery obtainable is contributed by small  $X_{sp}$  and high laminar operating Reynold's number.

<sup>3</sup>T. M. Drzewiecki and E. M. Manion, *Flueries* 40 : LJARS, The Laminar Jet Angular Rate Sensor, HDL-TM-70-7, Harry Diamond Laboratories (December 1970).

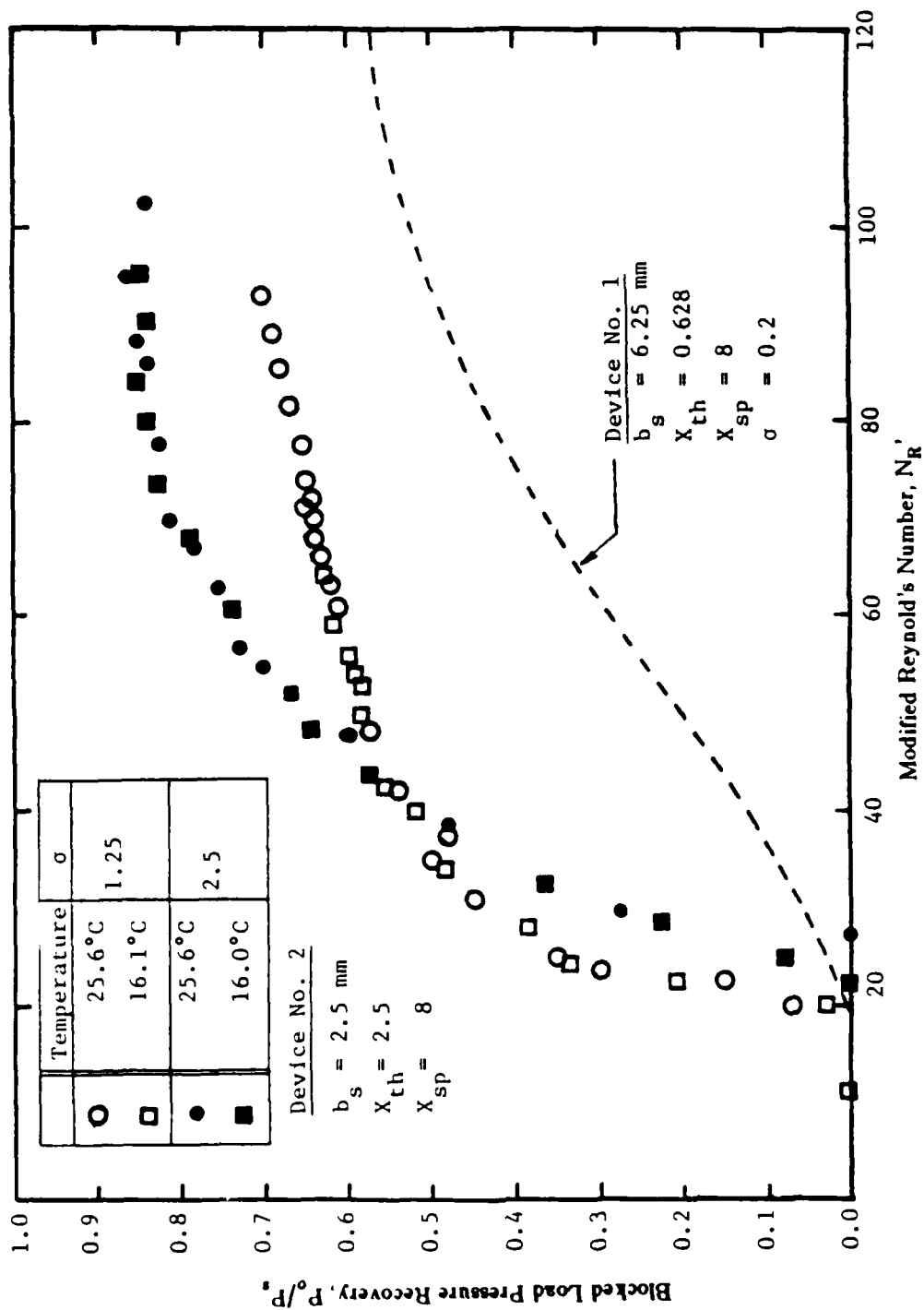


Figure 15. Influence of aspect ratio on blocked-load pressure recovery.

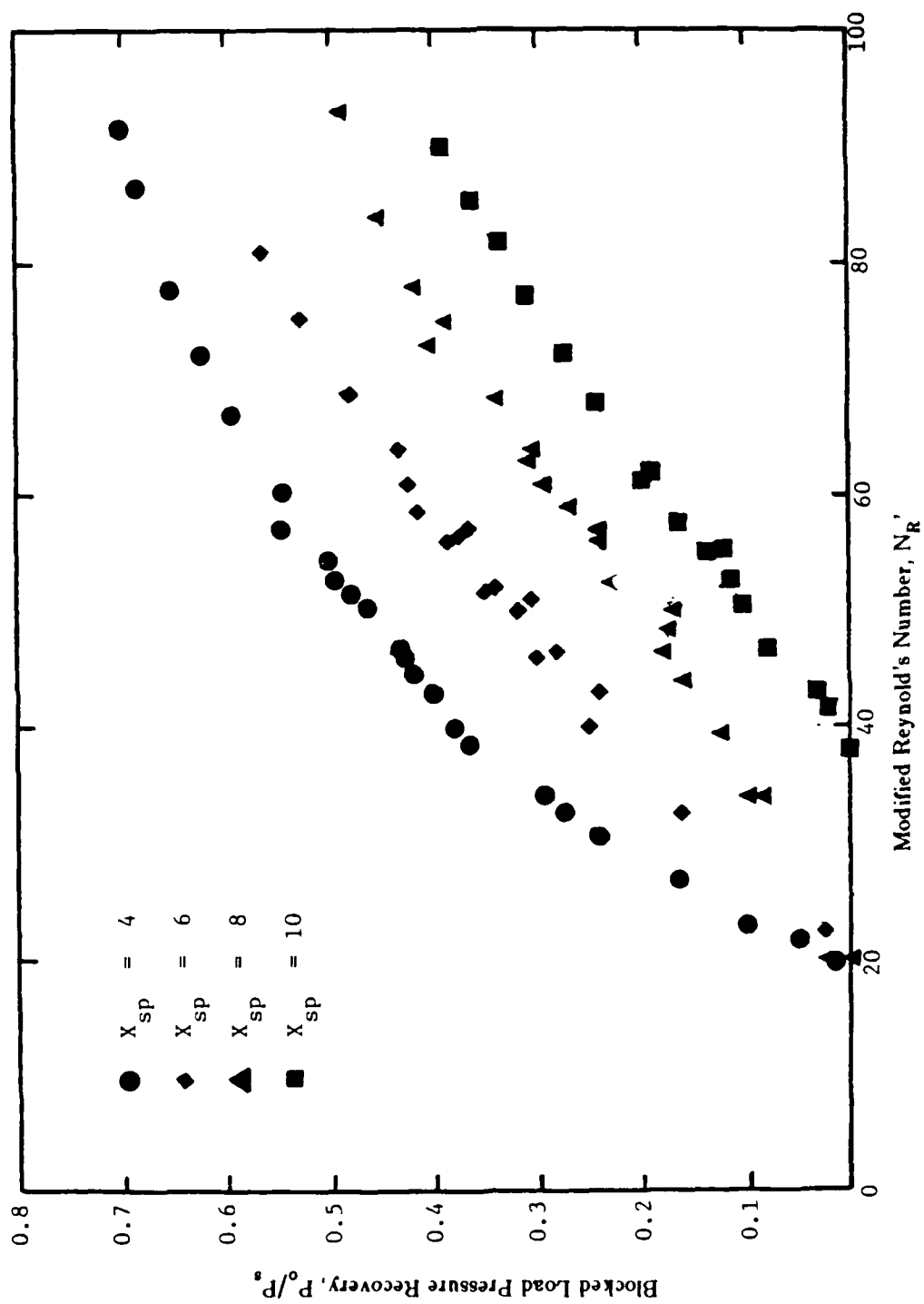


Figure 16. Effect of  $X_{sp}$  on blocked load pressure;  $\sigma=0.2$ .

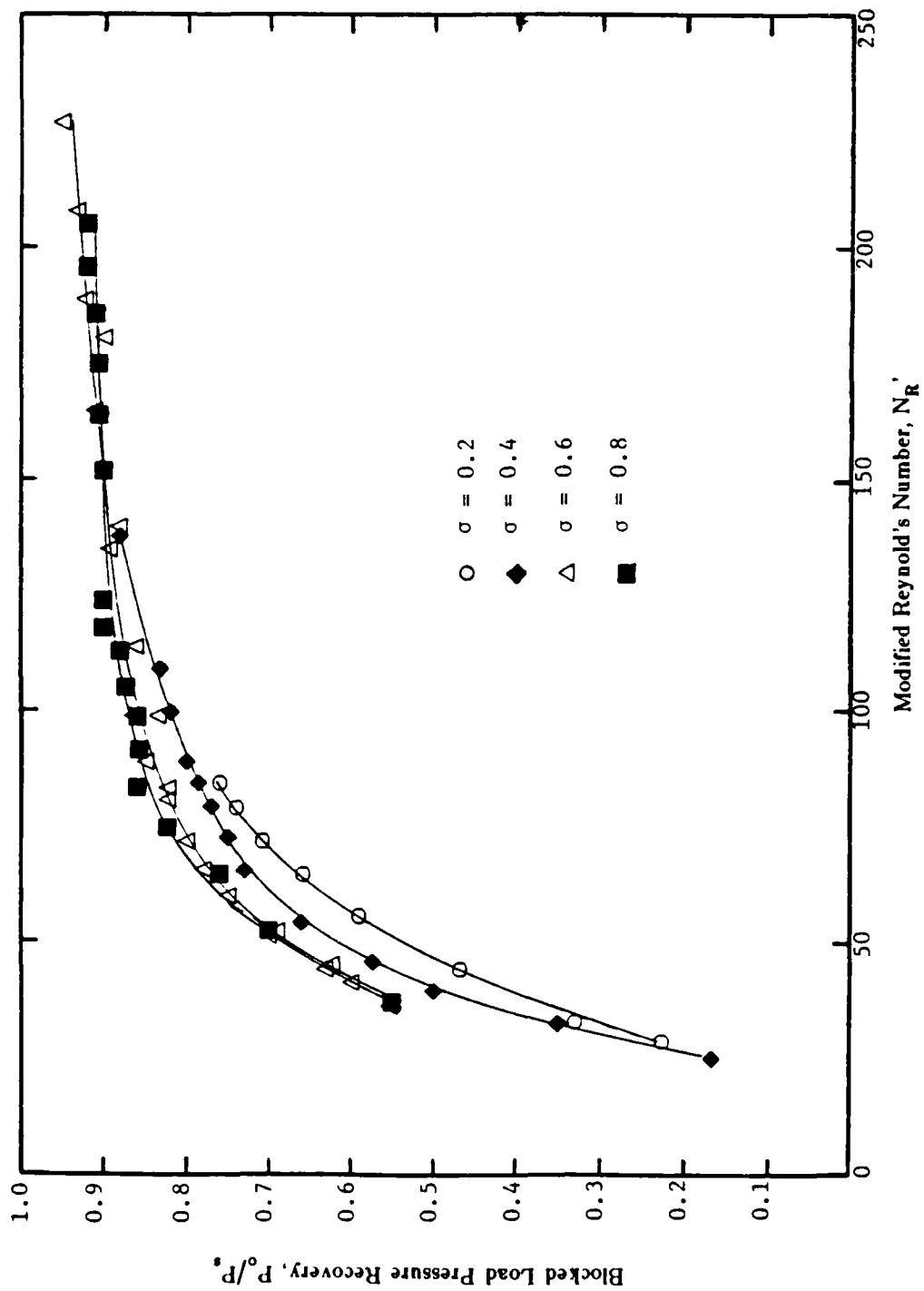


Figure 17. Effect of aspect ratio on blocked load pressure;  $X_{sp} = 3$ .

## 2.4 Analytical Model and Receiver Configuration

In the following discussions, an analytical model to predict the output pressure-flow characteristics is developed. The entire flow field is sub-divided into the regions shown in figure 18 :

- Planar nozzle flow.
- Bounded jet flow with negligible pressure gradient, indicated by CV1.
- Jet/receiver interaction where the adverse axial pressure gradient due to the load may not be neglected, indicated by CV2 and CV3.

The nozzle/jet/receiver system model is based on the following operating conditions and design requirements for power modulation :

1. The flow is incompressible, laminar, and steady.
2. The aspect ratio,  $\sigma$ , is less than 0.8 as it is generally encountered for power modulation.
3. The modified Reynold's number is greater than 20 below which the pressure recovery is too low for practical use.
4. The nozzle-to-receiver distance,  $X_{sp}$ , is limited to 10 or less as a high pressure recovery is generally desirable in power modulation.
5. The included expansion angle of the receiver is small, 6 degrees or less, which is generally encountered in C-Format LPA design and to avoid flow separation.

The bounded jet problem is analysed by the integral method. The basic equations are the continuity equation, the momentum equation, and the mechanical energy equation with the following boundary conditions :

- the symmetries about the X-Y and the X-Z planes,
- the non-slip conditions at the top and bottom bounding plates,
- the axial velocity tends to zero as Y tends to infinity,

and the initial condition,  $X = 0$ , is defined by the flow condition at the nozzle exit. The flow in the quarter region of the jet cross-section is considered because the flow is symmetric with respect to the Y axis and Z axis. A general form of the velocity profile at any particular distance, X, measured from the nozzle exit, consists of a main flow region, a mixing region, the wall boundary layer and the interferential region. The boundary conditions and the velocity profile assumptions are tabulated in table 1 in terms of the following jet parameters :

$$m_z = \frac{\delta_z}{h/2}, \quad (13)$$

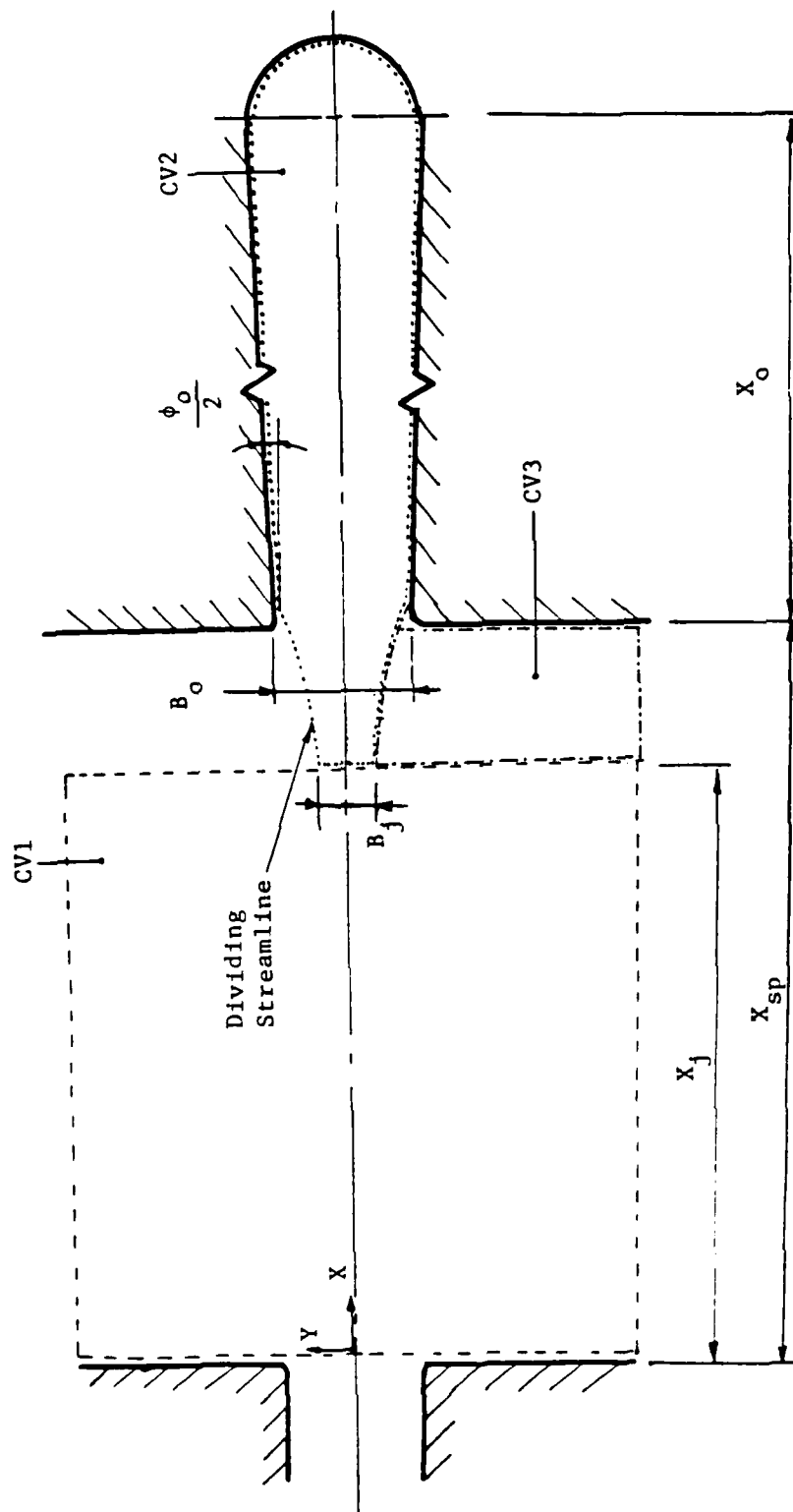


Figure 18. Flow regions of nozzle/jet/receiver system.

$$\beta_1 = \frac{\delta_1}{b_s/2}, \quad (14)$$

$$m_y = \frac{\delta_y}{b_s/2}, \quad (15)$$

$$\beta_2 = \beta_1 + m_y. \quad (16)$$

where  $\delta_z$ ,  $\delta_1$  and  $\delta_y$  are the wall boundary layer thickness, main flow core width and width of mixing region respectively. The procedures for computing the jet parameters as a function of axial distance are summarized in appendix A.

At the jet/receiver interaction region, it is assumed that a dividing streamline exists at the receiver inlet and separates the flow passing through the receiver and all remaining jet flow which misses the receiver as shown in figure 18. The dividing streamline is defined by the continuity equation as

$$\int_{Z=0}^1 \int_{Y=0}^{B_j} U|_{X_j} dY dZ = \frac{Q_o}{Q_s} \quad (17)$$

where  $U|_{X_j}$  is the velocity profile of the bounded jet computed at  $X=X_j$ . Reid's analysis<sup>6</sup> on the axial symmetrical turbulent jet/receiver interaction has suggested the initial trial for the spacing,  $X_{sp}-X_j$ , to be one. It is expected that a larger entrained flow and a jet spread are encountered for the large  $X_{sp}$  than for the small  $X_{sp}$ . As the depth of jet penetration into the receiver depends on the operating Reynold's number, a smaller spacing,  $X_{sp}-X_j$ , is required for the high Reynold's number flow than for the low Reynold's number flow.

As  $X_o \gg X_{sp}-X_j$ , the frictional losses due to the top and bottom plates in the jet/receiver interaction are negligible compared to that in the receiver. The momentum equation is written for CV2 in normalized form for the pressure drop as

$$\frac{P_r - P_o}{0.5\rho\bar{u}_o^2} = (f.Re_o)\phi_o + K_{fd} + K_j, \quad (18)$$

where

---

<sup>6</sup>E. G. Reid, Static and Dynamic Interaction of Fluid Jet and a Receiver-Diffuser, Department of Mechanical Engineering, Ph.D Thesis, MIT (September 1964).

TABLE 1. VELOCITY PROFILE OF BOUNDED JET

	Region	Boundary Conditions	Velocity Profile
Main Flow	$0 \leq Y \leq \beta_1$ $0 \leq Z \leq 1-m_z$	Uniform	$U = U_c$
Mixing	$\beta_1 \leq Y \leq \beta_2$ $0 \leq Z \leq 1-m_z$	$U, \frac{\partial U}{\partial Y}(X, \beta_2, Z) = 0$ $U, \frac{\partial U}{\partial Y}(X, \beta_1, Z) \text{ cont.}$ $U, \frac{\partial U}{\partial Z}(X, Y, 1-m_z) \text{ cont.}$	$U = \frac{U_c}{2}(1 + \cos \pi \eta)$ $\eta = \frac{Y - \beta_1}{\beta_2 - \beta_1}$
Boundary Layer	$0 \leq Y \leq \beta_1$ $1-m_z \leq Z \leq 1$	$\frac{\partial U}{\partial Y}(X, 0, Z) = 0$ $U(X, Y, 1) = 0$ $U, \frac{\partial U}{\partial Z}(X, Y, 1-m_z) \text{ cont.}$ $U, \frac{\partial U}{\partial Y}(X, \beta_1, Z) \text{ cont.}$	$U = U_c \cos \frac{\pi}{2} \xi$ $\xi = \frac{Z - (1 - m_z)}{m_z}$
Interference	$\beta_1 \leq Y \leq \beta_2$ $1 - m_z \leq Z \leq 1$	$U(X, Y, 1) = 0$ $U(X, \beta_2, Z) = 0$ $U, \frac{\partial U}{\partial Z}(X, Y, 1-m_z) \text{ cont.}$ $U, \frac{\partial U}{\partial Y}(X, \beta_1, Z) \text{ cont.}$	$U = \frac{U_c}{2}(1 + \cos \pi \eta) \cos \frac{\pi}{2} \xi$ $\eta = \frac{Y - \beta_1}{\beta_2 - \beta_1}$ $\xi = \frac{Z - (1 - m_z)}{m_z}$

$$fRe_o \phi_o = - \left( \frac{2\nu}{u_o A_o} \right) \int_0^{x_o} \oint \frac{\partial}{\partial n} \left( \frac{u_\infty}{u_o} \right) ds dx', \quad (19)$$

$$\phi_o = \frac{X_o}{4(1+B_o/\sigma)^2 C_d N_R (Q_o/Q_s)}, \quad (20)$$

$$x' = x - x_{sp}$$

$$K_{fd} = 2 \left[ \frac{1}{A_o} \int_{out} \left( \frac{u}{u_o} \right)^2 dA - 1 \right] - \left( \frac{2\nu}{u_o A_o} \right) \int_0^{x_o} \oint \frac{\partial}{\partial n} \frac{u - u_\infty}{u_o} ds dx', \quad (21)$$

$$K_j = 2 \left[ 1 - \frac{1}{A_o} \int_{in} \left( \frac{u}{u_o} \right)^2 dA \right], \quad (22)$$

and  $u_\infty$  is the fully developed velocity of the rectangular channel. The sum of the first and second terms are the pressure drop corresponding to the flow through rectangular channel with uniform inlet velocity profile. The parameters,  $(fRe_o)$  and  $K_{fd}$ , have been obtained by Lee<sup>7</sup> as a function of aspect ratio and included angle of divergence. It follows that the third term,  $K_j$ , is an additional correction factor due to the jet flow at the receiver inlet.

The average pressure acting on the receiver inlet of CV2 is

$$\frac{P_r}{P_s} = \frac{1}{2} \frac{P_m}{P_s} \left[ 1 + \cos \pi \frac{B_j}{\beta_1 + m_y} \right], \quad (23)$$

where the peak pressure  $P_m$  can be written from the momentum equation for CV3 as

$$\frac{P_m}{P_s} = \frac{4C_d^2}{\beta} \int_{Z=0}^1 \int_{Y=B_j}^\infty U^2|_{X=X_j} dY dZ, \quad (24)$$

and where the width of the recovered pressure distribution,  $\beta$ , was determined as a function of jet width,  $\beta_2(X=X_j)$ , by Lee<sup>7</sup>.

With the jet velocity profile computed at  $X=X_j$ , the blocked-load pressure recovery can be predicted from equation (24) with  $B_j = 0$  and the output pressure,  $P_o$ , can be predicted as a function of output flow,  $Q_o$ , using equations (17), (18), (23), and (24).

---

<sup>7</sup>K-M Lee, Analytical and Experimental Development of a Laminar Proportional Amplifier for Power Modulation, Ph.D Thesis, Department of Mechanical Engineering, MIT (January 1985).

The analytical predictions of the output characteristics and the efficiency which is a ratio of the output power to supply power for the system have been obtained for various configurations. Figures 19 and 20 are plotted for  $\sigma=0.2$  and  $X_{sp}=8$  at  $N_R' = 55, 75$  and  $100$ . The comparisons between analytical and experimental output flow-pressure characteristics show that the data computed at  $X_j=6.5$  provides a better estimation than at  $X_j=7$ . The efficiency as well as the pressure and flow recovery are very low for long  $X_{sp}$  in the case of low aspect ratios, particularly for  $N_R'$  equal to 55 or less.

Figures 21 and 22 show the output characteristics and the efficiency for  $\sigma=0.6$  and  $X_{sp}=3$  at  $N_R'$  of 51, 72, 140 and 200. The data for  $N_R'=51$  are computed at  $X_j=2$  and that for  $N_R'=72, 140$  and  $200$  are computed at  $X_j=2.5$ . Comparison of figure 19 with figure 21 shows that the blocked-load pressure recovery at  $N_R'=100$  has been significantly increased from 0.5 to 0.8 by reducing  $X_{sp}$  from 8 to 3. As the distance between the nozzle exit and receiver outlet remains unchanged, the reduction in  $X_{sp}$  is accompanied by an increase in  $X_o$ . As a result, the flow recovery has been increased only from 0.42 to 0.5 (a factor of 1.2) and is due primarily to the increase in aspect ratio.

The analytical model for the gradual expansion receiver is compared with the experimental data for  $\sigma=0.6$  and  $X_{sp}=3$  with an included angle of divergence of 4.5 degrees. The output characteristics for  $N_R' = 50, 72, 140$ , and  $200$  are compared with the experimental data in figures 23 and 24. In addition to the high-pressure recovery, high-flow recovery has been achieved as a result of the diffuser-like receiver.

### 3. LAMINAR PROPORTIONAL AMPLIFIER

With the development of an acceptable power jet representation, it is possible to investigate the governing relationships and associated design parameters between the power jet, control ports, and receivers. Of particular interest in many fluid power control applications are the jet deflection, blocked-load pressure gain, and output flow-pressure characteristics. The analytical models to predict these performance measures are developed in sections 3.1 to 3.4. The factors governing power amplifier design are discussed in section 3.5 and summarized in section 3.6.

Simson<sup>8</sup> has identified that the downstream control edge spacing,  $B_c$ , has a significant influence on the linearity of the relationship between the control flow,  $Q_c$  and the jet-edge pressure,  $P_j$  and that a linear relationship can be obtained by limiting  $B_c/2$  to one or less. In many applications, it is desired to have

---

<sup>8</sup>A. K. Simson, A Theoretical Study of the Design Parameters of Subsonic Pressure Controlled Fluid Jet Amplifiers, Ph.D Thesis, Department of Mechanical Engineering, MIT (July 1963).

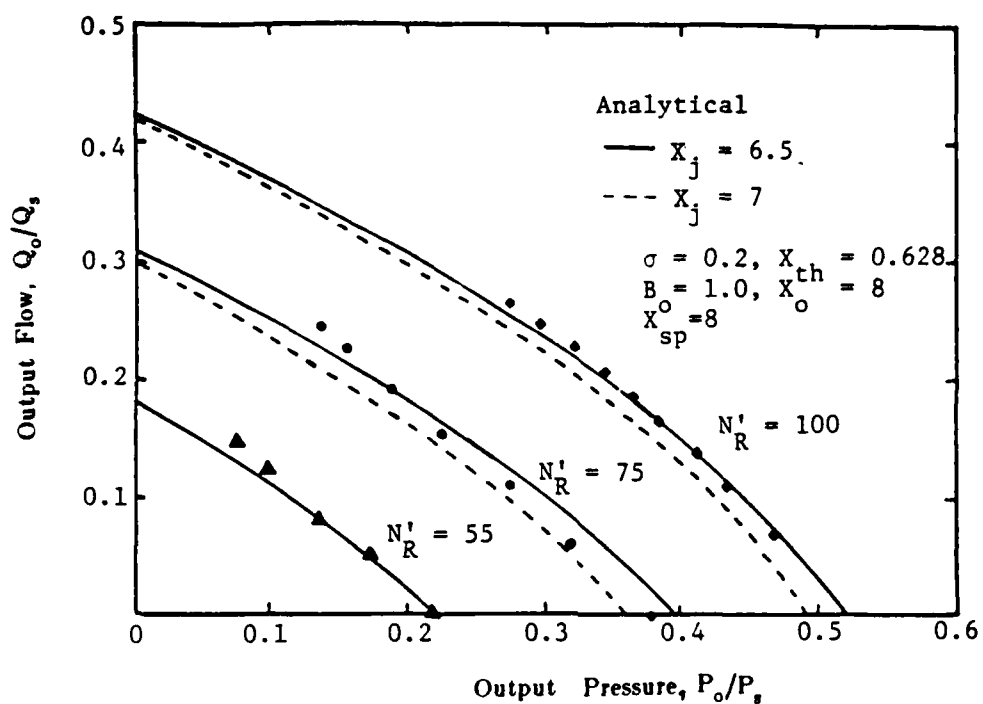


Figure 19. Comparison of output characteristics between analytical and experimental data;  $\sigma=0.2$ ,  $X_{sp}=8$ .

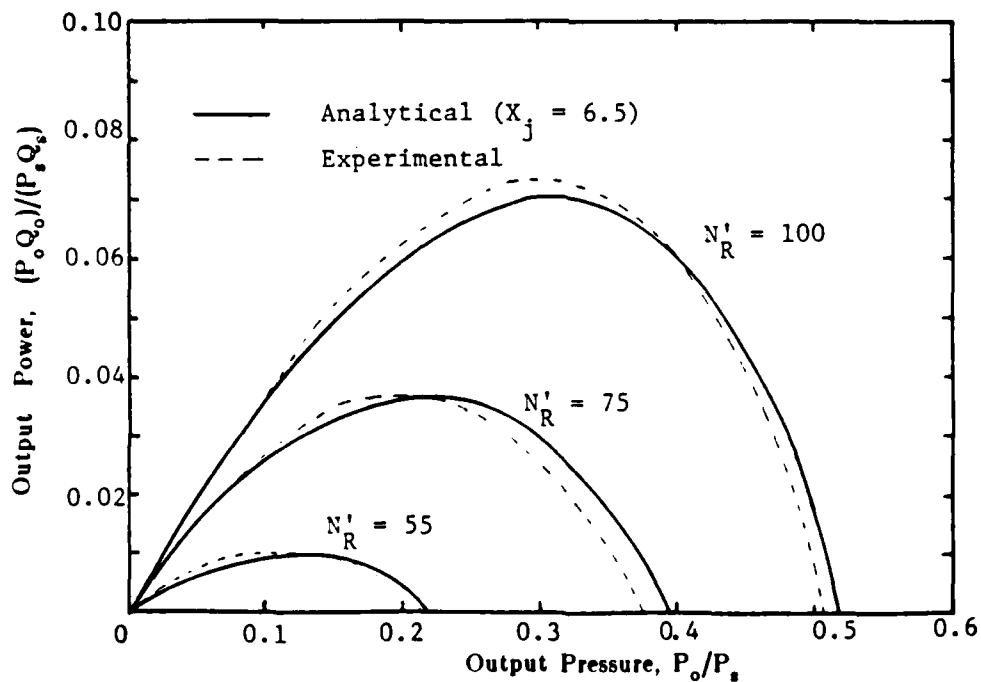
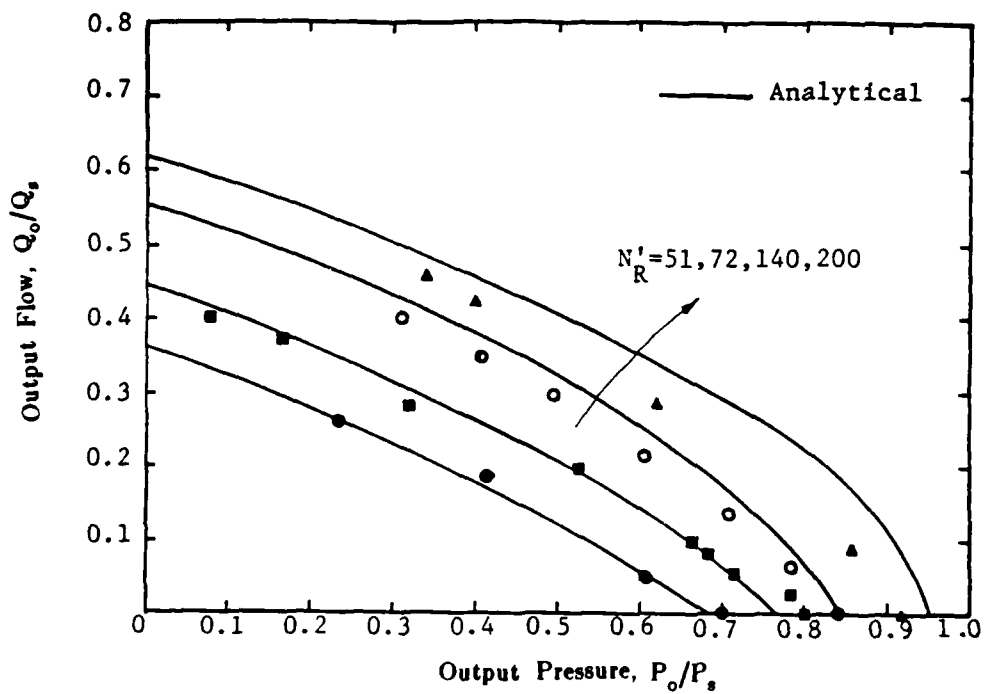
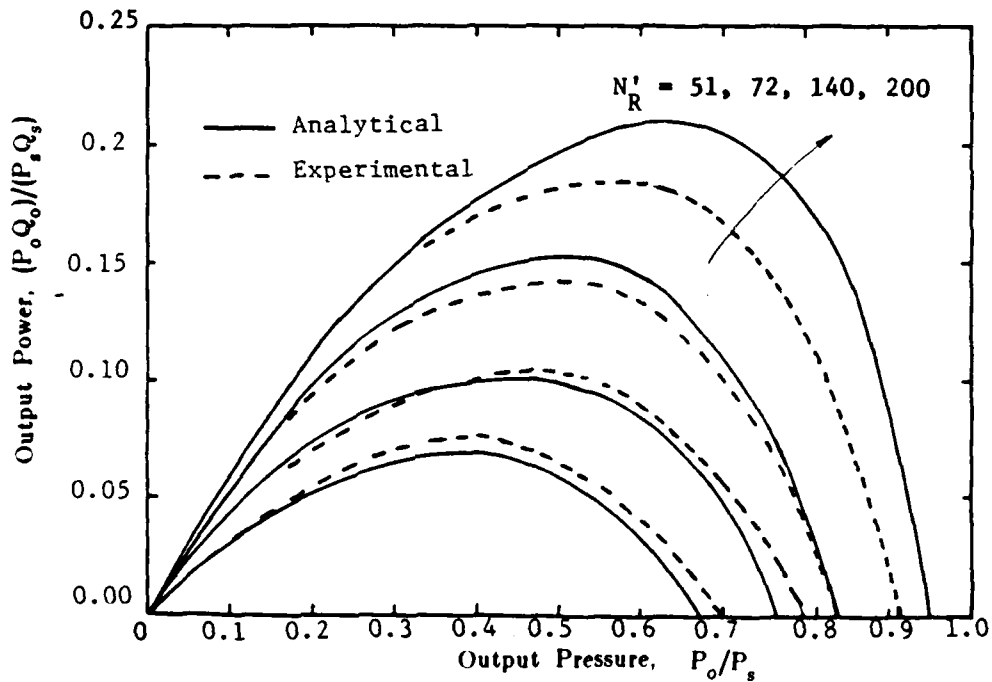


Figure 20. Efficiency of nozzle/jet/receiver system;  $\sigma=0.2$ ,  $X_{sp}=8$ .



**Figure 21.** Comparison of output characteristics between analytical and experimental data;  $\sigma=0.6$ ,  $X_{sp}=3$ .



**Figure 22.** Efficiency of nozzle/jet/receiver system;  $\sigma=0.6$ ,  $X_{sp}=3$ .

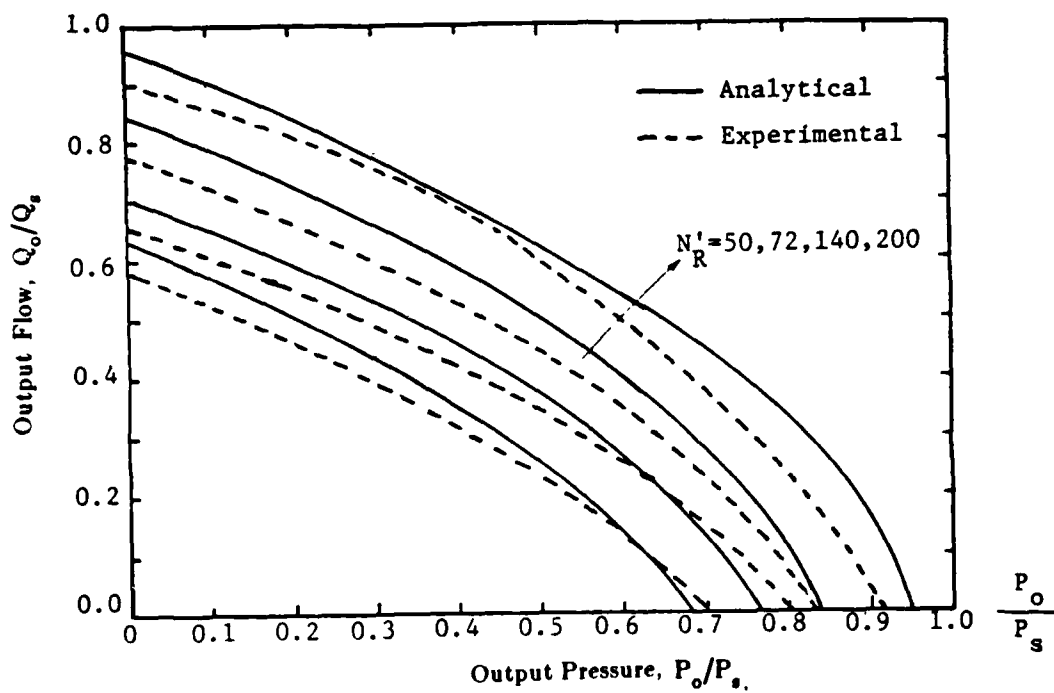


Figure 23. Comparison of output characteristics between analytical and experimental data; gradual expansion receiver.

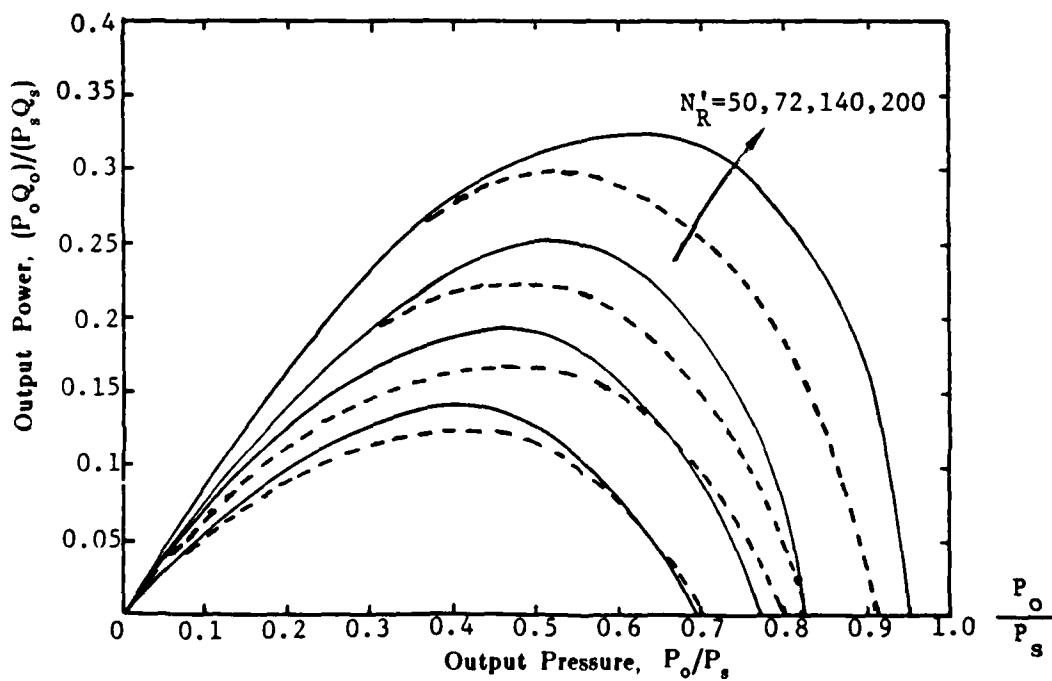


Figure 24. Efficiency of nozzle/jet/receiver system; gradual expansion receiver.

only a linear relationship between  $Q_c$  and  $P_j$  for a stable operating condition<sup>9</sup>. Hence, apart from the limitations (1) to (5) in section 2.4 on the design requirements and the operating conditions,  $B_t$  is limited to 2 or less as the linear input characteristic is desired for stable operating conditions.

### 3.1 Jet Deflection

Considering the basic geometry shown in figure 25, it is possible to develop a relationship between the pressures, power jet flow, and the jet radius of curvature. If frictionless and incompressible flow is assumed, the normal component of the Euler's equation in streamline coordinates is

$$\frac{\partial P}{\partial r'} = \rho \frac{u^2}{r} \quad , \quad (25)$$

where  $r$  is the radius of curvature of the jet. Integrating equation (25) over the cross-sectional area at the nozzle exit, the radius of curvature of the jet can be written in the normalized form as

$$\frac{r}{b_s} = -2 \frac{J_s}{P_{jd}/P_s} \quad , \quad (26)$$

where the following terms are defined :

$$J_s = C_d^2 \int_{Z=0}^1 \int_{Y=0}^1 U^2 dY dZ \quad , \quad (27)$$

and

$$\frac{P_{jd}}{P_s} = \frac{P_{jl} - P_{jr}}{P_s} \quad . \quad (28)$$

From the basic geometry, the radius of curvature can be written as

$$\frac{r}{b_s} = \frac{\{1 + DY^2\}^{3/2}}{-D^2Y} \quad , \quad (29)$$

where

$$DY = \frac{dY}{dX} \quad , \quad \text{and} \quad D^2Y = \frac{d^2Y}{dX^2} \quad .$$

Substituting the radius of curvature from equation (26) into equation (29), the jet deflection can be computed numerically as a function of jet momentum and the jet-edge pressure differential,  $P_{jd}$ . For a small deflection, the jet deflections at the downstream control edge and at the leading edge of the splitter are

<sup>9</sup>J. M. Kirshner and S. Katz, Design Theory of Fluidic Components, Academic Press (1975).

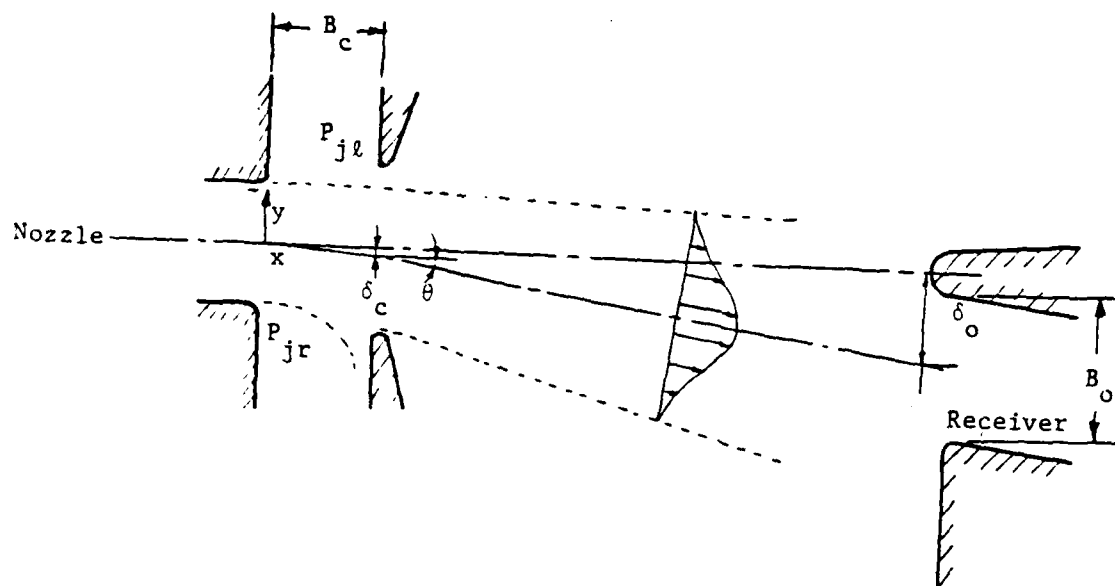


Figure 25. Power jet deflection schematic.

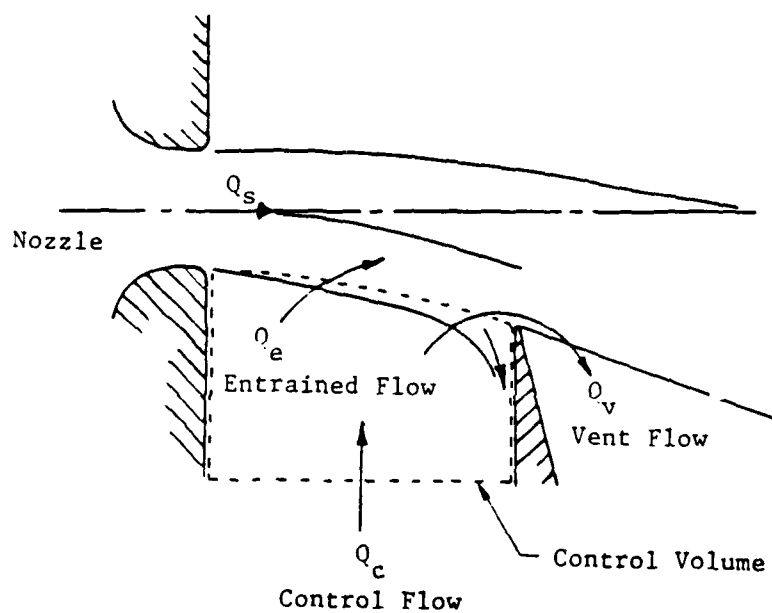


Figure 26. Flow component representation schematic.

$$D_c = \frac{\delta_c}{b_s/2} = 0.5 \frac{B_c^2 P_{jd}}{J_s P_s},$$

$$D_o = \frac{\delta_o}{b_s/2} = 0.5 \left(2 \frac{X_{sp}}{B_c} - 1\right) \frac{B_c^2 P_{jd}}{J_s P_s}. \quad (31)$$

Hence, the normalized jet deflection,  $D_c$ , is linearly proportional to the normalized jet-edge pressure differential and the proportionality is a function of  $B_c^2$  and the momentum flux at the nozzle exit.

### 3.2 Input Characteristics

The flow processes associated with the input characteristics are the flow through the control port channel and that interacting with the power jet. It is assumed that the increase in one control port pressure is accompanied by a corresponding decrease in the other control port pressure. On each side of the power jet, the control port pressure,  $P_c$ , can be related to the control flow,  $Q_c$ , with the jet edge pressure,  $P_j$ , as a parameter

$$P_c = P_j + R_c Q_c, \quad (32)$$

where  $R_c$  is the flow resistance of the control channel. The ratio of channel resistance to supply nozzle resistance is derived as a function of channel aspect ratio in appendix B. The control flow is assumed to be made up by the following flow components :

$$Q_c = Q_e - Q_r + Q_v, \quad (33)$$

where  $Q_e$ ,  $Q_v$  and  $Q_r$  are the entrained flow, vent flow, and return flow respectively. The definition of the various flow components is only an aid in analyzing the general control flow problem, and in many cases it is impossible to physically distinguish them. Each of the flow components has been determined<sup>7</sup> as a function of jet deflection which is expressed in terms of  $P_{jd}$ . Hence, the control flow can then be computed from equation (33) and the control pressure can be related to the control flow through equation (32)

<sup>7</sup>K-M Lee, Analytical and Experimental Development of a Laminar Proportional Amplifier for Power Modulation, Ph.D Thesis, Department of Mechanical Engineering, MIT (January 1985).

### 3.3 Blocked Load Characteristics and Pressure Gain Analysis

The blocked-load characteristic discussed in this section is defined as the relationship between the output and control pressure differential. The jet deflection has been expressed as a function of control pressure differential.

From section 2.4, the maximum pressure recovery obtainable for the single receiver configuration is

$$P_{\max} = \frac{4C_d^2 \alpha_j}{\beta B_o}, \quad (34)$$

where

$$\alpha_j = \int_{Z=0}^1 \int_{Y=0}^{\infty} U^2|_{X_j} dYdZ. \quad (35)$$

The output differential pressure can be obtained as

$$\frac{P_{od}}{P_{\max}} = \pm C_{sp} \frac{\alpha_D}{\alpha_j}, \quad (36)$$

where  $C_{sp}$  is the splitter loss coefficient which has been approximated by the two dimensional impingement of uniform flow on the leading edge of the circular cylinder as described by Lee<sup>7</sup> and where

$$\alpha_D = \int_{Z=0}^1 \int_{Y=0}^{D_o} U^2|_{X_j} dYdZ \quad (37)$$

The blocked-load differential pressure gain is defined as

$$G_p = \left. \frac{\partial P_{od}}{\partial P_{cd}} \right|_{P_{cd}, Q_o=0} \quad (38)$$

or

$$\left. \frac{\partial P_{od}}{\partial P_{cd}} \right|_{P_{cd}, Q_o=0} = \left[ \frac{\partial P_{od}}{\partial D_o} \frac{\partial D_o}{\partial D_c} \frac{\partial D_c}{\partial P_{jd}} \frac{\partial P_{jd}}{\partial P_{cd}} \right] \Big|_{P_{cd}, Q_o=0} \quad (39)$$

As seen from equation (39), the problem of determining the differential gain is reduced to one of deriving the individual gain components from sections 3.1, 3.3 and 3.3 and combining the results.

---

<sup>7</sup>K-M Lee, Analytical and Experimental Development of a Laminar Proportional Amplifier for Power Modulation, Ph.D Thesis, Department of Mechanical Engineering, MIT (January 1985).

### 3.4 Output Characteristics

The analytical model in section 2.4 of the nozzle/jet/receiver system is modified and applied in the following discussion to predict the output characteristics. The analysis is limited to the case of positive flow into the receivers and does not consider variation due to the negative flows coming back out of the receivers. As the included angles of expansion for the LPA receivers are generally small, the solution of Cheng's<sup>10</sup> correlation factor is used to account for the effect of curvature. The effect of the curvature on  $K_{fd}$  is assumed to be negligible for the range of Reynold's number encountered. The friction factor and  $K_{fd}$  are computed based on the constant width or gradual expansion channel model.

The output characteristics can be computed from equation (18). However,  $P_m$  is now dependent on the jet deflection. At a fully deflected jet position, a certain fraction of the jet momentum may miss the receiving channel. The peak pressure,  $P_m$ , of the pressure profile becomes

$$\frac{P_m}{P_{\max}} = \frac{1}{2} C_{sp} \left( 1 + \frac{\alpha_D}{\alpha_j} \right), \quad (40)$$

where  $P_{\max}$  is the maximum pressure obtainable for a single receiver in the absence of a splitter.

Due to the non-uniformity and asymmetry of the inlet velocity profiles at the centered jet position, the influence of the spill back momentum must be considered. The velocity profile in the spill back flow is assumed to be of the form

$$U_{sp} = \frac{3}{2} \frac{1}{B_o} \left( \frac{0.5Q_j - Q_o}{Q_s} \right) (1 - Z^2), \quad (41)$$

where  $Q_j$  is the volumetric flowrate jet at  $X=X_j$ . The corresponding maximum pressure,  $P_m$  for the pressure profile becomes

$$\frac{P_m}{P_s} = 2 \frac{C_d^2 C_{sp} \alpha_j}{\beta B_o} + \frac{8 C_d^2 B_o \sin \phi}{\beta} \int_{Z=0}^1 U_{sp}^2 dZ, \quad (42)$$

where  $\phi$  is the angle of spill back flow measured clockwise from the axis perpendicular to the direction of flow. Dividing equation (42) through by  $P_{\max}/P_s$ ,

$$\frac{P_m}{P_{\max}} = \frac{1}{2} C_{sp} + \frac{24}{5} \left( \frac{0.5Q_j - Q_o}{Q_s} \right)^2 \sin \phi, \quad (43)$$

$P_r/P_s$  can be obtained by substituting  $P_m/P_s$  from equation (40) for fully developed jet or equation

<sup>10</sup>Cheng et al, Fully Developed Flow in Curved Rectangular Channels, Trans ASME, Journal of Fluids Engineering, Ser. I 98-1, Pg. 41, (March 1979).

(43) for center-jet into equation (23). The output characteristic can then be computed by equation (18). The value of  $\phi$  is determined experimentally.

### 3.5 Design Considerations

In general, the splitter radius and the downstream control edge corners of the prototype LPA are limited by manufacturing processes. In the following discussion, the minimum radius for a prototype amplifier device is assumed to be 0.095mm (0.00375 in.) based on 347 stainless steel.<sup>11</sup> The model test amplifier is five time larger than the prototype device.

The objective of the design is to achieve a high-power-to-weight ratio for a given supply power input, to reduce temperature sensitivity and to increase the laminar operating range of the amplifier subjected to the constraints due to the fluid properties and the C-Format geometry. The design procedure is outlined as follows :

1. The geometry related to the jet interference region is determined so that the maximum pressure recovery can be obtained.
2. The supply duct length and the receiver shape are determined so that flow recovery is optimized. The diverging angle, the duct length, and the radius of curvature of the receivers are dependent on the length of the supply duct.
3. Finally, the downstream control edge spacing and the geometry of the control port are chosen to match the desired input impedance.

#### 3.5.1 Effect of $X_{sp}$ and $B_c$

The characteristic dimensions  $X_{sp}$  and  $B_c$  can effect one or all of the following characteristics, the maximum pressure recovery, the jet edge pressure differential required to fully deflect the jet, the pressure gain and the bias sensitivity on the pressure gain, which are related to the blocked-load characteristics. However, the geometry related to the jet interaction region can be designed independent of the C-Format geometry.

The dimension  $X_{sp}$  consists primarily of the downstream control port width,  $B_c$ , the radius of the corner at downstream control edges and the vent width measured along the line of symmetry. The vent should be sufficiently wide so that the quiescent flow can be properly drained at blocked-load. The minimum acceptable radius for downstream control edge corners is primarily limited by the

---

<sup>11</sup>L. E. Scheer and J. Joyce, Manufacturing Techniques for reducing High Quality Fluidic Laminates in Production Quantities, 20th Anniversary of Fluidic Symposium (November 1980).

manufacturing processes. It has been found that the bias sensitivity can be significantly minimized by reducing  $B_c$ .<sup>2,12</sup>

The maximum deflection for specified  $B_{sp}$  and  $B_o$  is provided by the jet edge pressure differential,  $P_{jdm}$ , across the jet.  $P_{jdm}$  can then be related to the control pressure differential in terms of the control port geometry and the distance between the downstream control edges,  $B_c$ . Typical data for  $P_{jdm}$  as a function of  $B_c$  and  $X_{sp}$ , computed based on  $B_o$  equal to 1.0 and  $B_{sp}$  of 0.25 and 0.5, are shown in figure 27. The value of  $J_s$  varies from 0.5 to 0.625 corresponding to  $N_R$  from 50 to 150. The data illustrate that the input effort increases significantly with the decrease in  $B_c$ . To obtain a high pressure recovery, the receiver must be placed as close as possible to the nozzle exit. Therefore, the trade-off for a maximum output pressure,  $P_{om}$ , with a lowest maximum input jet edge pressure differential,  $P_{jdm}$ , should be considered in terms of  $X_{sp}$  and  $B_c$ .

The constraints imposed by the geometry, input pressure differential allowable and the bias sensitivity on the design of the jet interaction region are illustrated in figure 28. Hence,  $X_{sp}$  is chosen to be 3 corresponding to  $B_c=1$  to minimize the Reynold's number sensitivity and to maximize pressure recovery with a maximum jet-edge pressure differential of 25%  $P_s$  required to fully deflect the jet.

### 3.5.2 Effect of Supply Duct and Receiver Geometries

The ratio of the power recovered in the receiver to the power available at the input of the supply duct can be expressed as

$$\frac{P_o}{P_s + \Delta P_s} \frac{Q_o}{Q_s} = \frac{P_s}{P_s + \Delta P_s} \frac{P_o P_r Q_o}{P_r P_s Q_s} \quad (44)$$

where  $\Delta P_s$  is the pressure drop along the supply duct. The ratio  $P_r/P_s$  is independent of the C-Format constraints for a specified outlet flow. Therefore, to optimize the power recovery, the ratios  $P_s/(P_s + \Delta P_s)$  and  $P_o/P_r$  should be optimized at any loading condition. The ratio  $P_s/(P_s + \Delta P_s)$  is related to the supply nozzle configuration and the ratio  $P_o/P_r$  is primarily a function of the receiver geometry, receiver inlet velocity profile uniformity and the flow Reynold's number of the receiver.

The constraints imposed by the C-Format laminate are illustrated in figure 29 and 30. Figure 29

<sup>2</sup>F. M. Manion and T. M. Drzewiecki, Analytical Design of Laminar Proportional Amplifiers, HDL Fluidic State-of-the-Art (October 1974).

<sup>12</sup>G. Mon, Fluoric Laminar Gain Blocks and an Operational Amplifier Scaler. Technical Report HDL-TR-1730, Harry Diamond Laboratories (December 1975).

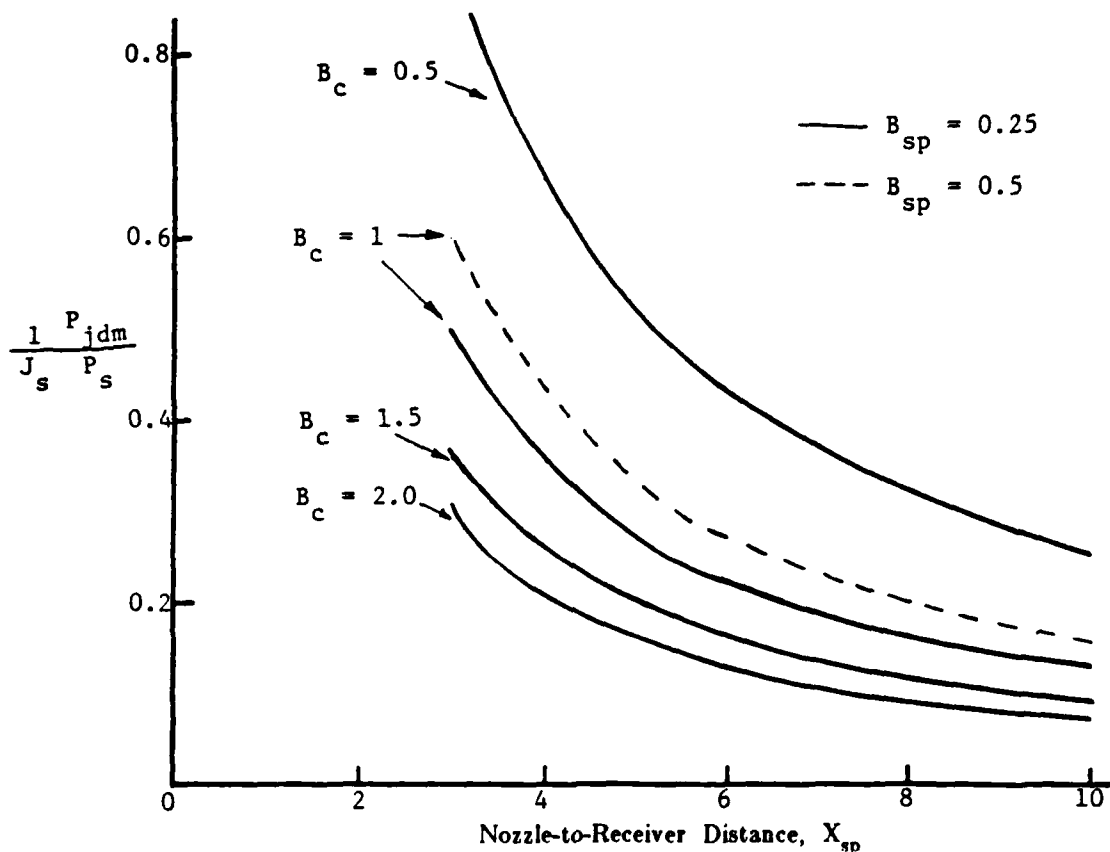


Figure 27. The effect of  $B_c$  on maximum jet edge pressure differential,  $P_{jdm}$ .

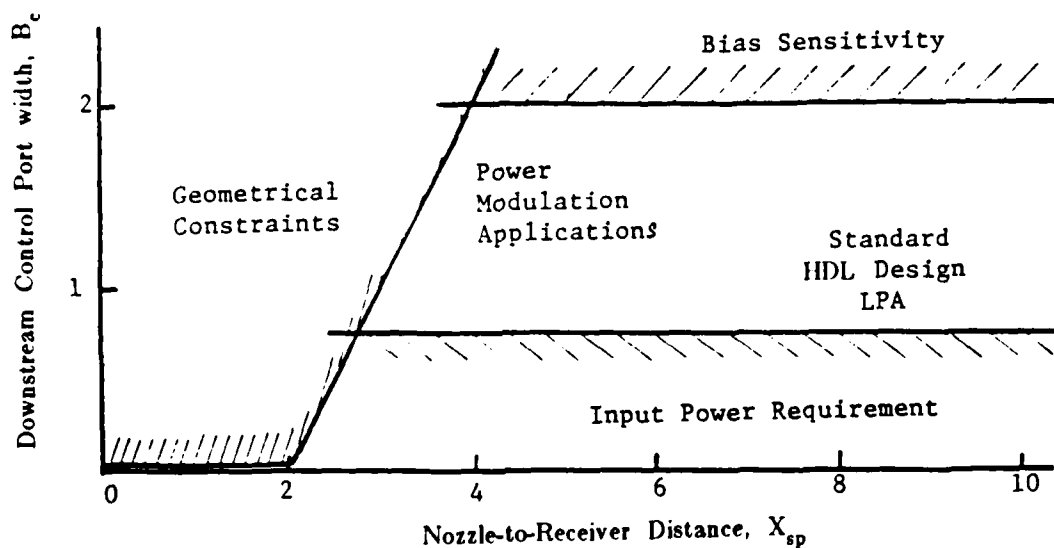
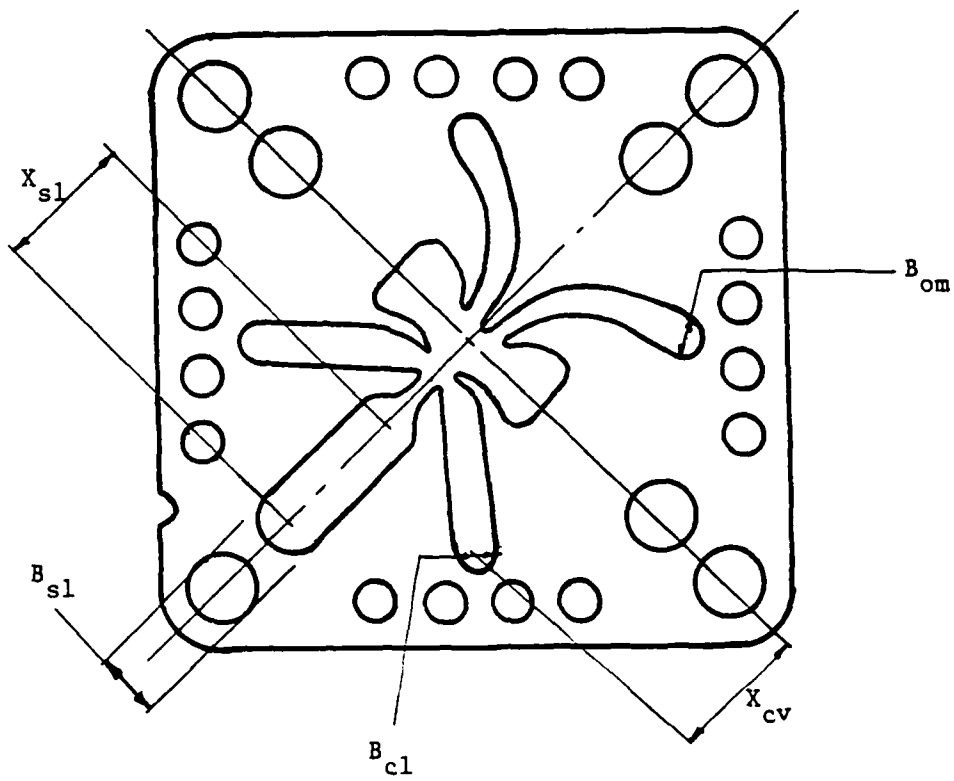
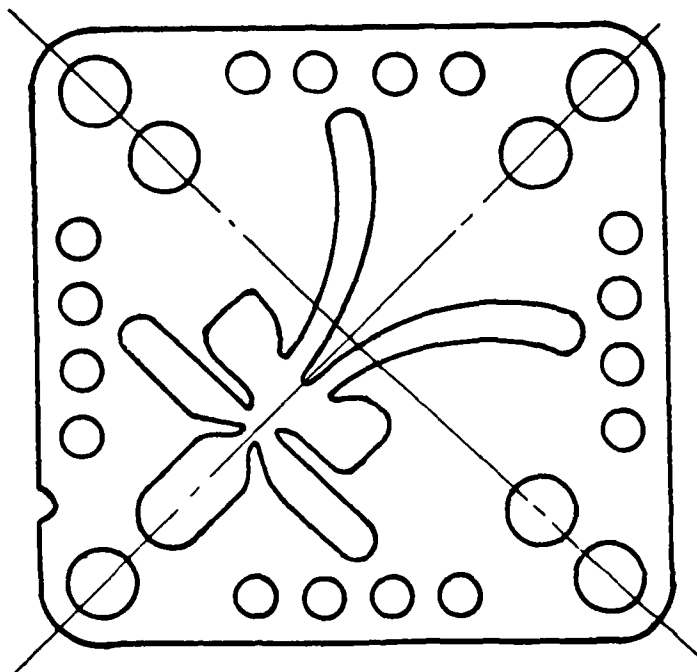


Figure 28. The effect of constraints on the selection of  $B_c$  and  $X_{sp}$ .



**Figure 29.** The conventional C-format amplifier design.



**Figure 30.** The offset C-format amplifier design.

shows a typical conventional design which has the center-line of the vent aligned with a diagonal of the C-Format laminate. The design results in long supply and control channels and a pair of short but curved outlet receivers. As a result, the receivers are shaped with an average included expansion angle of 2.0 to 3.0 degrees and, in general, accompanied with a small radius of curvature. The friction factor for the curved duct is higher than that of a straight duct, although the additional pressure drop associated with the effect of receiver curvature may be neglected for the case of low Reynolds number flow as encountered in the conventional LPA for signal processing applications. Figure 30 shows a different design in which the center-line of the vent is offset from the diagonal of the laminate. The second design intentionally shows the shortest possible supply and control ports and a pair of long gradual expansion diffusers. It is believed that an optimal design can be obtained between these limits.

Two particular receiver configurations, corresponding to the prototype device with  $b_s = 0.75\text{mm}$  (0.03 inch), have been considered as follows .

1. The width at the receiver outlet is designed to be 3 times  $b_s$ , which is equal to the outlet port diameter in the C-Format laminate. The included angle of divergence and the radius of curvature are then calculated as a function of  $X_{s1}/B_{s1}$ .
2. The maximum allowable width of the receiver outlet is considered to be 4.7 times  $b_s$ , which is equal to the supply port diameter on the C-Format laminate. The included angle of divergence is designed to be 6 degrees initially and the corresponding width at the receiver outlet and the radius of curvature are then calculated as a function of  $X_{s1}/B_{s1}$ . If the width of the receiver outlet is larger than  $4.7b_s$ , the included angle is re-calculated based on the maximum width at the receiver outlet.

The product of the two factors,  $P_s/(P_s + \Delta P_s)$  and  $P_o/P_r$ , is shown in figure 31 for  $B_o=1$ ,  $X_{sp}=3$ ,  $\sigma=0.6$  and  $X_{th}=0.628$  at  $N_R'$  of 50 and 200. The outlet flow condition is chosen around the point of maximum efficiency. For the first configuration which has a small included angle of 3 degrees, the result is insensitive to  $X_{s1}/B_{s1}$  at  $N_R' = 50$ . It is worth noting that the pressure drop is larger at  $N_R' = 200$  than that at  $N_R' = 50$  due to the effect of curvature. The overall pressure drop is significantly lowered by an increase in the included angle from 3 to 6 degrees and an increase in the radius of receiver curvature. For  $X_{s1}/B_{s1}$  between 0.5 and 1.5, the pressure drop of the second configuration is insensitive to the variation of  $X_{s1}/B_{s1}$ .

### 3.5.3 Effect of Control Edge Spacing and Control Port Geometry

Much work has been done by Simson<sup>8</sup> on the downstream control edge shape to distinguish the proportional amplifier from the wall attachment digital amplifier.

---

<sup>8</sup>A. K. Simson, A Theoretical Study of the Design Parameters of Subsonic Pressure Controlled Fluid Jet Amplifiers, Ph.D Thesis, Department of Mechanical Engineering, MIT (July 1963).

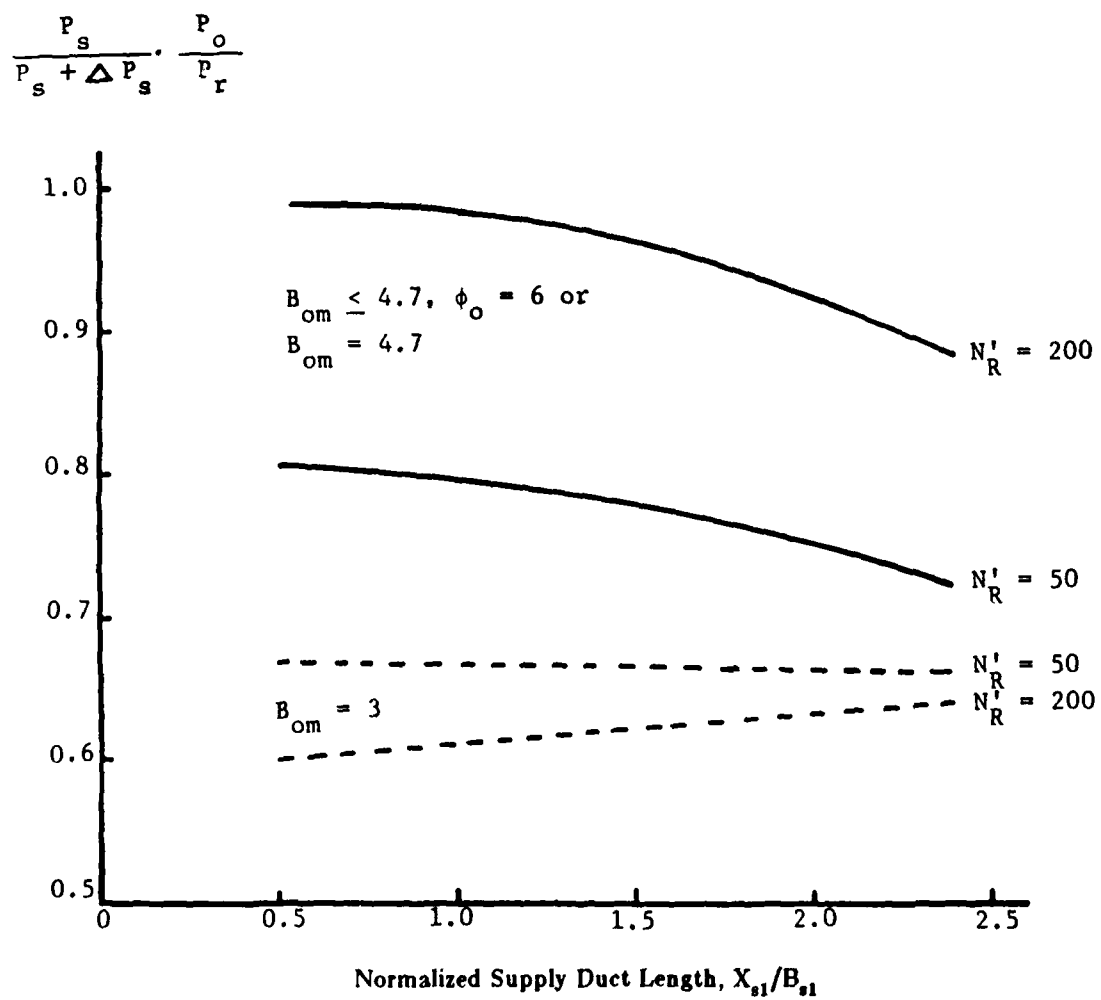


**Figure 31.** Effect of supply duct length.

For proper operation of an amplifier, it is normally desired that the downstream control edge spacing should not affect the motion of the power jet. If the downstream control edge spacing is too small, the return flow may carry sufficient momentum to cause the power jet to be significantly deflected from its expected direction and the desired maximum deflected jet position may not be obtainable. On the other hand, a sufficiently large control edge spacing is generally desired such that a linear input characteristic and a flat output saturation characteristic can be obtained.

In general, the control port geometry should be shaped to reduce temperature sensitivity and to optimize the ratio,  $P_j/P_c$ . The overall design goal is to match the input impedance which may be specified by the application requirement.

### 3.6 Design Summary

The geometries related to the jet interaction region and the influence of the C-Format configuration on LPA design have been discussed. In the jet interaction region, the trade-off between  $X_{sp}$  and  $B_c$  have been determined with  $B_{sp}$  and  $B_o$  as parameters to achieve high pressure recovery for power modulation applications and to minimize the bias sensitivity and the jet-edge differential pressure required to fully deflect the jet. The splitter width,  $B_{sp}$ , is chosen to decouple the outlet receivers for a high outlet differential pressure obtainable and is limited by the allowable jet-edge differential pressure at the fully deflected jet position. The influence of the C-Format geometry on LPA design has been expressed as a function of supply duct length. It has been shown that power recovery can be optimized by properly designing the vent location to allow a large receiver radius of curvature and to have a pair of diffuser-like receivers. For power modulation applications,  $X_{sp}$  and  $B_c$  are selected to be 3 and 1 respectively corresponding to  $B_{sp}=0.5$  and  $B_o=1.25$ . The width of the receiver outlet is designed to be 4.7 times  $b_s$  to allow for approximately 6 degrees of diverging angle, which corresponds to a prototype C-Format LPA of  $b_s$  of 0.095 mm. For  $X_{s1}/B_{s1}$  between 0.5 and 1.5, optimum power recovery can be obtained.

## 4. LPA CONFIGURATIONS AND PERFORMANCE EVALUATION

The LPA configuration designed for power modulation was constructed and tested. The objectives of the tests are to evaluate the characteristic performance of the new LPA configuration and to provide a basis for comparison between the analytical prediction with the experimental evaluation. A standard HDL design LPA was tested to serve as a basis for comparison.

The LPA static characteristics determined in the tests are the blocked-load characteristics and output flow-pressure characteristics with the modified Reynold's number as an input parameter. The static tests were conducted on model LPA's which are five times larger than the prototype C-Format geometry. For

dynamic response, the frequency response of blocked load pressure gain was obtained experimentally using the prototype C-Format LPA with  $b_s$  equal to 0.75 mm (0.03 in.).

The LPA configuration and construction are described in section 4.1, and a general performance evaluation using conventional parameters between the new LPA configuration and the standard HDL design LPA, is discussed section 4.2.

#### 4.1 LPA Configurations and Construction

Two LPA configurations are considered in this investigation; namely, a power modulation LPA which was designed using the procedure outlined above and a standard HDL design LPA which is used as a basis for comparison. The characteristic dimensions of the model LPA's are summarized in table 2. The schematics of the power modulation LPA and standard HDL C-Format LPA are shown in figures 32 and 33 respectively.

The power modulation LPA was designed with a computer-aided-graphics technique to allow easy variation of the characteristic dimensions and shape. Numerical machining techniques have been used to manufacture the model amplifier, vents, and exhausts. The model amplifier which is five time larger than the standard prototype C-Format laminate is machined out of 1.5625 mm (1/16 in.) Lexan sheet. Lexan sheet was chosen for the amplifier due to its mechanical strength so that the thin sections near the downstream control edges and the splitter can be machined without breaking the part. The corresponding model vents and exhausts are machined out of 3.125 mm (1/8 in.) and 6.25 mm (1/4 in.) plexiglass respectively.

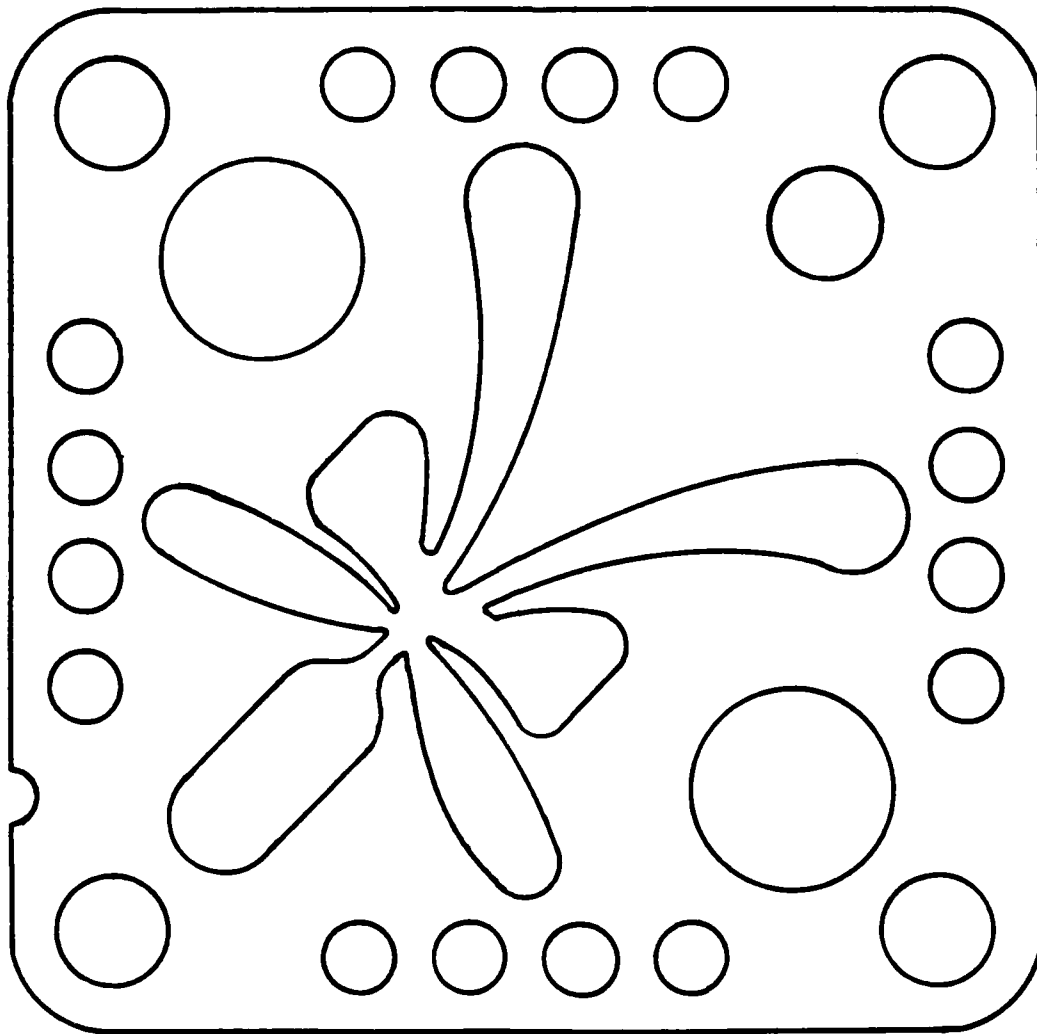
#### 4.2 Performance Evaluation

For purposes of comparison, the amplifiers are designed at 27 C with the same supply pressure corresponding to  $N_R'$  of 75 and 100 respectively for the traditional HDL design LPA and the power modulation LPA respectively. The  $N_R'$  is selected somewhere in the middle of the laminar operating range so that the amplifier is operational over a range of temperatures. The performance characteristics of the LPA's were determined experimentally. Throughout the experiments, the temperature was carefully regulated to maintain a constant predetermined value. A schematic of the experimental apparatus used to determine the blocked-load and output characteristics of the LPA's is shown in figure 34. Figure 35 shows the schematic and the stacking order of the components which make up the complete amplifier test section.

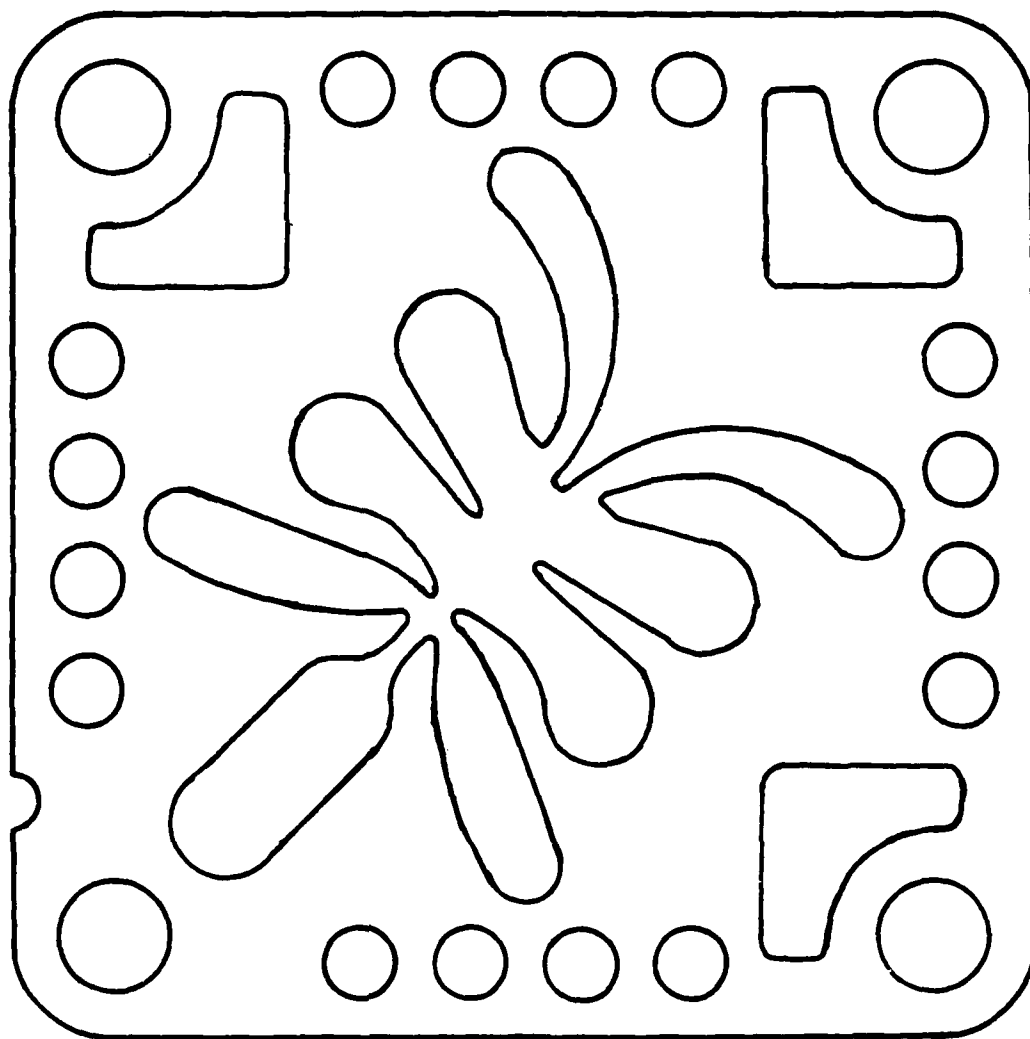
The output characteristics of the LPA's were obtained experimentally at a temperatures 28.9 C and at

TABLE 2. CHARACTERISTIC DIMENSIONS OF MODEL LPA

Port	Dimension	Power Modulation LPA	Standard HDL LPA
Nozzle	$b_s$	3.75 (0.15 inch)	3.75
	$\sigma$	0.4	0.4
	$x_{th}$	0.6	1.25
Control	$B_c$	1.0	1.0
	$x_c$	10.39	10.67
	$B_t$	1.75	1.20
	$x_{sp}$	3	8
	$B_{sp}$	0.5	0.667
Outlet	$B_o$	1.25	1.267
	$x_o$	16.38	12.69
	$B_{o2}$	4.686	3
	$R_{cur}$	27.36	9.17



**Figure 32.** C-format power modulation LPA schematic.



**Figure 33.** C-format standard HDL design LPA schematic.

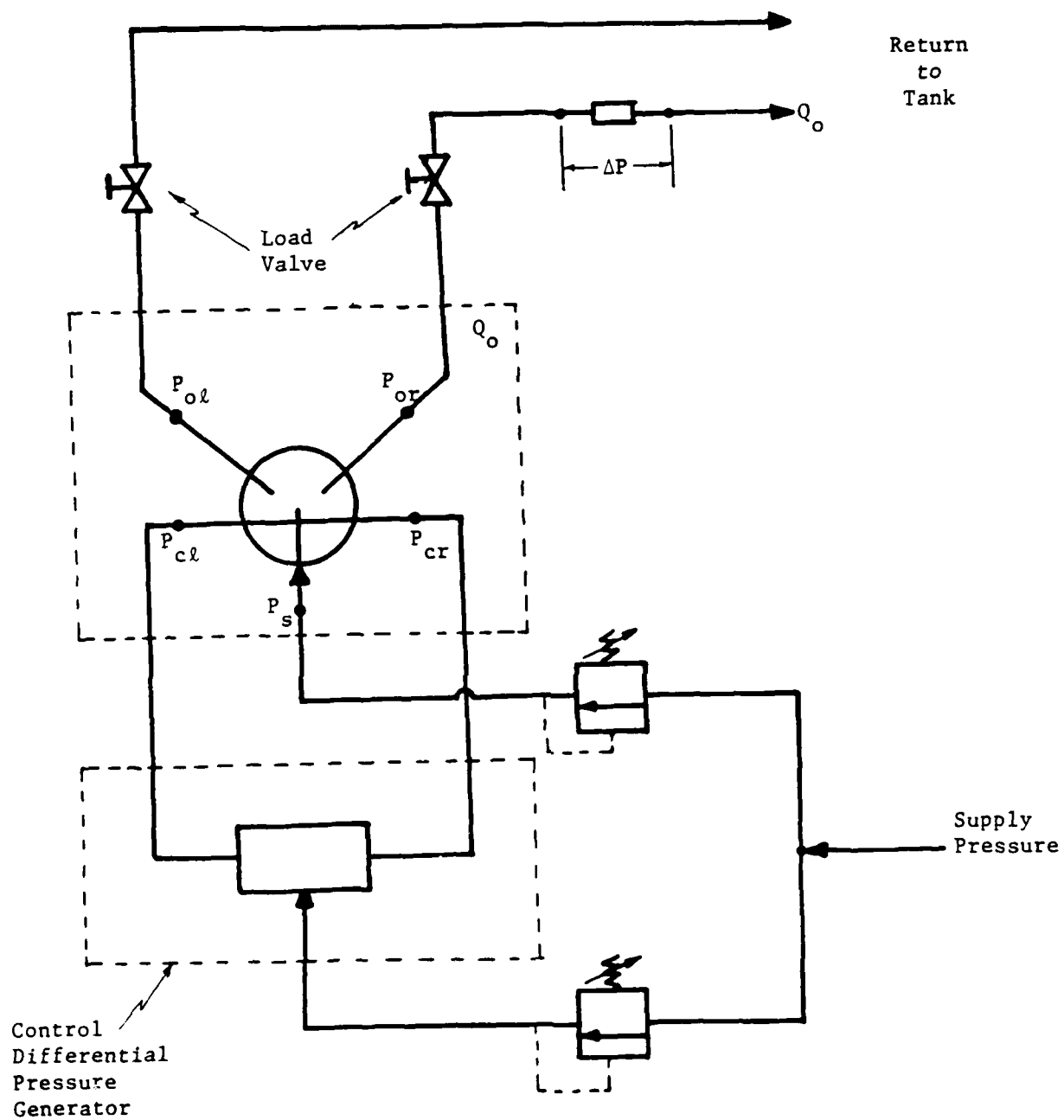


**Figure 34.** Experiment schematic.

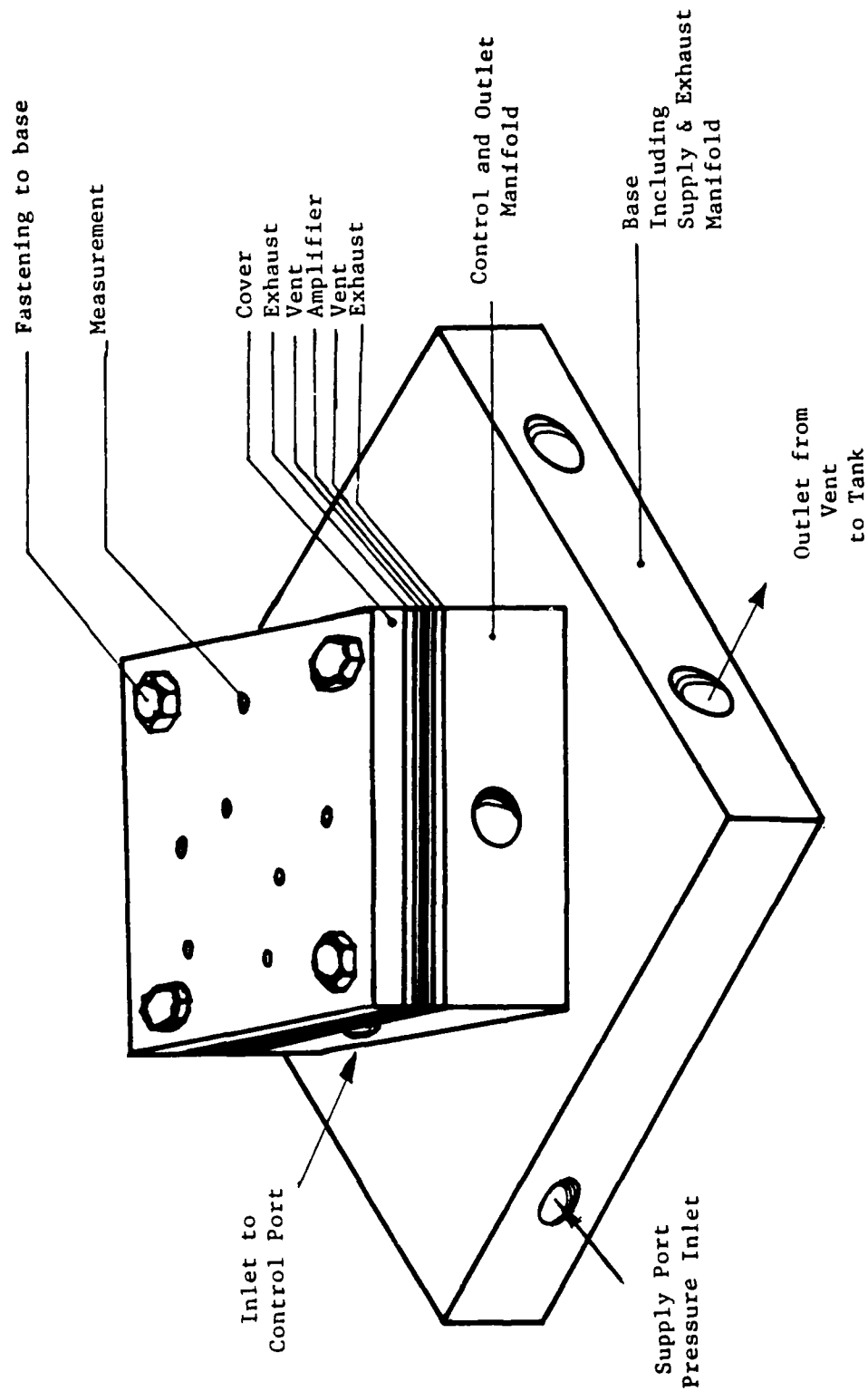


Figure 35. Amplifier test section schematic.

a supply pressure of 60 KPa. The comparison between the analytical and the experimental output characteristics and the efficiency are plotted in figures 36 and 37 for the Power Modulation LPA and in figures 38 and 39 for the standard HDL design LPA. The spill back angle,  $\phi$ , has been determined to be 15 degrees for the power modulation LPA and 5 degrees for the standard HDL design LPA.

#### 4.2.1 Influence of Modified Reynold's Number

The blocked-load characteristics of the power modulation LPA are obtained at two different temperatures of 28.9 C (84 F) and 60 C (140 F) and at  $N_R' = 50, 100, 150, 172$  and 203. The comparison of blocked-load characteristics between the experimental data and the analytical predictions are shown in figure 40. The blocked-load characteristic is linear if the control differential pressure is within 20 percent of the supply pressure and the slope of the blocked-load characteristic decreases beyond that point. For a change of  $N_R'$  from 50 to 200, the normalized saturation outlet differential pressure varies from 0.4 to 0.6 and the saturation control differential pressure varies from 0.225 to 0.3.

Similarly, the experimental data of blocked-load characteristics of the traditional LPA were taken at a temperature of 27 C and at the  $N_R' = 50, 72$  and 100. They are compared with the predictions in figures 41 and 38. The blocked-load characteristic is linear if the control differential pressure is within 5 percent of the supply pressure. Unlike the power modulation LPA, the pressure gain of the traditional amplifier increases as the modified Reynold's number increases.

The comparisons of the blocked-load pressure gain and recovery of the two LPA configurations are shown in figures 42 and 43. The blocked-load performance of the power modulation LPA, with short  $X_{sp}$  of 3, is characterized by high-pressure recovery and low-pressure gain but insensitivity to Reynold's number variation. On the other hand, the standard HDL design LPA is characterized by relatively low-pressure recovery and high-pressure gain, which are sensitive to a change of  $N_R'$ . The laminar operating range of the LPA has been extended beyond  $N_R' = 120$  by reducing  $X_{sp}$  from 8 to 3.

The analytically predicted output rating and efficiency of the two LPA's are tabulated in table 3. The output flow recovery of the power modulation LPA varies from 0.12 to 0.96 at  $N_R'$  of 25 to 200; whereas, that of the traditional design varies from near 0 to 0.66 at  $N_R'$  of 25 to 100. The maximum flow recovery obtainable has been increased by a factor of 1.5 over the traditional LPA. The maximum efficiency of the power modulation LPA varies from 13 percent at  $N_R'$  of 100 to 22.1 percent at  $N_R'$  of 200; whereas, that of the traditional HDL design LPA varies from 2.2 percent to 10.0 percent corresponding to  $N_R'$  of 50 to 100. In addition to the larger laminar operating range, the efficiency of the power modulation LPA is significantly higher than the standard HDL design LPA by a factor of more than 3 for  $N_R'$  less than 50 and a factor of about 2 near the upper limit of laminar operating range. The

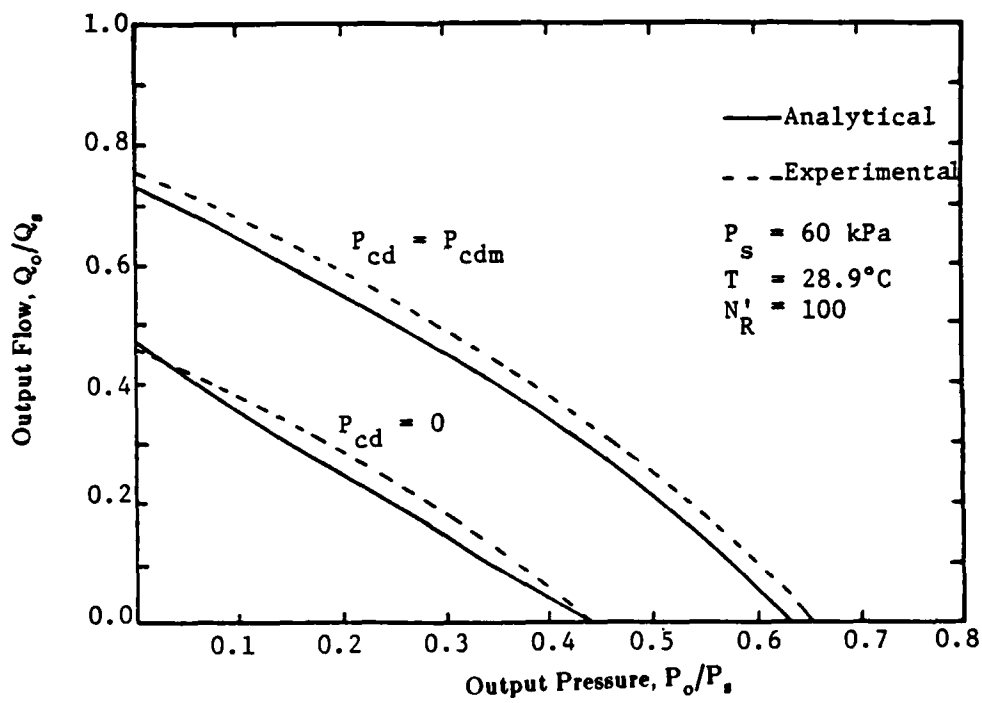


Figure 36. Comparison of output characteristics at  $N_R' = 100$ .

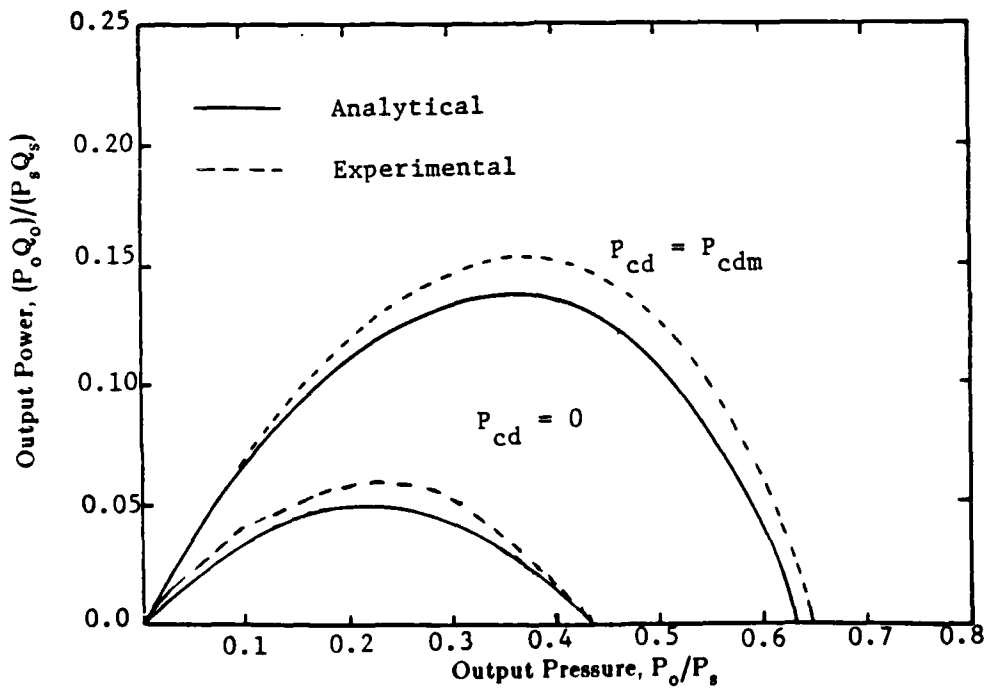


Figure 37. Efficiency of power modulation LPA at  $N_R' = 100$ .

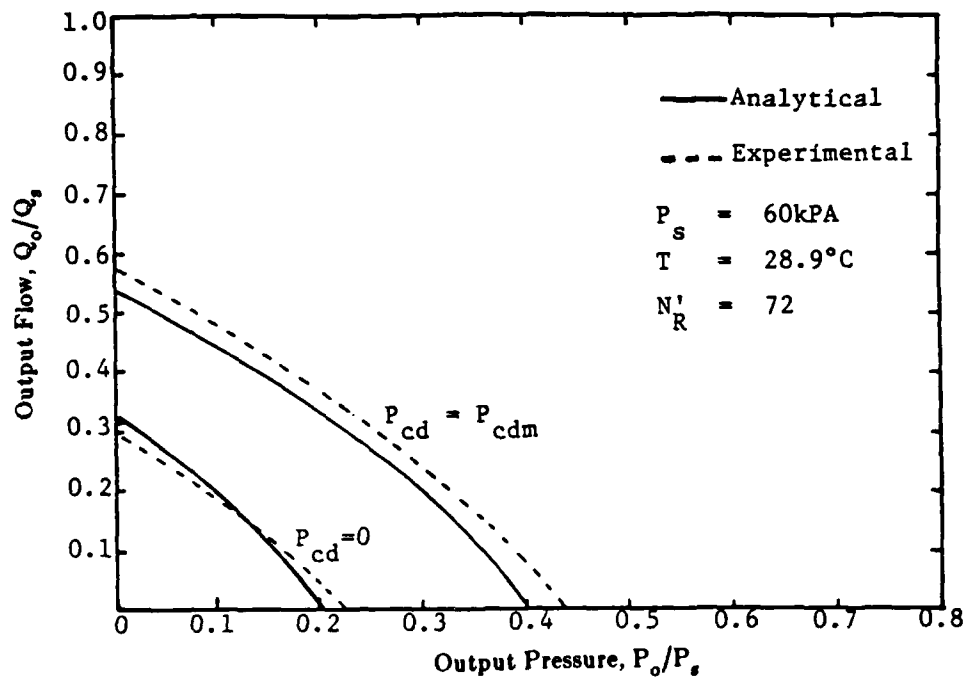


Figure 38. Output characteristics of traditional HDL design LPA.

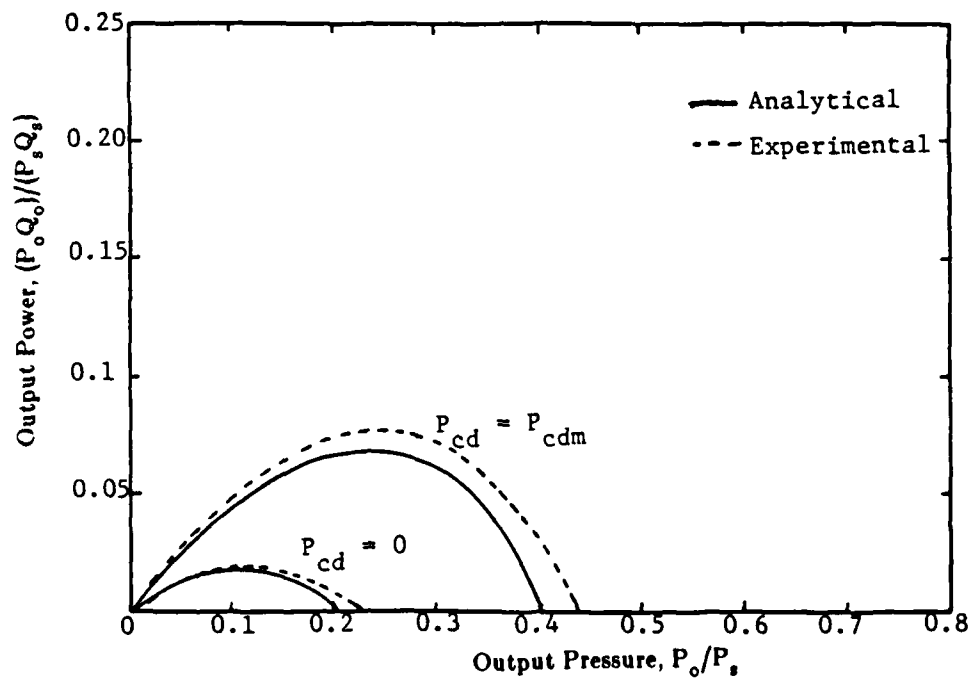


Figure 39. Efficiency of traditional HDL design LPA.

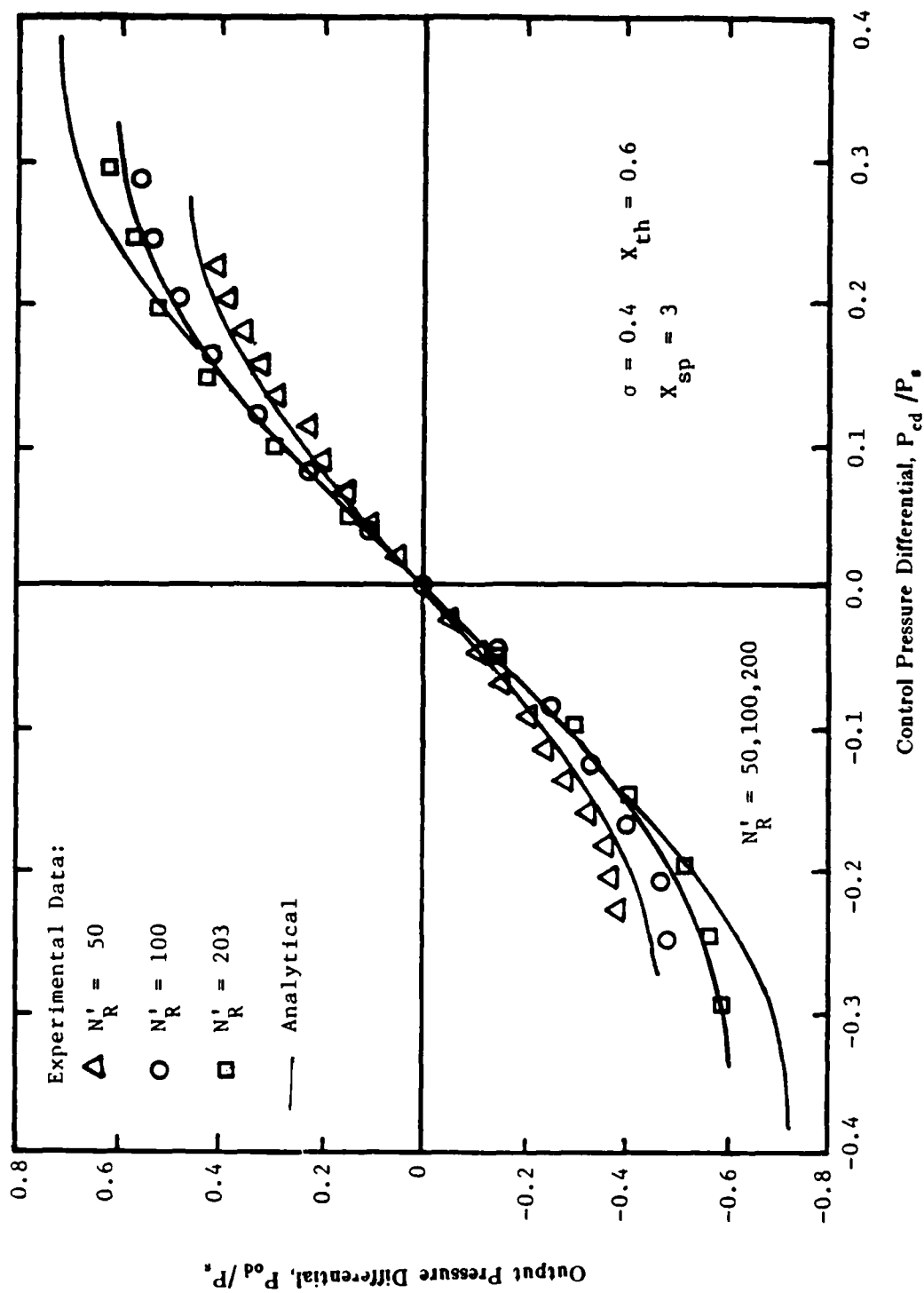


Figure 40. Blocked-load characteristics of power modulation LPA.

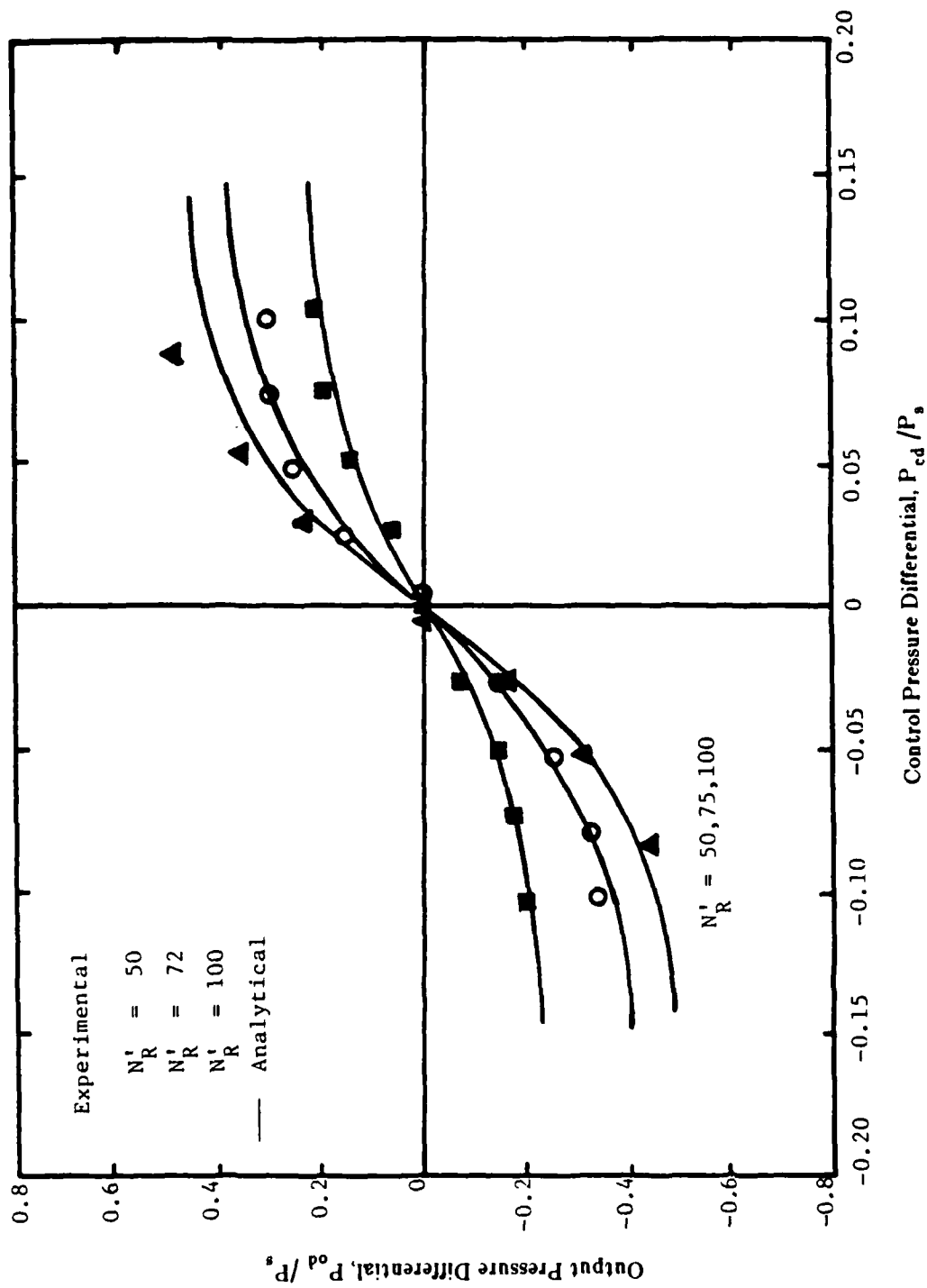


Figure 41. Blocked-load characteristics of traditional HDL design LPA.

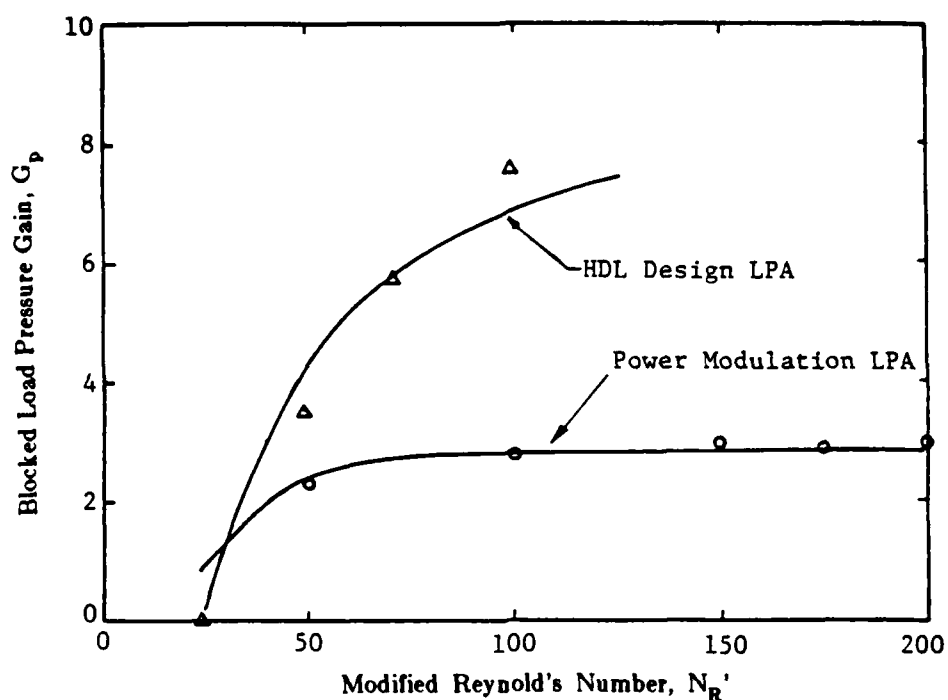


Figure 42. Comparison of blocked-load pressure gain.

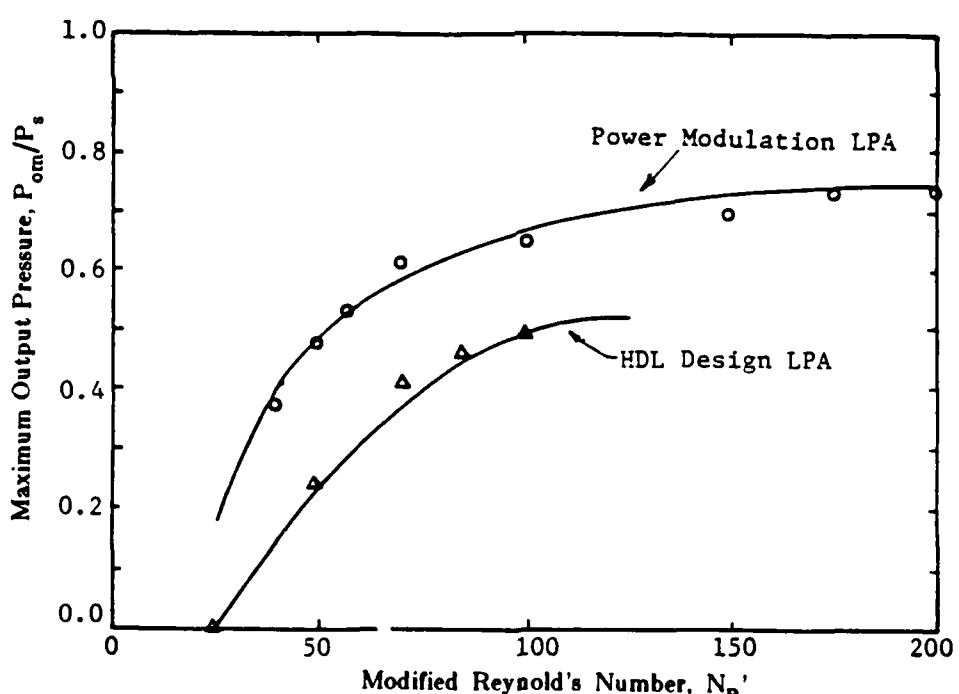


Figure 43. Comparison of blocked-load pressure recovery.

TABLE 3. OUTPUT RATING AND EFFICIENCY

$N'_R$	Power Modulation LPA			Standard HDL Design LPA		
	$\frac{P_{om}}{P_s}$	$\frac{Q_{om}}{Q_s}$	Max.Eff(%)	$\frac{P_{om}}{P_s}$	$\frac{Q_{om}}{Q_s}$	Max.Eff.(%)
25	0.176	0.12	0.5	Approaching Zero		
50	0.503	0.475	6.2	0.24	0.28	2.2
100	0.633	0.7	13.0	0.484	0.66	10.0
150	0.736	0.86	18.7	Turbulent Regime		
200	0.755	0.96	22.1			

power recovery can be significantly increased by operating the power modulation LPA at a higher  $N_R'$  than 120 as shown in figures 44 and 45 in which the experimental data for  $N_R'=175$  are compared with the analytical predictions.

#### 4.2.2 Temperature Sensitivity

The operating Reynold's numbers of fluidic amplifiers are often subjected to oil temperature variations through their influence on viscosity. For constant supply pressure and fluid density,

$$\frac{N_R}{N_{R,0}} = \frac{\nu_0}{\nu}, \quad (45)$$

where  $N_{R,0}$  and  $\nu_0$  are the Reynold's number and kinematic viscosity of the fluid at a specified design temperature. Based on the analytical model, the temperature sensitivities of the pressure gain of two LPA configurations are compared in figure 46. The pressure gain of the power modulation LPA is practically constant in the temperature range of 0 C to 70 C whereas that of the traditional LPA increases as the temperature increases. Beyond the temperature of 50 C, the traditional LPA operates in the turbulent regime where noise is a problem. The temperature sensitivities of the traditional LPA are primarily due to the change of fluid viscosity with temperature, which decreases from 40 cSt to 10 cSt corresponding to a temperature increase from 0 C to 70 C. Therefore, the Reynold's numbers change by a factor of 4 for the same temperature range. It has been noted that the blocked-load pressure recovery is more sensitive to the Reynold's number variation for large  $X_{sp}$  than small  $X_{sp}$  due to the influence of the top and bottom plates which increase the jet spread and reduce the jet momentum through frictional effects. The blocked-load pressure gain of the traditional LPA has the same temperature effect as the gain depends on the pressure recovery. By reducing the nozzle-to-splitter distance from 8 to 3 in the design of the power modulation LPA, the temperature sensitivities have been significantly reduced.

#### 4.2.3 Frequency Response

The dynamic response of the laminar fluidic amplifier has been studied by Caen et al<sup>13</sup> and Drzewiecki.<sup>14</sup> For low frequency application where the blocked-load pressure gain can be expressed as

$$G_p(s) = G_p e^{-\tau s}, \quad (46)$$

---

<sup>13</sup>R. Caen and C. Fonade, Analysis of the Frequency Response of a Fluid Amplifier Using Unsteady Flow Characteristics, *Journal of Fluids Engineering*, 105 (October 1980).

<sup>14</sup>T. M. Drzewiecki, A High Order, Lumped Parameter, Jet Dynamic Model for the Frequency Response of Laminar Proportional Amplifiers, *Trans. ASME, Journal of Dynamic Systems Measurement and Control*, 103 (December 1981).

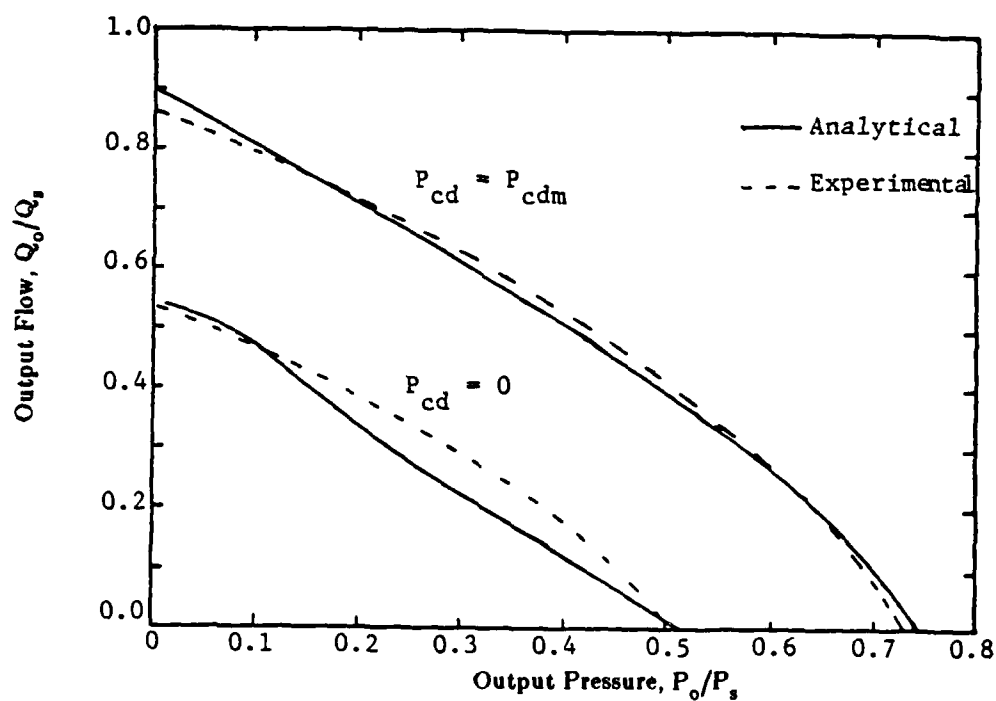


Figure 44. Comparison of output characteristics at  $N_R' = 175$ .

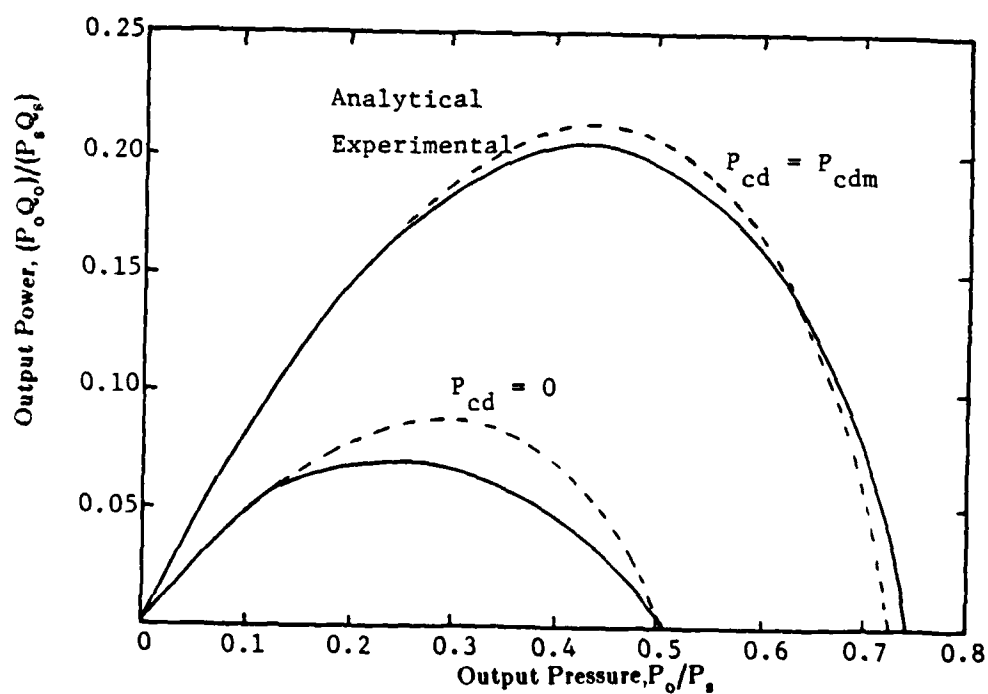


Figure 45. Efficiency of power modulation LPA at  $N_R' = 175$ .

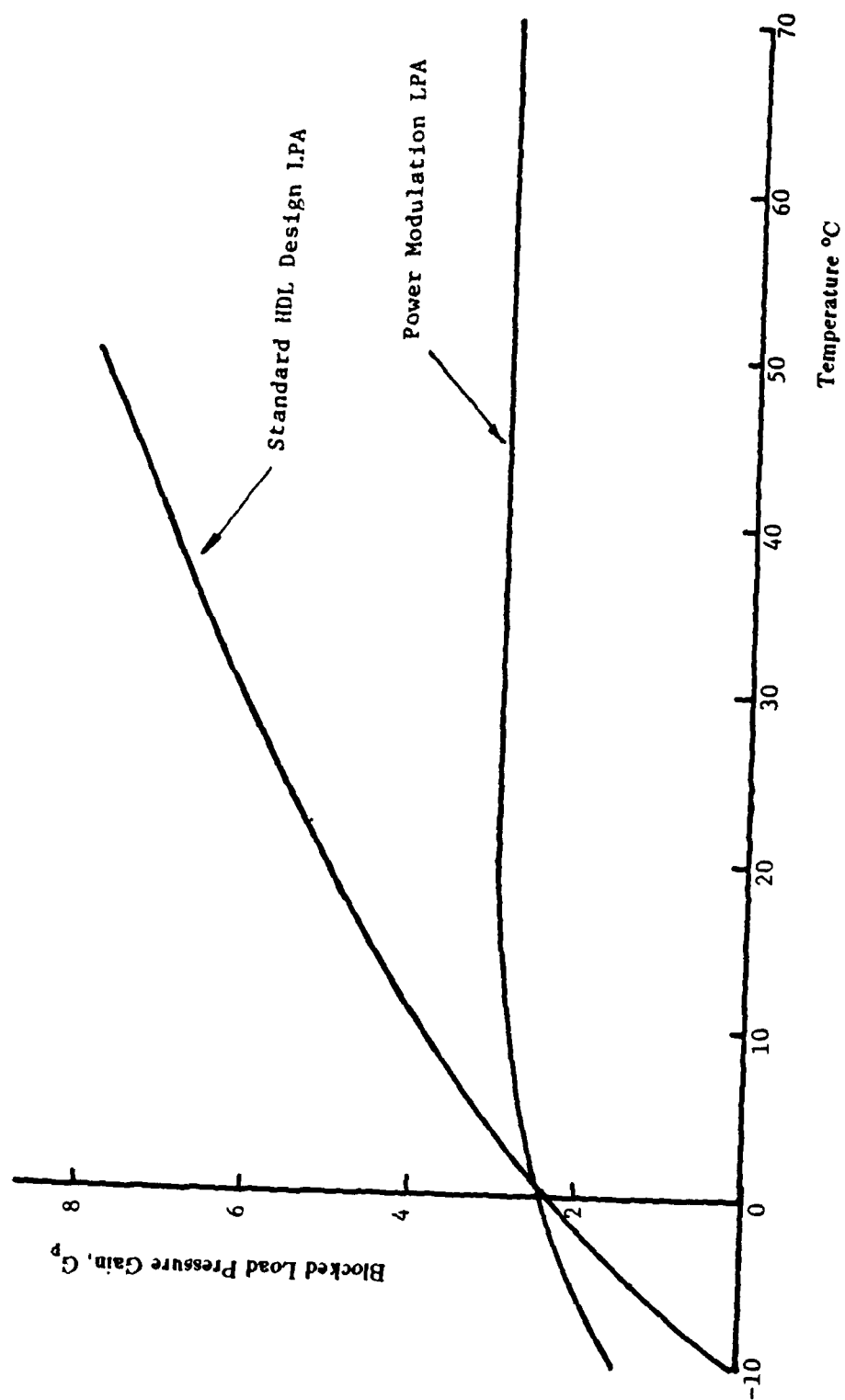


Figure 46. Effect of temperature.

$$\tau = 4 \frac{x_{sp}}{C_d u_s}, \quad (47)$$

where  $s$  is a Laplace operator and  $\tau$  is the time delay.

The time delay, in general, is proportional to the distance travelled,  $x_{sp}$ , and the average jet velocity. Hence,

$$\frac{\tau_I}{\tau_{II}} = \frac{x_{sp,I}}{x_{sp,II}} \frac{C_{d,II}}{C_{d,I}},$$

where subscripts "I" and "II" denote the parameters,  $x_{sp}$  and  $C_d$ , of the power modulation LPA and standard HDL design LPA respectively. For LPA's with a same  $b_s$ , the ratio of the time delay at the design temperature is

$$\frac{\tau_I}{\tau_{II}} = 0.365.$$

Hence, the bandwidth defined by 90 degree phase lag of the power modulation LPA should be increased compared to the standard HDL design LPA.

It is of interest to determine the steady-state blocked-load pressure gain and the time delay of the prototype LPA's frequency response. A prototype C-Format power modulation LPA has been machined out of 0.5 mm (0.02 in.) aluminium sheet using a 1/32-inch milling cutter. The nozzle throat width,  $b_s$ , and the aspect ratio of the prototype power modulation LPA are 0.78 mm (0.031 in.) and 0.667 respectively. The blocked-load pressure gain frequency response was obtained experimentally for both the prototype power modulation LPA and standard HDL design LPA 63020. The supply pressure and temperature were 689.5 KPa (100 psi) and 27 C respectively. The experimentally determined steady-state gain and frequency responses of the LPA's are compared in figure 47 and 48 respectively. The steady-state pressure gain of the power modulation LPA and standard HDL design LPA were determined experimentally to be 3 and 9 respectively. Due to the uneven machining process in manufacturing the prototype Power Modulation LPA, a significant offset occurs as shown in figure 47. However, it is worth noting that the bandwidth defined by the 90 degree phase lag has been extended from 300 to 800 Hz by reducing  $X_{sp}$  from 8 to 3.

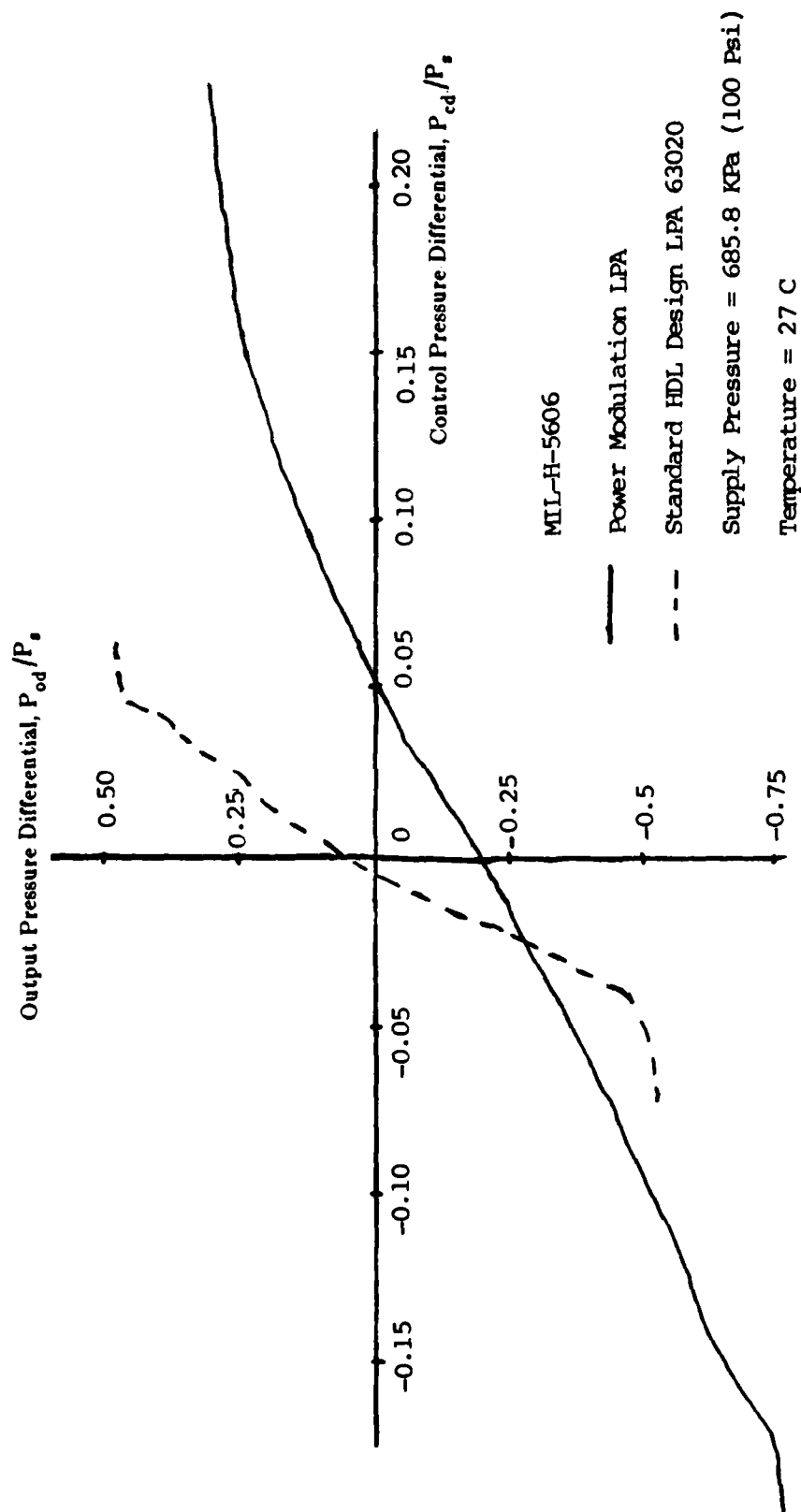


Figure 47. Steady-state gain of prototype LPA.

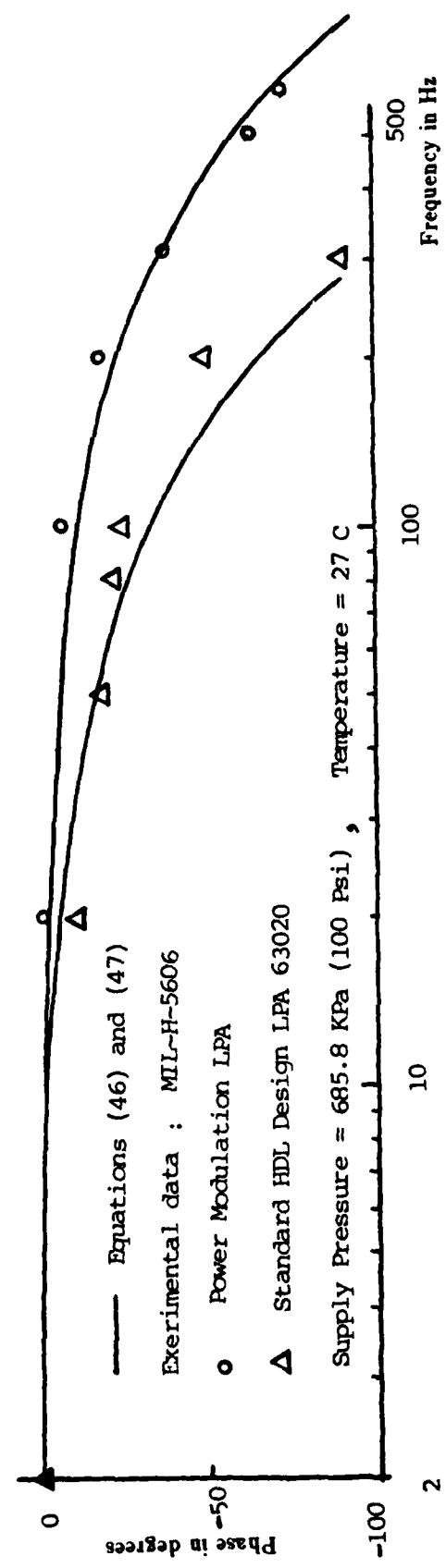
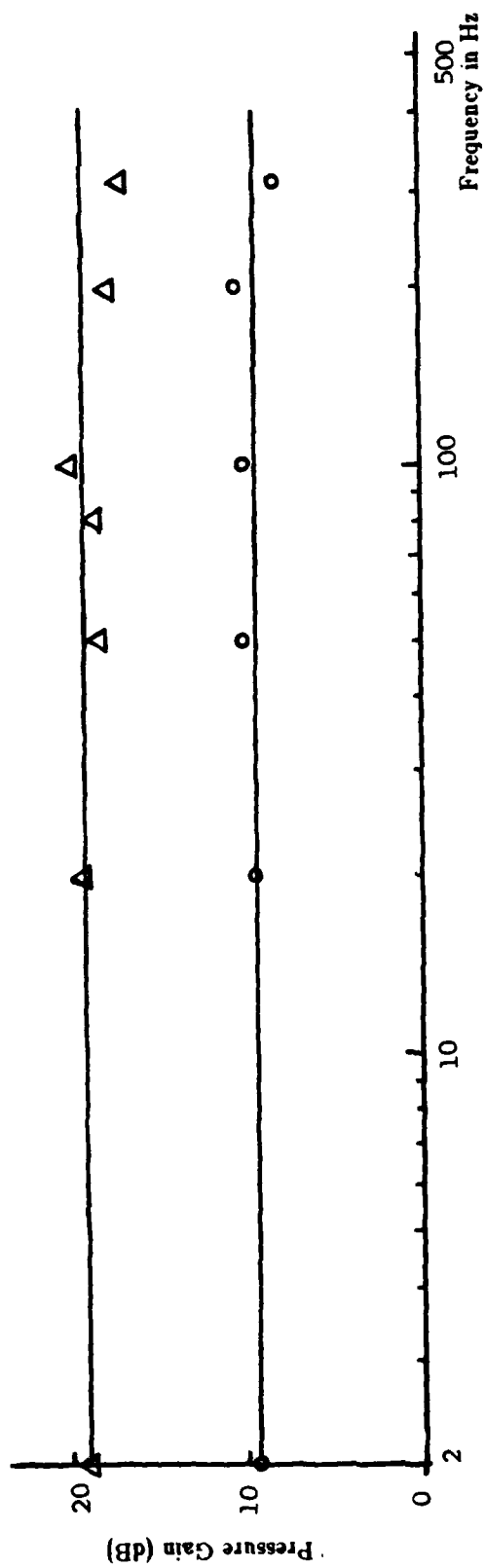


Figure 48. Comparison of frequency response.

#### 4.2.4 Leakage Flow

The leakage flow or quiescent flow is equal to the supply flow of the amplifier as the fluidic amplifier consumes power continuously regardless of the load condition. For each section, the maximum output flow obtainable from the power modulation LPA is 1.5 times that of the traditional LPA. To obtain the same rated maximum output flow, more sections of a traditional LPA with associated vent and exhaust laminates must be stacked in parallel. Thus, the leakage flow as well as the weight and volume of the traditional LPA are increased compared to the power modulation LPA for the same output power requirements.

#### 4.3 Discussion of Results

As shown in figures 40, 41, and 42, the analytical predictions are in close agreement with the experimental data in the linear range of the blocked-load characteristics and with the pressure gain which is defined as the slope of the blocked-load characteristics. In the saturation range of the blocked-load characteristics, the predictions are good for the maximum pressure recovery shown in figure 43, but overestimate the maximum control and output differential pressures shown in figure 40. The difference between the predictions and the experimental data is smaller for the LPA with  $X_{sp}=8$  than for LPA with  $X_{sp}=3$ . The differences may be due to the following approximations :

- An approximation has been made in simplifying the three-dimensional effects of the flow impingement on the splitter to a more tractable two-dimensional form.
- The non-uniformity of the velocity profile at the receiver inlet has been neglected. This approximation is good around the center-jet position. The velocity profile viewed by the receiving outlet channel may be well approximated to be uniform at a fully deflected jet position, but that seen by its adjacent outlet channel is non-uniform. The effect of non-uniformity is more pronounced for LPA with small  $X_{sp}$  than large  $X_{sp}$ .

The analytical predictions agree closely with both the center-jet and the fully deflected jet output characteristics. For the traditional LPA operated at  $N_R'=75$  which is somewhere in the middle of the operating range, the maximum pressure and flow recovery are 0.4 and 0.3 respectively and the maximum efficiency is less than 10 percent. However, for the power modulation LPA operated at  $N_R'=100$ , the maximum pressure and flow recovery are 0.65 and 0.75 respectively, considerably higher than the traditional LPA with the same supply pressure. The high-pressure recovery is due to the reduction of the nozzle-to-splitter distance; whereas, the high-flow recovery is a result of the efficient conversion of kinetic energy into controllable pressure in the diffuser-like receiver. The maximum output flow recovery and the efficiency of the power modulation LPA increases from 0.75 to 0.85 and from 15 percent to 22 percent respectively corresponding to the modified Reynold's number from 100 to 175. It is noted that the traditional LPA is operated in the turbulent flow regime beyond the modified Reynold's number of 120, where the analysis fails to apply.

## 5. SUMMARY AND CONCLUSION

A C-Format power modulation LPA has been developed, which is characterized by high-pressure/flow recovery and a temperature insensitive pressure gain. The high-pressure recovery and the temperature insensitivities are contributed by the small nozzle-to-splitter distance; whereas, the high-flow recovery is due to the efficient conversion of kinetic energy into controllable pressure by means of a diffuser-like receiver designed with a large radius of curvature.

An analytical model has been developed as a basis for design and characteristic performance predictions. For power modulation applications, effort concentrated on aspect ratios less than or equal to 0.8. The C-Format power modulation LPA has been optimized subjected to the constraints imposed by fluid properties and C-Format geometry. The studies show that the C-Format geometry has a significant influence on the LPA design in terms of the supply duct length and the receiver configurations, particularly for operation at high Reynold's number.

Both the power modulation LPA and the traditional LPA have been evaluated analytically and experimentally. The traditional LPA has a higher pressure gain than the power modulation LPA, but it is more temperature sensitive and has a smaller laminar operating range. Although the temperature sensitivities of the traditional LPA may be reduced by operation at  $N_R' > 40$  with an aspect ratio greater than unity, the requirement that the LPA must be operated in the laminar flow regime with a high supply pressure for the power modulation applications imposes an upper limit on the aspect ratio which is generally less than or equal to  $2/3$ . The maximum control differential pressure required to fully deflect the jet is 10 percent and 25 percent of the supply pressures for the traditional LPA and power modulation LPA respectively.

The pressure and flow recovery, as well as the efficiency of the power modulation LPA are substantially higher than those of the traditional LPA. In addition, as a result of the small  $X_{sp}$  in the power modulation LPA design, significant improvements in terms of temperature insensitivity and reduction of leakage flow, time delay, weight, and volume are achieved which are attractive to high-performance power modulation applications.

# APPENDIX A.--BOUNDED JET ANALYSIS

## A-1. INTRODUCTION

The following normalized equations are used in the bounded jet analysis; namely, the continuity, momentum and energy equations. The coordinate system is shown in section 2.3. The continuity equation in normalized form is

$$\frac{1}{2\sigma C_d N_R} \frac{\partial U}{\partial X^*} + \sigma \frac{\partial V}{\partial Y} + \frac{\partial W}{\partial Z} = 0, \quad (A-1)$$

where

$$X^* = \frac{X}{\sigma^2 C_d N_R}. \quad (A-2)$$

Similarly, the momentum equation is

$$\frac{1}{2\sigma C_d N_R} \frac{\partial}{\partial X^*} U^2 + \sigma \frac{\partial}{\partial Y} (UV) + \frac{\partial}{\partial Z} (UW) = \frac{2}{\sigma C_d N_R} \left( \sigma^2 \frac{\partial^2 U}{\partial Y^2} + \frac{\partial^2 U}{\partial Z^2} \right), \quad (A-3)$$

and the energy equation is :

$$\frac{1}{2\sigma C_d N_R} \frac{\partial}{\partial X^*} \left( \frac{1}{2} U^3 \right) + \sigma \frac{\partial}{\partial Y} \left( \frac{1}{2} U^2 V \right) + \frac{\partial}{\partial Z} \left( \frac{1}{2} U^2 W \right) = \frac{2}{\sigma C_d N_R} \left( \sigma^2 U \frac{\partial^2 U}{\partial Y^2} + U \frac{\partial^2 U}{\partial Z^2} \right). \quad (A-4)$$

Integrating the momentum and energy equations with respect to Y from zero to infinity and Z from zero to one with the use of the boundary conditions, the following integral equations are obtained

$$\frac{d}{dX^*} \int_{Z=0}^1 \int_{Y=0}^{\infty} U^2 dY dZ = 4 \int_{Y=0}^{\infty} \frac{\partial U}{\partial Z} \Big|_{Z=1} dY, \quad (A-5)$$

and

$$\frac{d}{dX^*} \int_{Z=0}^1 \int_{Y=0}^{\infty} \frac{1}{2} U^3 dY dZ = -4 \int_{Z=0}^1 \int_{Y=0}^{\infty} \left\{ \sigma^2 \left( \frac{\partial U}{\partial Y} \right)^2 + \left( \frac{\partial U}{\partial Z} \right)^2 \right\} dY dZ. \quad (A-6)$$

The flow development of the bounded jet is illustrated in figure A-1. It can be divided into three regions; namely, the developing region, the transition zone and the fully established jet. The definitions of these regions and the unknowns to be determined are summarized in table A-1. The velocity profiles of the bounded jet have been listed in table 1.

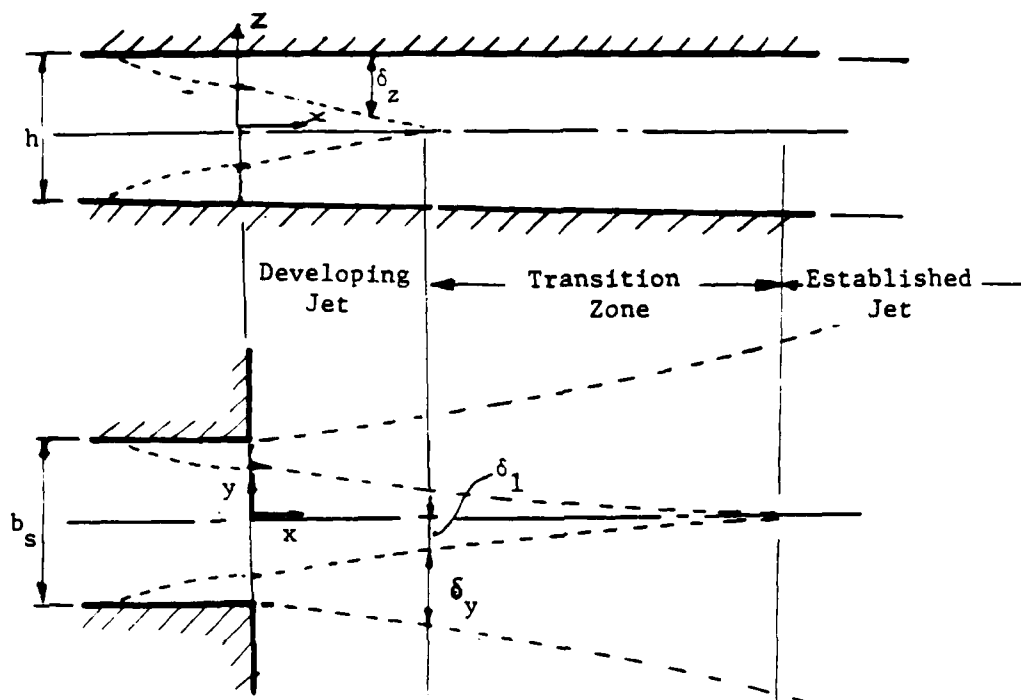


Figure A-1. Flow development of bounded jet.

TABLE A-1. FLOW DEVELOPMENT OF BOUNDED JET

	Definition	Unknown	Comments
Developing flow:	$m_z < 1$	$U_c = \text{constant}$	$\frac{dp}{dx} = 0$
	$\beta_1 > 0$	$m_z, \beta_1, m_y$	$\frac{dU_c}{dx} = 0$ (Bernoulli's Eqn.)
Transition zone:	Case 1: $\sigma^2 \ll 1$	$m_z = \text{constant}$	
	$m_z = 1$ $\beta_1 > 0$	$U_c, \beta_1, m_y$	
Fully established jet	Case 2: $\sigma^2 \geq 1$	$\beta_1 = \text{constant}$	
	$m_z < 1$ $\beta_1 = 0$	$U_c, m_z, m_y$	
Fully established jet	$m_z = 1$	$m_z = \text{constant}$	
	$\beta_1 = 0$	$\beta_1 = \text{constant}$ $U_c; m_y$	

## A-2. FULLY ESTABLISHED JET

When the jet is fully developed, the two unknowns are  $U_c$  which decays with increasing axial distance and  $m_y$  which increases due to the entrained flow and the continuity of the main flow.

Substituting the velocity profiles from table 1, the integral momentum and energy equations, (A-5) and (A-6) respectively, can be rewritten as

$$\frac{dU_c}{dX^*} = -\frac{6}{5} \pi^3 \left[ \left( \frac{\sigma}{m_y} \right)^2 + \frac{3}{4} \right] + \frac{16}{3} \pi, \quad (A-7)$$

$$\frac{dm_y}{dX^*} = \frac{m_y}{U_c} \left\{ \frac{12}{5} \pi^3 \left[ \left( \frac{\sigma}{m_y} \right)^2 + \frac{3}{4} \right] - 16\pi \right\}. \quad (A-8)$$

The equations can then be solved numerically for  $m_y$  and  $U_c$  using a fourth order Runge Kutta integration technique.

## A-3. DEVELOPING FLOW AND TRANSITION ZONE

For the case of developing jet flow and in the transition zone, there are three unknowns in each case as listed in table A-1. The additional equations can be obtained by integrating equations (A-1), (A-3) and (A-4) with respect to  $Y$  from 0 to  $\beta_1$  and  $Z$  from 0 to 1 as

$$\frac{\beta_1}{2\sigma C_d N_R} \frac{d}{dX^*} \int_{Z=0}^1 U dZ + \sigma \int_{Z=0}^1 V|_{\beta_1} dZ = 0, \quad (A-9)$$

$$\frac{\beta_1}{2\sigma C_d N_R} \frac{d}{dX^*} \int_{Z=0}^1 U^2 dZ + \sigma \int_{Z=0}^1 (UV)_{\beta_1} dZ = \frac{2}{\sigma C_d N_R} \int_{Y=0}^{\beta_1} \frac{\partial U}{\partial Z} \Big|_{Z=1} dY, \quad (A-10)$$

$$\frac{\beta_1}{2\sigma C_d N_R} \frac{d}{dX^*} \int_{Z=0}^1 \frac{1}{2} U^3 dZ + \sigma \int_{Z=0}^1 \left( \frac{1}{2} U^2 V \right)_{\beta_1} dZ = \frac{-2}{\sigma C_d N_R} \int_{Z=0}^1 \int_{Y=0}^{\beta_1} \left( \frac{\partial U}{\partial Z} \right)^2 dY dZ. \quad (A-11)$$

The form of the cross flow velocity  $V|_{\beta_1}$  is assumed to be :

$$V(X^*, \beta_1, Z) = V_1(X^*, \beta_1) F(X^*, Z). \quad (A-12)$$

Two additional unknowns,  $V_1$  and  $F$ , are introduced. Hence, five unknowns are to be solved from five equations, (A-5), (A-6), (A-9), (A-10), and (A-11).

### A-3.1 Developing Jet

The center line velocity,  $U_c$  is a constant. Hence, only the jet parameters,  $\beta_1$ ,  $m_z$  and  $m_y$  are of interest. Substituting the unknown integral of  $V_1$  from equation (A-9) into equations (A-10) and (A-11), the derivative  $dm_z/dX^*$  can then be eliminated by combining the resulting two equations as

$$\int_{1-m_z}^1 \frac{F}{1-m_z} \left[ \frac{1}{2} \left( \frac{U}{U_c} \right)^2 - \frac{\pi}{4} \left( \frac{U}{U_c} \right) - C_1 \right] dZ = C_1 + \frac{\pi}{4} - 1, \quad (A-13)$$

where  $C_1 = -0.28869$ .

Hence,  $F$  is assumed to have the form

$$F(m_z, \xi) = \frac{1-m_z}{m_z} \frac{a_0 + a_1 \xi + a_2 \xi^2 + a_3 \xi^3}{[(1/2)(U/U_c)^2 - (\pi/4)(U/U_c) - C_1]}, \quad (A-14)$$

where  $\xi$  and  $U/U_c$  are defined in table 1, in the main body of the report and the coefficients,  $a_0$ ,  $a_1$ ,  $a_2$ , and  $a_3$  are determined from the equation (A-13) and the following boundary conditions:

$$F(m_z, \xi=1) = 0,$$

$$\frac{\partial F}{\partial \xi}(m_z, \xi=0) = 0, \text{ and}$$

$$F(m_z, \xi=0) = 1.$$

Substituting the integral of  $V_1$  from equation (A-9) and  $F$  from equation (A-14) into equation (A-10),  $m_z$  can be solved as a function of  $X$  from equation (A-10). The remaining two unknowns are then solved from equations (A-5) and (A-6) with the assumed velocity profiles using Runge Kutta integration technique as in the case of fully established jet.

### A-3.2 Transition Zone

The procedure outlined in this section is similar to that for the developing jet. However,  $U_c$  which is no longer a known parameter must be determined in place of  $m_z$ . Again eliminating  $V_1$  from equations (A-10) and (A-11), the normalized axial distance  $X^*$  can then be eliminated from the resulting equations as

$$\int_{1-m_z}^1 F \left[ \frac{1}{2} \left( \frac{U}{U_c} \right)^2 - \frac{\pi}{4} \left( \frac{U}{U_c} \right) + C_2 \right] dZ = 0, \quad (A-15)$$

where

$$C_2 = \pi^2/8 - 1 .$$

F is assumed to be the form

$$F(Z) = \frac{1-m_z}{m_z} \frac{a_0 + a_1 Z + a_2 Z^2 + a_3 Z^3}{\{ (1/2)(U/U_c)^2 - (\pi/4)(U/U_c) + C_2 \}} , \quad (A-16)$$

and the coefficients,  $a_0$ ,  $a_1$ ,  $a_2$  and  $a_3$  are determined from the equation (A-15) and the boundary conditions

$$F(Z=1) = 0 .$$

$$\frac{\partial F}{\partial Z}(Z=0) = 0 , \text{ and}$$

$$F(Z=0) = 1 .$$

Substituting the integral of  $V_1$  from equation (A-9) and F from equation (A-16) into equation (A-10),  $U_c$  can be solved as a function of X from equation (A-10). The remaining two unknowns are then solved from equations (A-5) and (A-6) with the assumed velocity profiles using a Runge Kutta integration technique as in the case of fully-established jet.

# APPENDIX B.--NORMALIZED CHANNEL RESISTANCE

## B-1. INTRODUCTION

As the pressure and flow are normalized to the supply pressure and the flow through the supply nozzle respectively, the flow resistance of the channel is normalized to the supply resistance. In the following section, the supply resistance is defined and the coefficients of the normalized channel resistance are expressed in terms of the fluid properties and the nozzle geometries.

## B-2. NORMALIZED CHANNEL RESISTANCE

The supply resistance of a LPA is defined as

$$R_s = \frac{P_s}{Q_s} = \frac{\mu N_R}{2(C_d b_s^3 \sigma)}, \quad (B-1)$$

where  $\mu$  = fluid absolute viscosity, and defining a flow resistance as

$$R = \frac{P_i - P_o}{Q}, \quad (B-2)$$

where

$P_i$  = pressure at channel inlet,

$P_o$  = pressure at channel outlet, and

$Q$  = flow through channel.

The normalized channel resistance,  $R_c/R_s$ , can be written as

$$\frac{R_c}{R_s} = \frac{R_l}{R_s} + K_c \frac{Q}{Q_s}, \quad (B-3)$$

where

$$\frac{R_l}{R_s} = \frac{1}{4} (f \cdot Re) \left( 1 + \frac{\sigma}{B_c} \right)^2 \frac{C_d}{N_R} \frac{X_c}{B_c \sigma^2}, \quad (B-4)$$

and

$$K_c = \frac{C_d^2}{B_c^2} K_{fd}. \quad (B-5)$$

$B_c$  and  $X_c$  are the width and length of the rectangular channel normalized to  $b_s$  respectively.

# NOMENCLATURE

## Capitalized Letter

$A_o$	area of receiver inlet
$B_c$	downstream control port width to nozzle throat width ratio
$B_{c1}$	defined in figure 29
$B_j$	defined in equation (17)
$B_o$	receiver inlet width to nozzle throat width ratio
$B_{om}$	defined in figure 29 normalized to $b_s$
$B_{s1}$	supply duct width to nozzle throat width ratio
$B_t$	downstream control edges spacing to nozzle throat width ratio
$C_d$	discharge coefficient
$C_{sp}$	splitter friction coefficient
$D_c$	normalized deflection at $X=B_c$
$D_e$	equivalent diameter, $4A/p$
$D_o$	normalized deflection at $X=X_{sp}$
$F$	function defined in equation (A-12)
$G_p$	pressure gain
$J_s$	normalized momentum flux at nozzle exit
$K_{fd}$	fully developed correction factor
$K_j$	defined in equation (22)
$N_R$	Reynold's number
$N_{R,0}$	$N_R$ at design temperature
$N_R'$	modified Reynold's number
$P_c$	control port pressure
$P_i$	pressure at channel inlet
$P_j$	jet edge pressure

$P_m$	peak pressure
$P_{max}$	maximum pressure recovery
$P_o$	pressure at receiver outlet
$P_r$	average pressure at receiver inlet
$P_s$	supply pressure
$P_v$	vent pressure
$Q_c$	control flow
$Q_e$	entrained flow
$Q_o$	outlet flow
$Q_r$	return flow
$Q_s$	supply flow
$Q_v$	vent flow
$R_c$	control port channel resistance
$Re$	Reynold's number based on equivalent diameter
$U$	dimensionless axial velocity
$U_c$	normalized centerline velocity
$U_{sp}$	defined in equation (41)
$V$	dimensionless Y-component velocity
$V_I$	defined in equation (A-12)
$W$	dimensionless Z-component velocity
$X$	normalized axial distance
$X_j$	X measured to the inlet of jet/receiver interaction region
$X_{cv}$	defined in figure 29, normalized to $b_s$
$X_{eq}$	equivalent length to nozzle throat width ratio
$X_o$	receiver channel length to nozzle throat width ratio
$X_{sp}$	nozzle/splitter distance to nozzle throat width ratio
$X_{sl}$	supply duct length to nozzle throat width ratio

$X_{th}$  nozzle throat length-to-width ratio

$X^*$  defined in equation (A-2)

$Y$  normalized y-coordinate

$Z$  normalized z-coordinate

#### Lower Case Letter

$a_o$  coefficient in equation (A-14) or (A-16)

$a_1$  coefficient defined in equation (A-14) or (A-16)

$a_2$  coefficient defined in equation (A-14) or (A-16)

$a_3$  coefficient defined in equation (A-14) or (A-16)

$b_s$  supply nozzle throat width

$f$  friction factor

$h$  depth

$m_z$  jet parameter defined in equation (13)

$m_y$  jet parameter defined in equation (15)

$r$  radius of jet curvature

$s$  elemental length in section 2.4 or Laplace operator in section 4.2.3

$u$  axial velocity

$u_c$  centerline velocity

$u_s$  Bernoulli's velocity

$\bar{u}$  average velocity

$v$  y component velocity

$w$  z component velocity

$x$  axial distance defined in figure 14

$x'$   $x - x_{sp}$

$y$  defined in figure 14

$z$  defined in figure 14

### Capitalized Greek Letter

- $\Phi$  normalized entrance length  
 $\Phi_o$  normalized entrance length of receiver

### Lower Case Greek Letter

- $\alpha_D$  defined in equation (37)  
 $\alpha_j$  momentum flux at  $X=X_j$   
 $\beta$  parameter in pressure profile representation  
 $\beta_1$  jet parameter defined in equation (14)  
 $\beta_2$  jet parameter defined in equation (16)  
 $\delta$  deflection  
 $\delta_c$  jet deflection at  $X=B_c$   
 $\delta_y$  defined in figure A-1  
 $\delta_z$  defined in figure A-1  
 $\delta_1$  defined in figure A-1  
 $\phi_o$  included angle of divergence  
 $\phi$  angle of spill back flow at receiver inlet  
 $\eta$  defined in table 1  
 $\mu$  viscosity of fluid  
 $\nu$  kinematic viscosity of fluid  
 $\nu_0$   $\nu$  at design temperature  
 $\rho$  density of fluid  
 $\sigma$  aspect ratio  
 $\tau_I$  time delay of power modulation LPA  
 $\tau_{II}$  time delay of standard HDL design LPA  
 $\xi$  defined in table 1

## DISTRIBUTION

ADMINISTRATOR  
DEFENSE TECHNICAL INFORMATION CENTER  
ATTN DTIC-DDA (12 COPIES)  
CAMERON STATION, BUILDING 5  
ALEXANDRIA, VA 22304-6145

OFFICE OF THE DEPUTY CHIEF OF STAFF FOR  
RESEARCH, DEVELOPMENT, & ACQUISITION  
DEPARTMENT OF THE ARMY  
ATTN DAMA-ARP-P  
ATTN DAMA-CSS-N  
WASHINGTON, DC 20310

COMMANDER IDDR&E  
PENTAGON, ROOM 3D 1089  
ATTN G. KOPCSAK  
WASHINGTON, DC 20310

DIRECTOR  
APPLIED TECHNOLOGY LABORATORY  
ATTN DAVDL-ATL-ASA  
FT EUSTIS, VA 23604

COMMANDER  
US ARMY ARMAMENT, MUNITIONS, &  
CHEMICAL COMMAND  
ATTN SARPA-TS-S #59  
ATTN DRDAR-LCN-C, A. E. SCHMIDLIN  
ATTN DRDAR-LCW-E, J. CONNORS  
ATTN DRDAR-SCF-IC, V. BAUMGARTH  
ATTN PBM-DPM (TAGLAIRINO)  
DOVER, NJ 07801

COMMANDER  
US ARMY ARMAMENT, MUNITIONS, &  
CHEMICAL COMMAND  
ATTN DRSAR-ASF, FUZE &  
MUNITIONS SUPPORT DIV  
ATTN DRSAR-RDF, SYS DEV DIV-FUZES  
ATTN DRSAR-RDG-T, R. SPENCER  
ATTN DRSAR-ASF  
ATTN DRSAR-LEP-L, TECH LIBRARY  
ROCK ISLAND, IL 61299

COMMANDER  
US ARMY ARMAMENT, MUNITIONS, &  
CHEMICAL COMMAND  
WATERVLIET ARSENAL  
ATTN SARWV-RDT-L  
ATTN DRDAR-LCB-RA, R. RACICOT  
WATERVLIET ARSENAL, NY 12189

BMD ADVANCED TECHNOLOGY CENTER  
PO BOX 1500  
ATTN J. PAPADOPOULOS  
HUNTSVILLE, AL 35807

DIRECTOR  
US ARMY BALLISTIC RESEARCH LABORATORY  
ATTN DRDAR-TSB-S (STINFO)  
ABERDEEN PROVING GROUND, MD 21005

US ARMY ELECTRONICS TECHNOLOGY  
& DEVICES LABORATORY  
ATTN DELET-DD  
FT MONMOUTH, NJ 07703

COMMANDER/DIRECTOR  
ATMOSPHERIC SCIENCES LABORATORY  
ATTN DELAS-AS (HOLT)  
ATTN DELAS-AS-T (R. RUBIO)  
WHITE SANDS MISSILE RANGE, NM 88002

COMMANDER  
US ARMY FOREIGN SCIENCE  
& TECHNOLOGY CENTER  
FEDERAL OFFICE BUILDING  
ATTN DRXST-SD1  
ATTN DRXST-IS3, C. R. MOORE  
220 7TH STREET, NE  
CHARLOTTESVILLE, VA 22901

COMMANDER  
US ARMY MATERIEL COMMAND  
ATTN AMCLD, JAMES BENDER  
5001 EISENHOWER AVENUE  
ALEXANDRIA, VA 22333-0001

DIRECTOR  
US ARMY MATERIEL SYSTEMS  
ANALYSIS ACTIVITY  
ATTN DRXSY-MP  
ABERDEEN PROVING GROUND, MD 21005

COMMANDER  
US ARMY MATERIEL & MECHANICS  
RESEARCH CENTER  
ATTN R. KATZ  
WATERTOWN, MA 02172

COMMANDER  
US ARMY MISSILE COMMAND  
ATTN REDSTONE SCIENTIFIC INFORMATION  
CENTER, DRSMI-RBD  
ATTN DRSMI-RC, WILLIAM GRIFFITH  
ATTN DRSMI-TGC, J. C. DUNAWAY  
ATTN DRCPM-TOE, FRED J. CHEPLEN  
REDSTONE ARSENAL, AL 35898

COMMANDER  
US ARMY MISSILE & MUNITIONS  
CENTER & SCHOOL  
ATTN ATSK-CTD-F  
REDSTONE ARSENAL, AL 35809

COMMANDER  
US ARMY MOBILITY EQUIPMENT R&D CENTER  
ATTN TECHNICAL LIBRARY (VAULT)  
ATTN DRDME-EM, R. N. WARE  
FT BELVOIR, VA 22060

US ARMY R&D GROUP (EUROPE)  
BOX 15  
ATTN CHIEF, AERONAUTICS BRANCH  
ATTN CHIEF, ENGINEERING SCIENCES  
FPO NEW YORK 09510

US ARMY RESEARCH OFFICE  
PO BOX 12211  
ATTN R. SINGLETON  
RESEARCH TRIANGLE PARK, NC 27709

COMMANDER  
US ARMY RSCH & STD GP (EUR)  
ATTN CHIEF, PHYSICS & MATH BRANCH  
FPO NEW YORK 09510

COMMANDER  
US ARMY-TANK AUTOMOTIVE COMMAND  
ARMOR & COMP DIV, DRDTA-RKT  
BLDG 215  
ATTN M. WHITMORE  
WARREN, MI 48090

COMMANDER  
ATTN STEWS-AD-L, TECHNICAL LIBRARY  
WHITE SANDS MISSILE RANGE, NM 88002

OFFICE OF NAVAL RESEARCH  
DEPARTMENT OF THE NAVY  
ATTN STANLEY W. DOROFF, CODE 438  
ATTN D. S. SIEGEL, CODE 211  
ARLINGTON, VA 22217

DEPARTMENT OF THE NAVY  
R&D PLANS DIVISION  
ROOM 5D760, PENTAGON  
ATTN BENJ R. PETRIE, JR.  
OP-987P4  
WASHINGTON, DC 20350

COMMANDER  
NAVAL AIR DEVELOPMENT CENTER  
ATTN R. MCGIBONEY, 60134  
ATTN CODE 8134, LOIS GUISE  
ATTN D. KEYSER, 60134  
WARMINSTER, PA 18974

COMMANDING OFFICER  
NAVAL AIR ENGINEERING CENTER  
ATTN ESSD, CODE 9314, HAROLD OTT  
LAKEHURST, NY 08733

NAVAL AIR SYSTEMS COMMAND  
DEPARTMENT OF THE NAVY  
ATTN CODE AIR-5162C1, J. BURNS  
ATTN CODE AIR-5143, D. RETTA  
WASHINGTON, DC 20361

COMMANDER  
PACIFIC MISSILE TEST CENTER  
ATTN CODE 3123, ABE J. GARRETT  
ATTN CODE 1243, A. ANDERSON  
POINT MUGU, CA 93042

COMMANDER  
NAVAL ORDNANCE STATION  
ATTN CODE 5123C, K. ENGLANDER  
INDIAN HEAD, MD 20640

COMMANDANT  
US NAVAL POSTGRADUATE SCHOOL DEPARTMENT  
OF MECHANICAL ENGINEERING  
ATTN CODE 69 Nn(NUNN)  
MONTEREY, CA 93940

NAVAL RESEARCH LABORATORY  
ATTN S. SEARLES, 117 BG A68  
WASHINGTON, DC 20375

NAVAL SEA SYSTEMS COMMAND  
SEA05R31  
ATTN J. H. HARRISON  
WASHINGTON, DC 20362

COMMANDER  
NAVAL SHIP ENGINEERING CENTER  
PHILADELPHIA DIVISION  
ATTN CODE 6772  
PHILADELPHIA, PA 19112

NAVAL SHIP RES & DEV CENTER  
ATTN CODE 1619, K. READER  
BETHESDA, MD 20084

COMMANDER  
NAVAL SURFACE WEAPONS CENTER  
ATTN CODE 413, CLAYTON MCKINDRA  
WHITE OAK, MD 20910

COMMANDER  
NAVAL WEAPONS CENTER  
ATTN CODE 533, LIBRARY DIVISION  
ATTN CODE 3636, C. BURMEISTER  
CHINA LAKE, CA 93555

USHQ, AF SYSTEMS COMMAND  
ATTN SGB, MAJ GEORGE JAMES  
ANDREWS AFB, DC 20334

HQ, USAF/SAMI  
WASHINGTON, DC 20330

COMMANDER  
AF AERO PROPULSION LABORATORY, AFSC  
ATTN LESTER SMALL, AFWAL/POTC  
WRIGHT-PATTERSON AFB, OH 45433

COMMANDER  
ARMAMENT DEVELOPMENT & TEST CENTER  
ATTN ADTC (DLOSL), TECH LIBRARY  
EGLIN AIR FORCE BASE, FL 32542

COMMANDER  
AIR FORCE AVIONICS LABORATORY  
ATTN AARA-2, RICHARD JACOBS  
WRIGHT-PATTERSON AFB, OH 45433

COMMANDER  
AIR FORCE FLIGHT DYNAMICS LABORATORY  
ATTN AFWAL/FIGL, H. SNOWBALL  
ATTN AFWAL/PIER, R. J. DOBBEK  
WRIGHT-PATTERSON AFB, OH 45433

AIR FORCE FLIGHT TEST CENTER  
6510 ABG/SSD  
ATTN TECHNICAL LIBRARY  
EDWARDS AFB, CA 93523

AF INSTITUTE OF TECHNOLOGY, AU  
ATTN LIBRARY AFIT (LD),  
BLDG 640, AREA B  
ATTN AFIT (ENM), MILTON E. FRANKE  
WRIGHT-PATTERSON AFB, OH 45433

DIRECTOR  
AF OFFICE OF SCIENTIFIC RESEARCH  
ATTN NE  
BOLLING AFB, DC 20332

COMMANDER  
AF WEAPONS LABORATORY, AFSC  
ATTN SUL, TECHNICAL LIBRARY  
KIRTLAND AFB, NM 87117

ARGONNE NATIONAL LABORATORY  
APPLIED PHYSICS DIV, BLDG 316  
ATTN N. M. O'FALLAN  
9700 S. CASS AVE  
ARGONNE, IL 60439

DEPARTMENT OF COMMERCE  
NATIONAL BUREAU OF STANDARDS  
ATTN JAMES SCHOOLEY, CHIEF,  
TEMPERATURE SECTION  
ATTN T. NEGAS, SOLID STATE  
CHEMISTRY DIVISION  
ATTN RAY DILS, RM B-254, BLDG 221  
ATTN GEORGE BURNS, RM B-222, BLDG 221  
WASHINGTON, DC 20230

DEPARTMENT OF COMMERCE  
BUREAU OF EAST-WEST TRADE  
OFFICE OF EXPORT ADMINISTRATION  
ATTN WALTER J. RUSNACK  
WASHINGTON, DC 20230

DEPARTMENT OF ENERGY  
C-156, GTN (OART)  
ATTN ROBERT ROBERTS  
ATTN SANDY DAPKUNAS  
WASHINGTON, DC 20585

DEPARTMENT  
FE-22  
ATTN T. K. LAU  
WASHINGTON, DC 20585

DEPARTMENT OF ENERGY  
F-317, GTN (COAL GASIFICATION)  
ATTN JIM CARR  
WASHINGTON, DC 20585

FEDERAL BUREAU OF INVESTIGATION  
J. EDGAR HOOVER BLDG  
ATTN ROBERT WILLIS  
WASHINGTON, DC 20535

JET PROPULSION LABORATORY  
ATTN JOHN V. WALSH, MS 125-138  
4800 OAK GROVE DRIVE  
PASADENA, CA 91103

DEPARTMENT OF JUSTICE  
IMMIGRATION & NATURALIZATION SERVICE  
425 "I" STREET, NW  
ATTN NEILL MCKAY  
WASHINGTON, DC 20536

LOS ALAMOS SCIENTIFIC LAB  
PO BOX 1663  
ATTN FRANK FINCH, MS 178  
LOS ALAMOS, NM 87545

NASA LANGLEY RESEARCH CENTER  
ATTN MS 494, H. D. GARNER  
ATTN MS 494, R. R. HELLBAUM  
ATTN MS 185, TECHNICAL LIBRARY  
HAMPTON, VA 23665

NASA SCIENTIFIC & TECH INFO FACILITY  
PO BOX 8657  
ATTN ACQUISITIONS BRANCH  
BALTIMORE/WASHINGTON INTERNATIONAL  
AIRPORT, MD 21240

OAK RIDGE NATIONAL LABORATORY  
CENTRAL RES LIBRARY, BLDG. 4500N,  
RM 175  
PO BOX X  
ATTN E. HOWARD

OAK RIDGE NATIONAL LABORATORY (cont'd)  
ATTN C. A. MOSSMAN  
ATTN R. E. HARPER  
OAK RIDGE, TN 37830

SCIENTIFIC LIBRARY  
US PATENT OFFICE  
ATTN MRS. CURETON  
WASHINGTON, DC 20231

UNIVERSITY OF ALABAMA  
CIVIL & MINERAL ENGINEERING DEPT  
PO BOX 1468  
ATTN HAROLD R. HENRY  
UNIVERSITY, AL 35486

UNIVERSITY OF ARKANSAS  
TECHNOLOGY CAMPUS  
PO BOX 3017  
ATTN PAUL C. MCLEOD  
LITTLE ROCK, AR 72203

UNIVERSITY OF ARKANSAS  
MECHANICAL ENGINEERING  
ATTN JACK H. COLE, ASSOC. PROF.  
FAYETTEVILLE, AR 72701

CARNEGIE-MELLON UNIVERSITY  
SCHENLEY PARK  
ATTN PROF. W. T. ROULEAU,  
MECH ENGR DEPT  
PITTSBURGH, PA 15213

CASE WESTERN RESERVE UNIVERSITY  
ATTN PROF. P.A. ORNER  
ATTN PROF. B. HORTON  
UNIVERSITY CIRCLE  
CLEVELAND, OH 44106

THE CITY COLLEGE OF THE CITY  
UNIVERSITY OF NY  
DEPT OF MECH ENGR  
ATTN PROF. L. JIJI  
ATTN PROF. G. LOWEN  
139TH ST. AT CONVENT AVE  
NEW YORK, NY 10031

CLEVELAND STATE UNIVERSITY  
FENN COLLEGE OF ENGINEERING  
ATTN PROF. R. COMPARIN  
CLEVELAND, OH 44115

DUKE UNIVERSITY  
COLLEGE OF ENGINEERING  
ATTN C. M. HARMAN  
DURHAM, NC 27706

FRANKLIN INSTITUTE OF THE STATE  
OF PENNSYLVANIA  
ATTN KA-CHEUNG TSUI, ELEC ENGR DIV  
ATTN C. A. BELSTERLING  
20TH STREET PARKWAY  
PHILADELPHIA, PA 19103

IIT RESEARCH INSTITUTE  
ATTN K. E. MCKEE  
10 WEST 35TH STREET  
CHICAGO, IL 60616

JOHNS HOPKINS UNIVERSITY  
APPLIED PHYSICS LABORATORIES  
ATTN MAYNARD HILL  
ATTN THOMAS RANKIN  
ATTN JOSEPH WALL  
LAUREL, MD 20810

LEHIGH UNIVERSITY  
DEPARTMENT OF MECHANICAL ENGINEERING  
ATTN PROF. FORBES T. BROWN  
BETHLEHEM, PA 18015

LINDA HALL LIBRARY  
ATTN DOCUMENTS DIVISION  
5109 CHERRY STREET  
KANSAS CITY, MO 64110

MASSACHUSETTS INSTITUTE OF TECHNOLOGY  
ATTN ENGINEERING TECHNICAL REPORTS,  
RM 10-408  
ATTN DAVID WORMLEY, MECH ENGR DEPT,  
RM 3-146  
77 MASSACHUSETTS AVENUE  
CAMBRIDGE, MA 02139

MIAMI UNIVERSITY  
DEPT OF ENG TECH  
SCHOOL OF APPLIED SCIENCE  
ATTN PROF. S. B. FRIEDMAN  
OXFORD, OH 45056

MICHIGAN TECHNOLOGICAL UNIVERSITY  
LIBRARY, DOCUMENTS DIVISION  
ATTN J. HAWTHORNE  
HOUGHTON, MI 49931

UNIVERSITY OF MISSISSIPPI  
ATTN JOHN A. FOX  
201 CARRIER HALL, DEPT OF MECH ENGR  
UNIVERSITY, MS 38677

MISSISSIPPI STATE UNIVERSITY  
DRAWER ME  
ATTN C. J. BELL, MECH ENG DEPT  
STATE COLLEGE, MS 39762

MISSISSIPPI STATE UNIVERSITY  
DEPT OF AEROSPACE ENGINEERING  
ATTN DAVID MURPHREE  
MISSISSIPPI STATE, MS 39762

UNIVERSITY OF NEBRASKA LIBRARIES  
ACQUISITIONS DEPT, SERIALS SECTIONS  
ATTN ALAN GOULD  
LINCOLN, NE 68508

UNIVERSITY OF NEW HAMPSHIRE  
MECH ENGR. DEPT, KINGSBURY HALL  
ATTN PROF. CHARLES TAFT  
ATTN PROF. DAVID LIMBERT  
DURHAM, NH 03824

UNIVERSITY OF N. CAROLINA  
INSTITUTE OF MARINE BIOMEDICAL RESEARCH  
ATTN MICHAEL E. SHEEHAN  
WILMINGTON, NC 28401

NEW JERSEY INSTITUTE OF TECHNOLOGY  
DEPARTMENT OF MECHANICAL ENGINEERING  
ATTN R. Y. CHEN  
323 HIGH STREET  
NEWARK, NJ 07102

OHIO STATE UNIVERSITY LIBRARIES  
SERIAL DIVISION, MAIN LIBRARY  
1858 NEIL AVENUE  
COLUMBUS, OH 43210

OKLAHOMA STATE UNIVERSITY  
SCHOOL OF MECH & AEROSPACE ENGR  
ATTN PROF. KARL N. REID  
STILLWATER, OK 74074

PENNSYLVANIA STATE UNIVERSITY  
ATTN J. L. SHEARER  
215 MECHANICAL ENGINEERING BUILDING  
UNIVERSITY PARK, PA 16802

PENNSYLVANIA STATE UNIVERSITY  
ENGINEERING LIBRARY  
ATTN M. BENNETT, ENGINEERING LIBRARIAN  
201 HAMMOND BLDG  
UNIVERSITY PARK, PA 16802

PORTLAND STATE UNIVERSITY  
DEPT OF ENGINEERING &  
APPLIED SCIENCE  
PO BOX 751  
ATTN PROF. P. I. CHEN  
PORTLAND, OR 97207

PURDUE UNIVERSITY  
SCHOOL OF MECHANICAL ENGINEERING  
ATTN PROF. VICTOR W. GOLDSCHMIDT  
ATTN PROF. ALAN T. McDONALD  
LAFAYETTE, IN 47907

ROCK VALLEY COLLEGE  
ATTN KEN BARTON  
3301 N. MULFORD ROAD  
ROCKFORD, IL 61101

RUTGERS UNIVERSITY  
LIBRARY OF SCIENCE & MEDICINE  
ATTN GOVERNMENT DOCUMENTS DEPT  
SANDRA R. LIVINGSTON  
NEW BRUNSWICK, NJ 08903

SYRACUSE UNIVERSITY  
DEPT OF MECH & AEROSPACE ENGINEERING  
ATTN PROF. D. S. DOSANJH  
139 E. A. LINK HALL  
SYRACUSE, NY 13210

UNIVERSITY OF TENNESSEE  
DEPT OF MECHANICAL ENGINEERING  
ATTN PROF. G. V. SMITH  
KNOXVILLE, TN 37916

UNIVERSITY OF TENNESSEE SPACE INST  
ENERGY CONVERSION DIVISION  
ATTN MARY ANN SCOTT  
TULLAHOMA, TN 37388

UNIVERSITY OF TEXAS AT AUSTIN  
DEPT OF MECHANICAL ENGINEERING  
ATTN A. J. HEALEY  
AUSTIN, TX 78712

THE UNIVERSITY OF TEXAS AT ARLINGTON  
MECHANICAL ENGINEERING DEPARTMENT  
ATTN ROBERT L. WOODS  
ARLINGTON, TX 76019

TULANE UNIVERSITY  
DEPT OF MECHANICAL ENGINEERING  
ATTN H. F. HRUBECKY  
NEW ORLEANS, LA 70118

UNION COLLEGE  
MECHANICAL ENGINEERING  
ATTN ASSOC. PROF. W. C. AUBREY  
MECH ENGR DEPT, STEINMETZ HALL  
SCHENECTADY, NY 12308

UNIVERSITY OF VIRGINIA  
DEPT OF MECH & AEROSPACE ENGR  
ATTN DAVID LEWIS  
CHARLOTTESVILLE, VA 22090

VIRGINIA POLYTECHNIC INSTITUTE  
OF STATE UNIV  
MECHANICAL ENGINEERING DEPARTMENT  
ATTN PROF. H. MOSES  
BLACKSBURG, VA 24061

WASHINGTON UNIVERSITY  
SCHOOL OF ENGINEERING  
PO BOX 1185  
ATTN W. M. SWANSON  
ST LOUIS, MO 63130

WEST VIRGINIA UNIVERSITY  
MECHANICAL ENGINEERING DEPARTMENT  
ATTN RICHARD A. BAJURA  
MORGANTOWN, WV 26505

WICHITA STATE UNIVERSITY  
ATTN DEPT AERO ENGR, E. J. RODGERS  
WICHITA, KS 67208

UNIVERSITY OF WISCONSIN  
MECHANICAL ENGINEERING DEPARTMENT  
ATTN FEDERAL REPORTS CENTER  
ATTN NORMAN H. BEACHLEY, DIR  
DESIGN ENGINEERING LABORATORIES  
1513 UNIVERSITY AVENUE  
MADISON, WI 53706

WORCESTER POLYTECHNIC INSTITUTE  
ATTN GEORGE C. GORDON LIBRARY (TR)  
ATTN TECHNICAL REPORTS  
WORCESTER, MA 01609

ACCUMETRIX CORP  
ATTN R. M. PHILLIPPI (2 COPIES)  
1500 WILSON BLVD  
ARLINGTON, VA 22209

AVCO SYSTEMS DIVISION  
ATTN W. K. CLARK  
201 LOWELL STREET  
WILMINGTON, MA 01887

BARDER-COLMAN CO  
AIRCRAFT PRODUCTS DIVISION  
ATTN GARY FREDERICK  
1354 CLIFFORD AVENUE  
PO BOX 2940  
LOVES PARK, IL 61132-2960

BARNES ENGINEERING CO  
ATTN FRED SWEIHAUM  
30 COMMERCE ROAD  
STAMFORD, CT 06904

BELL HELICOPTER COMPANY  
PO BOX 482  
ATTN R. D. YEARY  
FT WORTH, TX 76101

BENDIX CORPORATION  
ELECTRODYNAMICS DIVISION  
ATTN D. COOPER  
11600 SHERMAN WAY  
N. HOLLYWOOD, CA 90605

BOEING COMPANY, THE  
PO BOX 3707  
ATTN HENRIK STRAUB  
SEATTLE, WA 98124

BOWLES FLUIDICS CORPORATION  
ATTN VICE PRES/ENGR  
6625 DOBBINS RD  
COLUMBIA, MD 21000

R. E. BOWLES  
2105 SONDRRA COURT  
SILVER SPRING, MD 20904

CHAMBERLAIN MANUFACTURING CORP  
EAST 4TH & ESTHER STS  
PO BOX 2545  
WATERLOO, IA 50705

CONTROL SYSTEMS INNOVATION  
ATTN N. F. MACIA  
517 EAST ORION STREET  
TEMPE, AZ 85283

CORDIS CORPORATION  
PO BOX 428  
ATTN STEPHEN F. VADAS, K-2  
MIAMI, FL 33137

CORNING GLASS WORKS  
ELECTRONIC MATERIALS PLANT  
ATTN SAM KASZCZYNEC  
PAINTED POST, NY 14870

CORNING GLASS WORKS  
FLUIDIC PRODUCTS  
ATTN R. H. BELLMAN  
HOUGHTON PARK, B-2  
CORNING, NY 14830

CHRYSLER CORPORATION  
PO BOX 118  
CIMS-418-33-22  
ATTN L. GAU  
DETROIT, MI 48231

JOHN DEERE PRODUCT ENGINEERING CENTER  
ATTN V. S. KUMAR  
WATERLOO, IA 50704

ELECTRIC POWER RESEARCH INSTITUTE  
PO BOX 10412  
ATTN MS. M. ANGIN,  
P. M. GEOTHERMAL ENERGY  
3412 HILLVIEW AVE  
PALO ALTO, CA 94303

ENGINEERING SOCIETIES LIBRARY  
ATTN ACQUISITIONS DEPARTMENT  
ATTN HOWARD GORDON  
345 EAST 47TH STREET  
NEW YORK, NY 10017

FLUIDICS QUARTERLY  
PO BOX 2989  
ATTN D. H. TARUMOTO  
STANFORD, CA 94305

FORD AEROSPACE & COMMUNICATIONS CORP  
ATTN DR. JOSEPH M. ISEMAN  
7235 STANDARD DRIVE  
HANOVER, MD 21076

FOXBORO COMPANY  
CORPORATE  
RESEARCH DIV  
ATTN JAMES VIGNOS  
ATTN J. DECARLO  
ATTN JOHN CHANG  
ATTN TOM KEGEL  
38 NEPONSET AVE  
FOXBORO, MA 02035

GARRETT PNEUMATIC SYSTEMS DIVISION  
PO BOX 5217  
ATTN TREVOR SUTTON  
ATTN TOM TIPPETTS  
ATTN C. ABBOTT  
111 SOUTH 34TH STREET  
PHOENIX, AZ 85010

GENERAL ELECTRIC COMPANY  
SACE/RES DIVISION  
PO BOX 8555  
ATTN MGR LIBRARIES, LARRY CHASEN  
PHILADELPHIA, PA 19101

GENERAL ELECTRIC COMPANY  
KNOLLS ATOMIC POWER LABORATORY  
ATTN D. KROMMENHOEK  
SCHENECTADY, NY 12301

GENERAL MOTORS CORPORATION  
DELCO ELECTRONICS DIV  
MANFRED G. WRIGHT  
NEW COMMERCIAL PRODUCTS  
PO BOX 1104  
ATTN R. E. SPARKS  
KOKOMO, IN 46901

GRUMMAN AEROSPACE CORPORATION  
TECHNICAL INFORMATION CENTER  
ATTN C. W. TURNER, DOCUMENTS  
LIBRARIAN  
ATTN TED SORENSEN, MS B1535

GRUMMAN AEROSPACE CORPORATION (cont'd)  
ATTN KEN HAIR, MS B1535  
SOUTH OYSTER BAY ROAD  
BETHPAGE, L. I., NY 11714

HAMILTON STANDARD  
DIVISION OF UNITED AIRCRAFT CORPORATION  
ATTN PHILIP BARNES  
WINDSOR LOCKS, CT 06096

HONEYWELL, INC  
ATTN J. HEDEEN  
ATTN W. POSINGIES  
1625 ZARTHAN AVE  
MINNEAPOLIS, MN 55413

HONEYWELL, INC  
ATTN RICHARD STEWART, MS 200  
1100 VIRGINIA DRIVE  
FT WASHINGTON, PA 19034

HUGHES HELICOPTERS  
DIVISION OF SUMMA CORPORATION  
CENTINELA & TEALE STREETS  
ATTN LIBRARY 2/T2124  
CULVER CITY, CA 90230

JOHNSON CONTROLS, INC  
ATTN WARREN A. LEDERMAN  
ATTN GEORGE JANU  
507 E. MICHIGAN  
MILWAUKEE, WI 53201

LEEDS & NORTHRUP CO  
ATTN ERNEST VAN VALKENBURGH  
DICKERSON ROAD  
NORTH WALES, PA 19454

MOORE PRODUCTS COMPANY  
ATTN R. ADAMS  
SPRING HOUSE, PA 19477

MARTIN MARIETTA CORPORATION  
AEROSPACE DIVISION  
ATTN R. K. BRODERSON, MP 326  
PO BOX 5837  
ORLANDO, FL 32805

MCDONNELL AIRCRAFT COMPANY  
GUIDANCE & CONTROL MECHANICS DIVISION  
ATTN ROYAL GUENTHER  
ST LOUIS, MO 63166

MCDONNELL DOUGLAS ASTRONAUTICS CO  
PROPULSION DEPARTMENT  
ATTN V. E. HALOULAKOS (A3-226)  
ATTN J. D. SCHWEIKLE (A3-226)  
5301 BOLSA AVENUE  
'UNTINGTON BEACH, CA 92647

NATIONAL FLUID POWER ASSOC.  
ATTN JOHN R. LUEKE  
DIR OF TECH SERVICES  
3333 NORTH MAYFAIR ROAD  
MILWAUKEE, WI 53222

NORTHROP CORP, ELECTRONICS DIV  
ATTN DESMOND NELSON  
SENIOR ENGINEER  
ORGN C3133, W/C  
2301 W. 120TH ST  
HAWTHORNE, CA 90250

PATSCENTER INTERNATIONAL  
ATTN MR. JOHN CLINE  
707 ALEXANDER ROAD  
PRINCETON, NJ 08540

PLESSEY AEROSPACE LTD  
ATTN A. ROSENBERG  
1700 OLD MEADOW ROAD  
MCLEAN, VA 22102

PROCON, INC.  
ATTN HERB MARCH  
OUP PLAZA  
DES PLAINES, IL 60016

PROPULSION DYNAMICS  
ATTN T. HOULIHAN  
2200 SOMERVILLE RD  
ANNAPOLIS, MD 21401

ROCKWELL INTERNATIONAL CORPORATION  
COLUMBUS AIRCRAFT DIVISION, PO BOX 1259  
ATTN MARVIN SCHWEIGER  
ATTN LOUIS BIAFORE  
4300 E. 5TH AVENUE  
COLUMBUS, OH 43216

SANDIA LABORATORIES  
ATTN WILLIAM R. LEUENBERGER, DIV 2323  
ATTN JERRY HOOD  
ATTN NED KELTNER  
ATTN ANTHONY VENERUSO, DIV 4742  
ALBUQUERQUE, NM 87185

DEFENSE RESEARCH TECHNOLOGIES, INC  
ATTN DR. T. DRZEWIECKI (2 COPIES)  
4608 NORBECK ROAD  
ROCKVILLE, MD 20853

SIKORSKY AIRCRAFT  
ATTN J. R. SOEHNLEIN  
NORTH MAIN STREET  
STRATFORD, CT 06602

STEIN ENGINEERING SERVICES, INC  
5602 E. MONTEROSA  
PHOENIX, AZ 85018

SYSCON CORP  
ATTN D. W. HOUCK  
1050 T. JEFFERSON ST, NW  
WASHINGTON, DC 20007

TRANS-TECH, INC  
ATTN L. DOMINGUES  
12 MEEM AVE  
GAITHERSBURG, MD 20760

TRITEC, INC  
ATTN L. SIERACKI (2 COPIES)  
PO BOX 56  
COLUMBIA, MD 21045

UNITED TECHNOLOGIES RESEARCH CENTER  
ATTN R. E. OLSON, MGR FLUID  
DYNAMICS LABORATORY  
400 MAIN STREET  
E. HARTFORD, CT 06108

VOUGHT CORP  
PO BOX 225907  
ATTN KELLEY FLING  
DALLAS, TX 75265

US ARMY LABORATORY COMMAND  
ATTN COMMANDER, AMSLC-CG  
ATTN TECHNICAL DIRECTOR, AMSLC-CT  
ATTN PUBLIC AFFAIRS OFFICE, AMSLC-PA

INSTALLATION SUPPORT ACTIVITY  
ATTN D  
ATTN RECORD COPY, SLCIS-IM-TS  
ATTN HDL LIBRARY, SLCIS-IM-TL (3 COPIES)  
ATTN HDL LIBRARY, SLCIS-IM-TL (WOODBIDGE)  
ATTN TECHNICAL REPORTS BRANCH, SLCIS-IM-TR  
ATTN LEGAL OFFICE, SLCIS-CC

HARRY DIAMOND LABORATORIES  
ATTN D/DIVISION DIRECTORS  
ATTN CORRIGAN, J., SLCHD-NW-P  
ATTN CHIEF, SLCHD-IT-R  
ATTN J. JOYCE, SLCHD-IT-R (20 COPIES)

**END**

**FILMED**

**2-86**

**DTIC**